

AD-A037 187

CALIFORNIA RESEARCH AND TECHNOLOGY INC WOODLAND HILLS

F/G 20/5

NUMERICAL INVESTIGATION OF WATER DROP EROSION MECHANISMS IN INF--ETC(U)

DEC 76 M ROSENBLATT, G E EGGUM, L A DEANGELO

F33615-75-C-5081

UNCLASSIFIED

CRT-2090-3

AFML-TR-76-193

NL

1 OF 1
AD
A037187



END

DATE

FILMED

4-77

AD A 037187

AFML-TR-76-193

✓

12

NUMERICAL INVESTIGATION OF WATER DROP EROSION MECHANISMS IN INFRARED-TRANSPARENT MATERIALS

CALIFORNIA RESEARCH AND TECHNOLOGY, INC.
6269 VARIEL AVENUE, SUITE 200
WOODLAND HILLS, CALIFORNIA 91367

DECEMBER 1976

TECHNICAL REPORT AFML-TR-76-193
FINAL REPORT FOR PERIOD 1 DECEMBER 1974 - 31 JULY 1976

BBB
MAR 22 1977
RECEIVED

Approved for public release; distribution unlimited

AIR FORCE MATERIALS LABORATORY
AIR FORCE WRIGHT AERONAUTICAL LABORATORIES
AIR FORCE SYSTEMS COMMAND
WRIGHT-PATTERSON AIR FORCE BASE, OHIO 45433



FOR THE DIRECTOR

AIR FORCE - 7 MARCH 77 - 300

RECEIVED
 DATE
 TIME
 BY
 U.S. DEPARTMENT OF JUSTICE
 DIVISION OF INVESTIGATION
 OFFICE OF THE ATTORNEY GENERAL
 U.S. DEPARTMENT OF JUSTICE
 DIVISION OF INVESTIGATION
 OFFICE OF THE ATTORNEY GENERAL

UNCLASSIFIED

SECURITY CLASSIFICATION OF THIS PAGE (When Data Entered)

19 REPORT DOCUMENTATION PAGE		READ INSTRUCTIONS BEFORE COMPLETING FORM
1. REPORT NUMBER AFML-TR-76-193	2. GOVT ACCESSION NO.	3. RECIPIENT'S CATALOG NUMBER
4. TITLE (and Subtitle) NUMERICAL INVESTIGATION OF WATER DROP EROSION MECHANISMS IN INFRARED-TRANSPARENT MATERIALS.		5. TYPE OF REPORT & PERIOD COVERED Final Report, 1 December 1974-31 July 1976
6. AUTHOR(s) M. Rosenblatt, L. A. DeAngelo G. E. Eggum, K. N. Kreyenhagen		7. PERFORMING ORG. REPORT NUMBER 4/CRT-2090-3
8. PERFORMING ORGANIZATION NAME AND ADDRESS California Research & Technology, Inc. 6269 Variel Avenue, Suite 200 Woodland Hills, CA 91367		9. CONTRACT OR GRANT NUMBER(s) F33615-75-C-5081
10. CONTROLLING OFFICE NAME AND ADDRESS Air Force Materials Laboratory Wright-Patterson AFB, Ohio 45433		11. PROGRAM ELEMENT, PROJECT, TASK AREA & WORK UNIT NUMBERS 6.1102F, Proj 2422, Task 242201, WU No. 73420213
12. MONITORING AGENCY NAME & ADDRESS (if different from Controlling Office)		13. REPORT DATE December 1976
14. DISTRIBUTION STATEMENT (of this Report) Approved for public release; distribution unlimited.		15. SECURITY CLASS. (of this report) UNCLASSIFIED
16. DISTRIBUTION STATEMENT (of the abstract entered in Block 20, if different from Report)		15a. DECLASSIFICATION/DOWNGRADING SCHEDULE
17. SUPPLEMENTARY NOTES		
18. KEY WORDS (Continue on reverse side if necessary and identify by block number) infrared windows numerical codes rain impact dynamic stresses erosion transmission loss crack initiation crack propagation		
19. ABSTRACT (Continue on reverse side if necessary and identify by block number) Numerical techniques were used to investigate the response of IR window materials to subsonic impacts (675 and 1100 fps) of water drops. Tensile crack initiation and propagation were treated, and the final predicted crack patterns were used to measure damage. Target damage sensitivity to elastic and tensile failure properties, impact velocity, density, and variations in numerical cell size were studied for 21 cases. The concept of using a rigid surface as an intermediary between water drop impact and window response was validated.		

DD FORM 1473

EDITION OF 1 NOV 65 IS OBSOLETE

UNCLASSIFIED

SECURITY CLASSIFICATION OF THIS PAGE (When Data Entered)

391223

AB

UNCLASSIFIED

SECURITY CLASSIFICATION OF THIS PAGE(When Data Entered)

An increase in the critical failure tensile stress, σ_c , to 8000 psi from the nominal 6500 psi causes a 60% reduction in target damage, while a decrease to 5000 psi increases target damage by over 100%. The tensile strength of the target is the most sensitive macromechanical physical characteristic in determining target damage.

Target damage decreases with an increase in Young's Modulus (E) or Poisson's Ratio (ν) and with a decrease in density (ρ_0).

The approximate relationship of the macromechanical property (σ_c) to a fundamental micromechanical property (the stress intensity factor (K_I)) in terms of the numerical calculation cell size (Δx) is as follows:

$$K_I = (\pi \Delta x)^{1/2} \sigma_c$$

The following damage mechanisms have been identified:

- o Tensile failure occurs behind the shear and Rayleigh waves, and cracks propagate until the shear wave has travelled about 1 droplet diameter in the 1100 fps impact case. (~ .5 μ sec for a 1 mm drop).
- o The water drop has time to interact with the surface cracks it generates during early stages of impact.
- o The presence of cracks significantly alters the stress fields near the developing cracks, thereby rendering elastic stress field predictions invalid once crack propagation begins.
- o Crack initiation and propagation may be enhanced by the high velocity water jets which are generated and which interact with surface roughness and flow into surface cracks and flaws.
- o The geometry of the drop is responsible for a pressure spike early in the impact which can actuate cracks by forcing water into surface openings.

$$* K_{sub I} = \text{sg. root of } (\pi(\Delta x)) \text{ sigma sub tau}$$

UNCLASSIFIED

SECURITY CLASSIFICATION OF THIS PAGE(When Data Entered)

PREFACE

When an IR window is exposed to impacts of rain droplets or ice particles at subsonic velocities (500-1100 fps), a loss in optical transmission frequently results which precedes any mass loss from the exposed surface. This phenomenology is not well understood, and is the subject of this report. The authors have used numerical methods to examine the dynamic stresses in window materials, the development of internal cracks which may cause transmission loss, and the dependency of these processes on various basic parameters characterizing window materials.

The work was performed for the Air Force Materials Laboratory under contract number F33615-75-C-5081. The guidance and assistance of the AFML Project Engineer, T. L. Peterson, is gratefully acknowledged.

TABLE OF CONTENTS

SECTION	PAGE
I. INTRODUCTION AND SUMMARY	1
1.1 Background and Objectives.	1
1.2 Analytical Approach.	1
1.3 Summary of Results	2
1.3.1 Impact Loading on Rigid Surface.	2
1.3.2 Window Response and Sensitivity Study for Water Drop Impacts	5
1.3.3 Damage Mechanisms.	14
1.4 Recommendations.	17
II. IMPACT LOADING ON RIGID SURFACE.	19
2.1 General Procedure for Impact Analysis.	19
2.2 675 fps Impact on Rigid Surface.	24
2.3 1100 fps Impact Solution	28
2.4 Independent Numerical Calculation.	34
2.5 Experimental Verification.	38
2.6 Details of the Pressure Peak at Very Early Times on the Outer Contact Radius Between the Spherical Water Drop and Rigid Surface	38
2.7 Comparison of Impact of a Water Drop on a Rigid Target and on a ZnSe Window.	42
III. MATERIAL PROPERTIES.	49
IV. PHENOMENOLOGY OF TARGET RESPONSE TO WATER DROP IMPACTS	52
V. SENSITIVITY STUDIES ON VARIOUS PARAMETERS INVOLVED IN WATER DROP IMPACTS ON WINDOWS.	61
5.1 Tensile Failure Criteria and Parameters.	61
5.2 Elastic Property Variations.	66

TABLE OF CONTENTS (CONT'D)

		PAGE
5.3	Target Density	68
5.4	Variation of Density and Young's Modulus	68
5.5	Impact Velocity Case and Repeated Impact on the Same Site	73
5.6	Target Thickness	75
5.7	Variations in Computational Zone Size and Effective Variation in Target Toughness.	78
	REFERENCE	84

LIST OF ILLUSTRATIONS

FIGURE		PAGE
1.	Steps Involved in Analytical Approach	3
2.	Velocity Field for 1100 fps Water Drop Impact on Rigid Surface at .47 and 1.16 μ sec	4
3.	Pressure-Time History at Impact Point for 1 mm Water Drop Impacting Rigid Surface at 1100 fps.	7
4.	Pressure-Radius Profiles on Rigid Surface for 1100 fps Water Drop Impact.	8
5.	Approximate Crack Length vs Time for 1100 fps Water Drop Impact on ZnSe Window (Case 1)	10
6A.	Target Damage as a Function of Stress Integral Parameter (κ_T).	11
6B.	Target Damage as a Function of Tensile Strength (σ_T).	11
6C.	Target Damage as a Function of Young's Modulus (E).	13
6D.	Target Damage as a Function of Poisson's Ratio (ν).	13
6E.	Target Damage as a Function of Material Density (ρ_0).	13

LIST OF ILLUSTRATIONS (CONT'D)

FIGURE		PAGE
7.	Crack Patterns and Predicted Target Damage in Cases 15 and 16.	15
8.	Initial Computational Grids for Water Drop Impact Problems, Early and Late Time Solution	23
9.	Velocity Field for 675 fps Water Drop Impact on Rigid Surface at .13 μ sec.	25
10.	Pressure-Radius Profiles on Rigid Surface for 675 fps Water Drop Impact	26
11.	Velocity and Pressure Fields for 675 fps Water Drop Impact on Rigid Surface at .26 μ sec.	27
12.	Velocity and Pressure Fields for 675 fps Water Drop Impact on Rigid Surface at .76 μ sec.	29
13.	Velocity and Pressure Fields for 675 fps Water Drop Impact on Rigid Surface at 1.31 μ sec	30
14.	Velocity and Pressure Fields for 675 fps Water Drop Impact on Rigid Surface at 1.87 μ sec	31
15.	Pressure-Radius Profiles on Rigid Surface at Transition between Early and Late Time Computational Grids	32
16.	Velocity and Pressure Fields for 1100 fps Water Drop Impact on Rigid Surface at .12 μ sec.	33
17.	Velocity and Pressure Fields for 1100 fps Water Drop Impact on Rigid Surface at .24 μ sec.	35
18.	Velocity and Pressure Fields for 1100 fps Water Drop Impact on Rigid Surface at .47 μ sec.	36
19.	Velocity and Pressure Fields for 1100 fps Water Drop Impact on Rigid Surface at 1.16 μ sec	37
20.	Pressure-Radius Profiles on Rigid Surface for Water Drop Impact	39
21.	Pressure Peak Characteristics for 675 and 1100 fps Impact Cases at Very Early Times.	41
22.	Relationship between Non-Dimensional Contact Radius, (r/R) , Time, $(\frac{Vt}{R})$ and Velocity of Contact Radius $(\frac{\dot{r}}{\dot{V}})$	44

LIST OF ILLUSTRATIONS (CONT'D)

FIGURE	PAGE
23. Initial Grid Configuration for 1100 fps Impact of Water Drop.	46
24. Velocity Field Comparison at .26 μ sec for 1100 fps Water Drop Impact on ZnSe Window and on Rigid Surface.	47
25. Pressure-Radius Profiles on Impact Surface for 1100 fps Impact of Water Drop on Rigid Surface and on ZnSe Window.	48
26. Treatment of Tensile Cracks in WAVE-L Code.	53
27. Crack Configuration at Various Times from Numerical Solution of 1100 fps Water Drop Impact on ZnSe Window	55
28. Contours of Peak Tensile Principal Stress for 1100 fps Water Drop Impact on ZnSe Window at .20 and .30 μ sec	57
29. Contours of Peak Tensile Principal Stress for 1100 fps Water Drop Impact on ZnSe Window at .40 and .50 μ sec	58
30. Computational Grid and Peak Tensile Principal Stress Contours for 1100 fps Water Drop Impact on ZnSe Window at .2 μ sec	59
31. Cumulative Maximum Tensile Stress Contours for 1 mm Water Drop Impact on ZnSe Window at 1100 fps . .	60
32. Crack Patterns as a Function of Stress Integral Parameters for 1100 fps Impact of .1 cm Water Drop on ZnSe Window	63
33. Crack Patterns as a Function of Tensile Strength, σ_T , for 1100 fps Impact of .1 cm Water Drop on ZnSe Window	65
34. Peak Values of Tensile Stress and Stress Integral of Purely Elastic ZnSe during 1100 fps Impact of .1 cm Water Drop (Case 18).	67
35. Crack Patterns as a Function of Young's Modulus, E, for 1100 fps Impact of .1 cm Water Drop on ZnSe Window	69
36. Crack Patterns as a Function of Poisson's Ratio, ν , for 1100 fps Impact of .1 cm Water Drop on ZnSe Window	70

LIST OF ILLUSTRATIONS (CONT'D)

FIGURE		PAGE
37.	Crack Patterns as a Function of Nominal Density, ρ_0 , for 1100 fps Impact of .1 cm Water Drop on ZnSe Window.	71
38.	Crack Patterns as a Function of Young's Modulus and Density for 1100 fps Impact of .1 cm Water Drop on ZnSe Window	72
39.	Peak Tensile Stress as a Function of Radius for 675 fps Impact Case	74
40.	Crack Pattern after Impact of Three Water Drops at 675 fps on ZnSe.	76
41.	Crack Pattern for Thin Target (.1 cm) Impacted with Water Drop at 1100 fps	77
42.	Crack Pattern for 1100 fps Water Drop Impact on ZnSe Window, Zone Size = 10, 20, 40	79

LIST OF TABLES

TABLE		PAGE
1.	Target Response Cases for Water Drop Impacts (D = .1 cm)	6
2.	Walker-Sternberg Equation of State.	21
3.	Critical Water Drop Parameters When $\dot{r} = C = 5000$ fps for $V = 675$ and 1100 fps	42
4.	Properties of ZnSe and Calcium Alumino-Sicate Glass	50
5.	Effective Stress Intensity Factors According to Equation 7.	82
6.	Effective Stress Intensity Factors According to Equation 6.	82

SECTION I

INTRODUCTION AND SUMMARY

1.1 Background and Objectives

There is a need for substantially improving the resistance of IR windows to optical damage resulting from subsonic impacts of rain drops. Such damage is usually referred to as subsonic erosion, although it differs from more conventional erosion in that significant optical damage occurs before there is any mass loss from the surface. The apparent reason for the optical damage is internal cracking, which causes loss of transmittance as well as degradation of optical quality.

Erosive damage of optically transparent materials by water drop impacts has been experimentally studied (e.g., Reference 1), and data have been obtained regarding the optical transmission loss through specific materials subjected to specific erosive environments. However, it is difficult to generalize from these data because of the complex nature of the phenomena involved.

The present study makes use of an efficient *numerical* technique for investigating response of window materials to subsonic water drop impacts. Specific objectives of the program were: (1) to identify the mechanisms responsible for transmittance loss in IR windows subjected to subsonic rain erosion, and (2) to determine the sensitivity of these mechanisms to basic material parameters.

1.2 Analytical Approach

The approach taken for accomplishing these objectives is based on numerical code solutions using the WAVE-L code. (WAVE-L is a 2-D Lagrangian finite difference code based on the HEMP code, Reference 2.) The following steps are involved in the analyses:

1. Impact loading analyses are performed to determine the history of stresses applied to a window surface by water drop impacts. The loading stresses are stored as a function of position on the target surface and time.
2. The impact loading stresses are then applied as a surface boundary condition to investigate the dynamic stress and failure response of window materials to the impact loading.

The sequential relationship between these steps is shown in Figure 1.

1.3 Summary of Results

During the course of this program numerical solutions were obtained which predict the response of materials to water drop impacts at 675 and 1100 fps. Detailed analyses of target damage sensitivity to elastic and tensile properties, material density, impact velocity and numerical cell size were performed for 21 cases.

1.3.1 Impact Loading on Rigid Surface

The impact dynamics and surface pressure loadings from a 1 mm water drop impacting a *rigid* surface at 675 fps and at 1100 fps were calculated using the WAVE-L code. Figure 2 shows two representative velocity field plots from the 1100 fps impact solution, and illustrates the nature of the impact process. Jetting, the development of radial velocities greater than the impact velocity, is prominent in the figure. The peak ratio of jetting velocity to impact velocity in the 1100 fps numerical solution was 3, which is consistent with observed values (Reference 3).

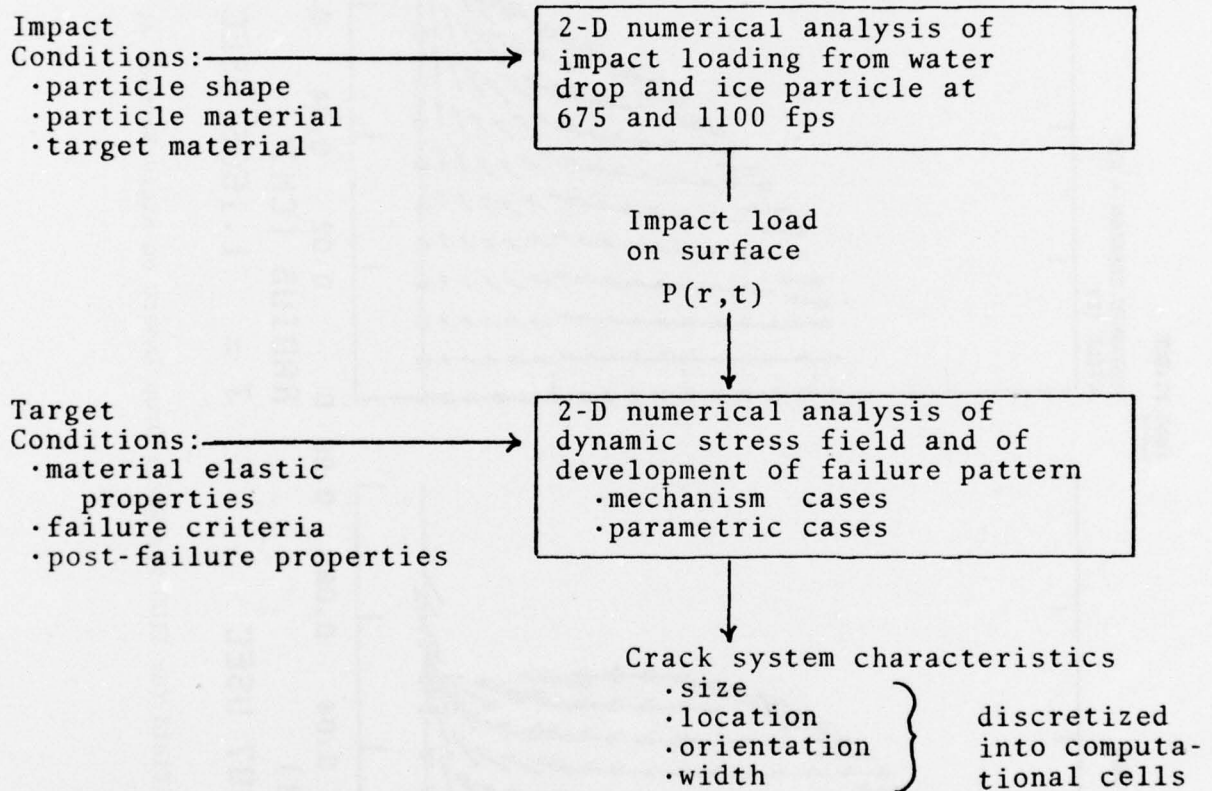


Figure 1. Steps Involved in Analytical Approach

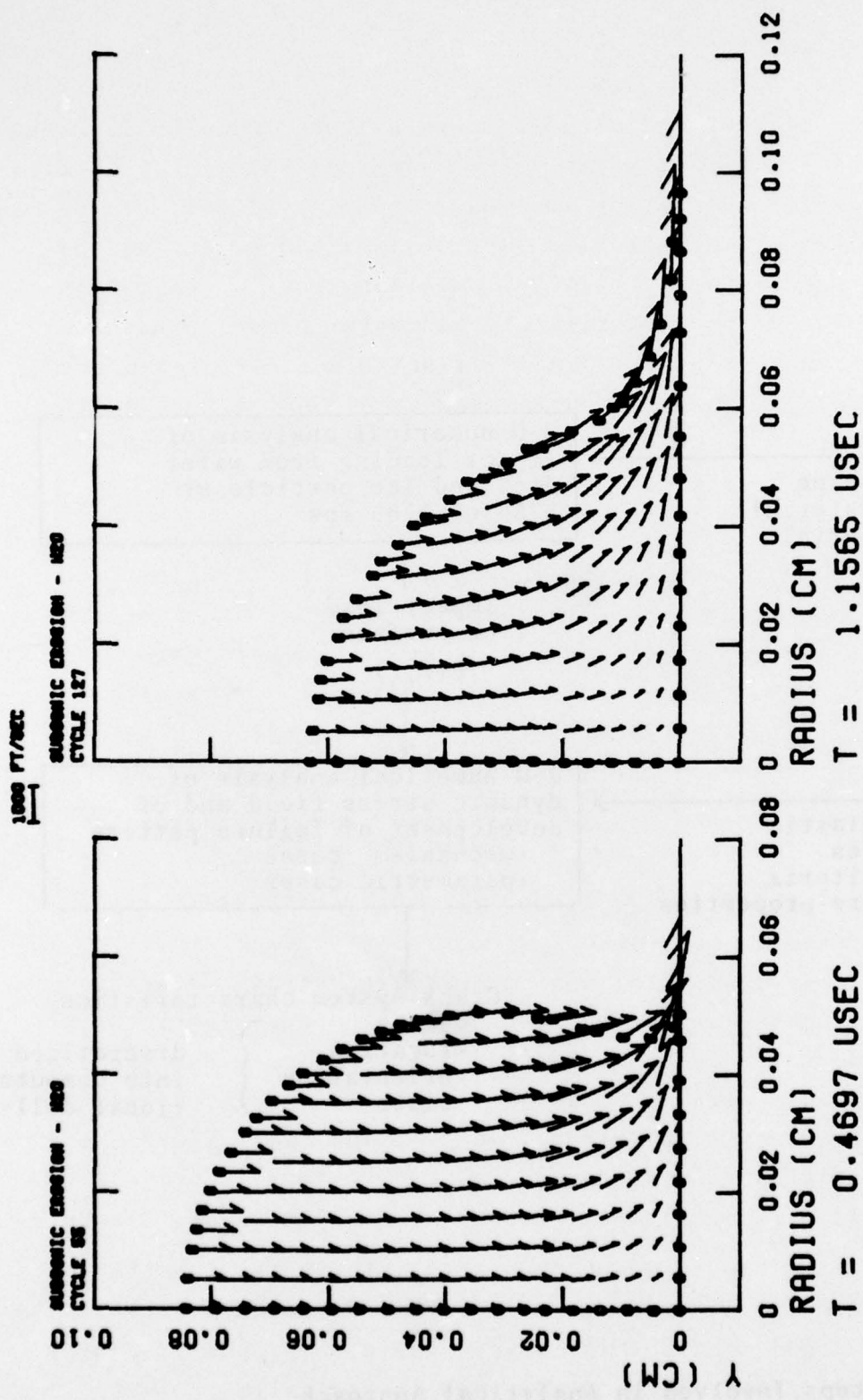


Figure 2. Velocity Field for 1100 fps Water Drop Impact on Rigid Surface at .47 and 1.16 μsec

Figure 3 shows the pressure-time history from the 1100 fps solution at the impact point. The numerical solution generated by Huang (Reference 4) for an impact velocity of 980 fps is also on this figure. The solutions are similar except during the first 0.1 μ sec, where the WAVE-L solution shows an almost instantaneous rise to approximately the water hammer pressure, in contrast with the more gradual rise to a lower pressure shown by Huang. However, particular efforts were made in the WAVE-L solution to resolve transitory phenomena; thus we believe the behavior of the WAVE-L solution is more accurate during the first 0.1 μ sec.

Figure 4 presents several pressure-radius profiles from the 1100 fps impact case. These profiles show, at several times, the spatial variations in pressure which load the surface of a window from a single drop. Note in the profiles at $t = .12, .24, \text{ and } .48 \mu\text{sec}$ that pressures are greatest near the periphery of the expanding contact surface.

1.3.2 Window Response and Sensitivity Study for Water Drop Impacts

Table 1 lists the 21 window response and sensitivity cases analyzed in this study. ZnSe ($\rho_0 = 5.27 \text{ gm/cm}^3$, $E = 10 \times 10^6 \text{ psi}$, $\nu = .3$) was the baseline window material treated. Impacts were simulated both on purely elastic ZnSe and on ZnSe which is allowed to fail in tension. Two types of tensile failure were modeled: (1) failure whenever a critical tensile stress (σ_T) is exceeded ($\sigma > \sigma_T$), and (2) failure whenever a specified time integral, κ_T , of the tensile over-stress is exceeded ($\int_0^t (\sigma - \sigma_T) dt > \kappa_T$, for $\sigma > \sigma_T$). In both cases, discrete tensile cracks can form and propagate through the computational grid. (When a cell cracks, the WAVE-L code calculates the orientation and width of the crack, and also properly adjusts the residual properties and stresses in the cell.

TABLE 1

TARGET RESPONSE CASES FOR WATER DROP IMPACTS (D = .1 cm)

Case	Impact Velocity V (fps)	Tensile Stress Integral Parameters κ_T (10^{-7} Mbar- μ sec)	σ_T (psi)	Young's Modulus E (10^6 psi)	Poisson's Ratio ν	Density ρ_0 (gm/cm ³)	Cell Size Δx (10^{-4} cm)	Relative Target Damage A/A _n	Comments
1	1100	0	6500	10	.3	5.27	50	1.59	Vary κ_T (baseline case)
2		5						1.0	
3		20						0.53	Vary κ_T
4		50						0.30	Vary κ_T
5		5	5000					2.26	Vary σ_T
6			8000					0.40	Vary σ_T
7			6500	6				1.27	Vary E
8				14				0.64	Vary E
9				10	.2			1.01	Vary ν
10					.4			0.81	Vary ν
11					.3	4.0		0.77	Vary ρ_0
12						6.5		1.04	Vary ρ_0
13				14		4.0		0.33	Vary E and ρ_0
14		0		10		5.27	100	0.61	Vary Δx , $\kappa_T=0$
15		0					25	3.57	Vary Δx , $\kappa_T=0$
16		0	3000				100	3.36	Vary σ_T and Δx , $\kappa_T=0$
17			Elastic target				50		Elastic Solution
18			Elastic target				25		Elastic Solution
19	675	5	6500				50		(No cracks developed)
20		0					↓		Multiple Impacts
21	1100	5	6500	10	.3	5.27	50		Thin Target Case

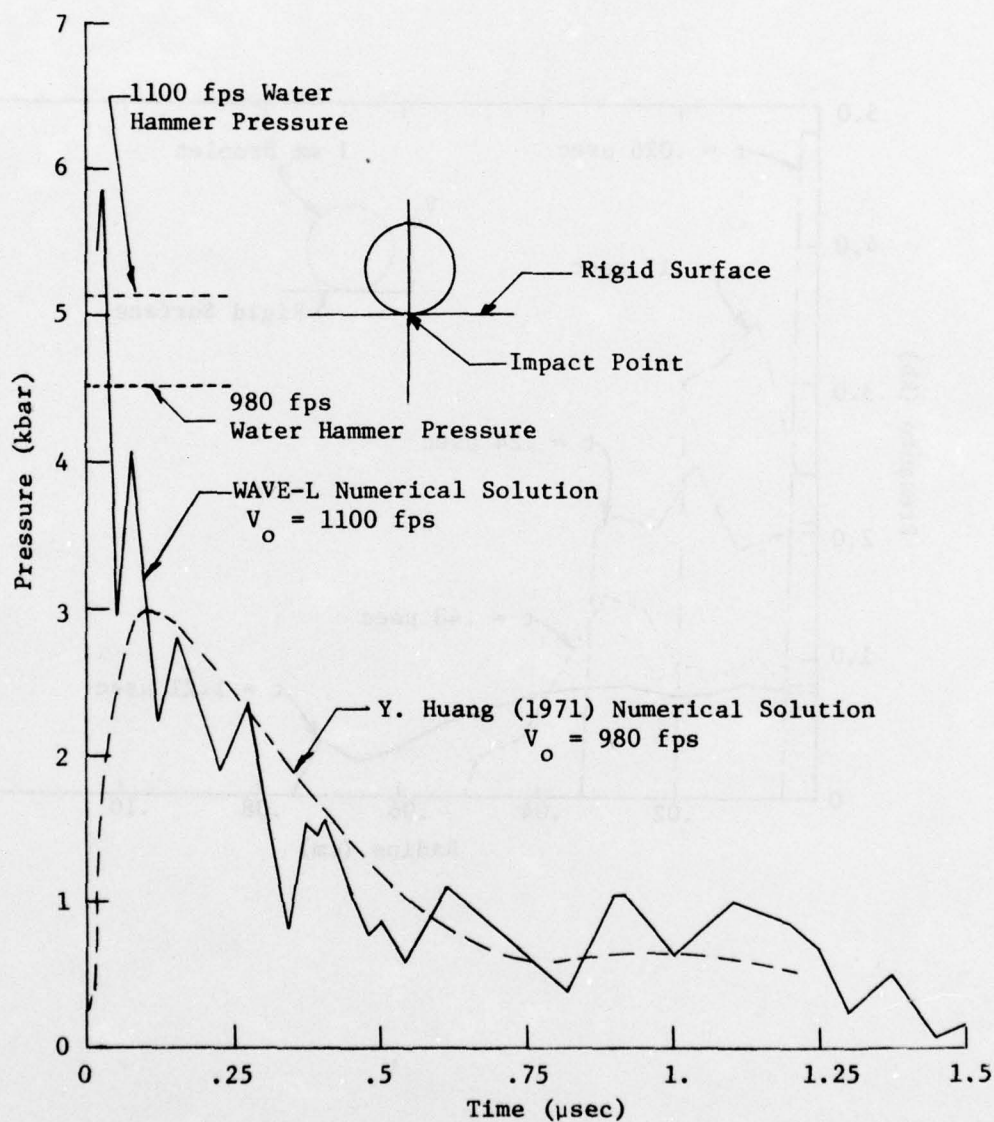


Figure 3. Pressure-Time History at Impact Point for 1 mm Water Drop Impacting Rigid Surface at 1100 fps

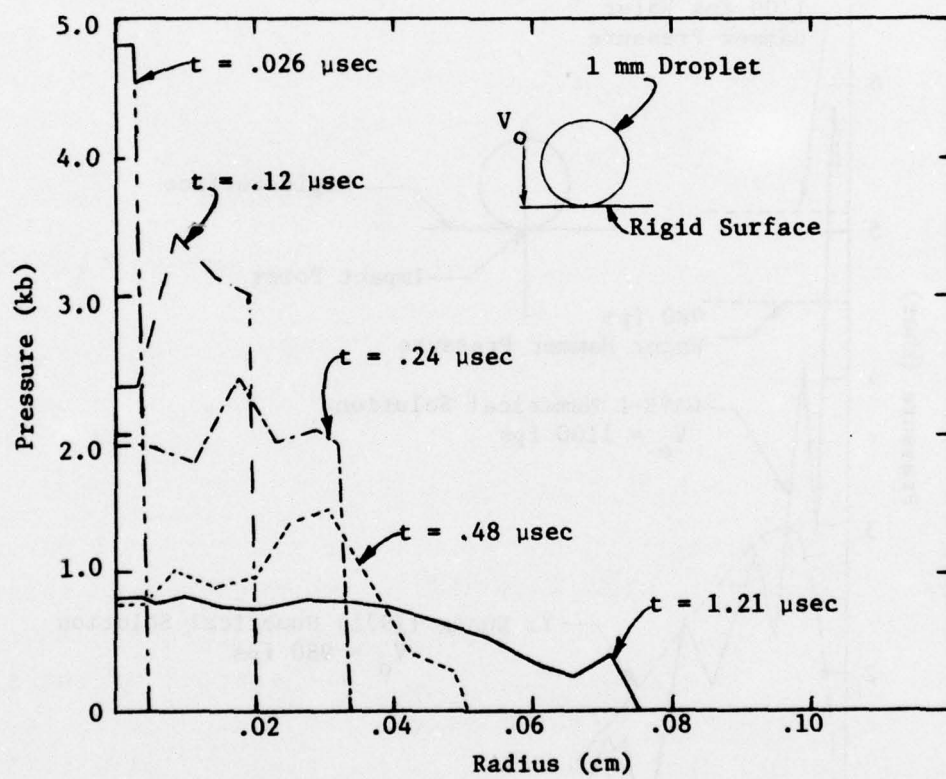


Figure 4. Pressure-Radius Profiles on Impact Surface for 1100 fps Impact of a Water Drop on a Rigid Surface

The propagation of tensile cracks from a 1100 fps water drop impact is illustrated in Figure 5. This figure shows the final crack pattern from the Case 1 solution, which used the critical tensile stress criteria ($\kappa_T = 0$) with $\sigma_T = 6500$ psi. The tensile cracks propagate at velocities on the order of the material shear ($C_s = .22$ cm/ μ sec) and Rayleigh wave speeds. In fact, the cracks form and propagate behind the shear wave front which develops during the water drop impacts. *By .5 μ sec, the tensile cracks are completely formed in this impact.*

The sensitivity study involved the variation of material parameters (κ_T , σ_T , E , ν , ρ_0), impact velocity (V), and computational zone size (Δx). The crack surface area (A), as computed by the numerical solutions, was used as a measure of the target damage. Table 1 lists the target damage in non-dimensional form, A/A_n , where $A_n = 8 \times 10^{-3}$ cm² is the cracked surface area for the base case (Case 2).

Figure 6 summarizes the results of the material parameter sensitivity study. Figure 6A shows target damage dependence on the stress integral parameter (κ_T). The target damage is a relatively strong function of κ_T and therefore of the strain rate characteristics of the target. An increase of κ_T from zero to 5×10^{-7} Mbar- μ sec reduces the target damage by 37%. (The $\kappa_T = 5 \times 10^{-7}$ results are used as the baseline target damage case in this study.)

Figure 6B shows target damage when critical tensile strength, σ_T , is varied and $\kappa_T = 5 \times 10^{-7}$ Mbar- μ sec is held constant. An increase in σ_T to 8000 psi from the nominal $\sigma_T = 6500$ psi causes a 60% reduction in target damage. A decrease to 5000 psi causes the target damage to increase by over 100%.

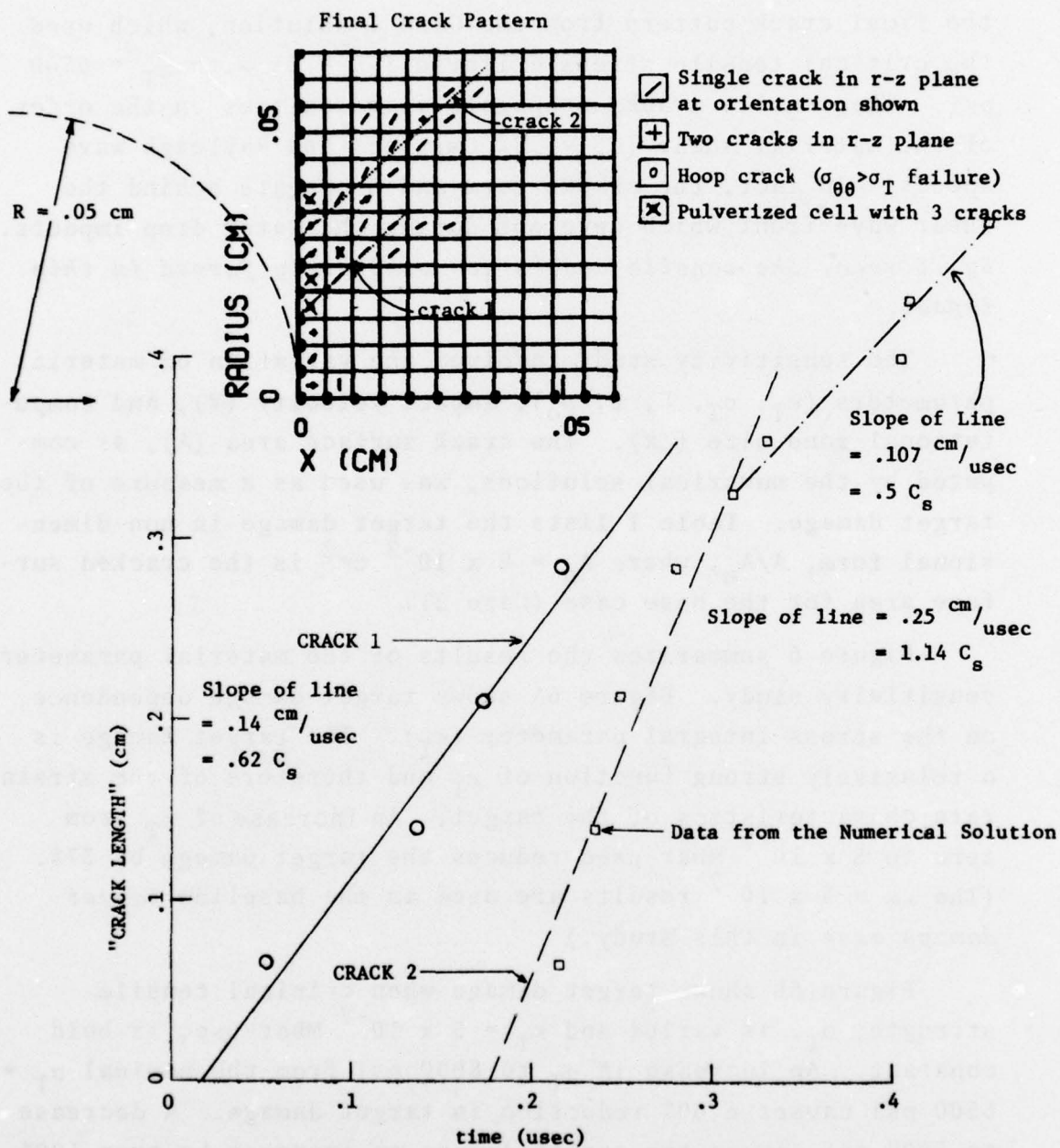


Figure 5. Approximate Crack Length versus Time for 1100 fps Water Drop Impact on ZnSe Window (Case 1)

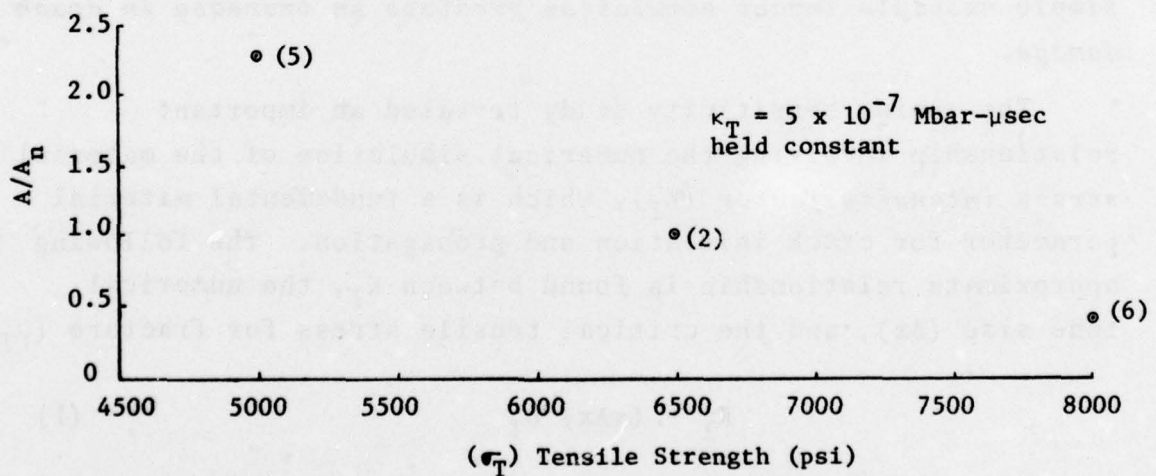
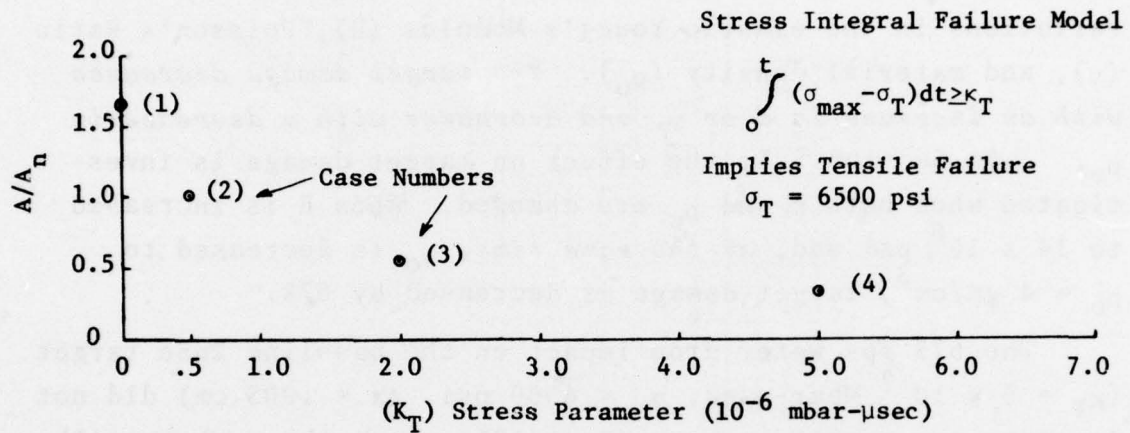


Figure 6A,B. Target Damage as a Function of Stress Integral Parameter (κ_T) and Tensile Strength (σ_T)

The tensile strength of the target is the most sensitive physical material characteristic in determining target damage.

Figures 6C, 6D, and 6E show target damage caused by variations in the elastic Young's Modulus (E), Poisson's Ratio (ν), and material density (ρ_0). *The target damage decreases with an increase in E or ν , and decreases with a decrease in ρ_0 .* In Section 5.3, the effect on target damage is investigated when both E and ρ_0 are changed. When E is increased to 14×10^6 psi and, at the same time, ρ_0 is decreased to $\rho_0 = 4 \text{ gm/cm}^3$, target damage is decreased by 67%.

The 675 fps water drop impact on the baseline ZnSe target ($\kappa_T = 5 \times 10^{-7}$ Mbar- μsec , $\sigma_T = 6500$ psi, $\Delta x = .005$ cm) did not generate any tensile cracks (Case 19), since the peak tensile stress exceeded σ_T only for a very short time. The solution was repeated with $\kappa_T = 0$ (Case 20), and one tensile crack developed. The final target conditions were then used for a second and third water drop impact on the same site. This simple multiple impact simulation predicts an increase in crack damage.

The zoning sensitivity study revealed an important relationship involving the numerical simulation of the material stress intensity factor (K_I), which is a fundamental material parameter for crack initiation and propagation. The following approximate relationship is found between K_I , the numerical zone size (Δx), and the critical tensile stress for fracture (σ_T):

$$K_I = (\pi \Delta x)^{1/2} \sigma_T \quad (1)$$

This equation is important because K_I is a measurable physical material parameter which is more fundamental than σ_T

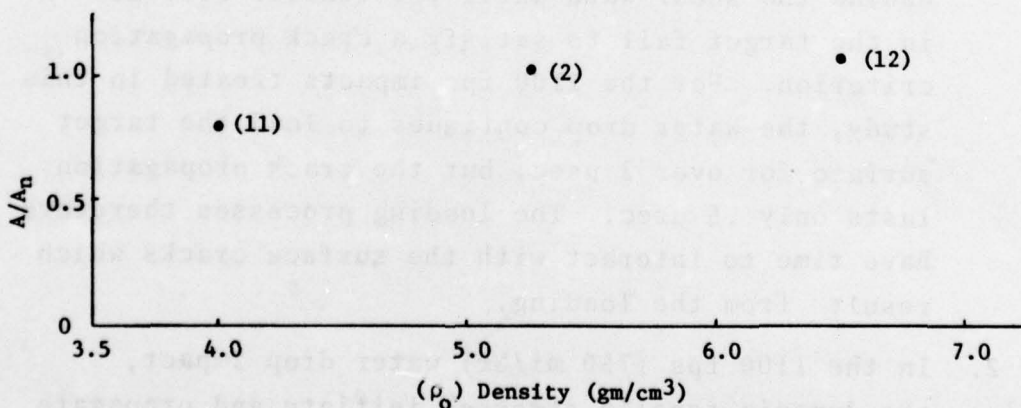
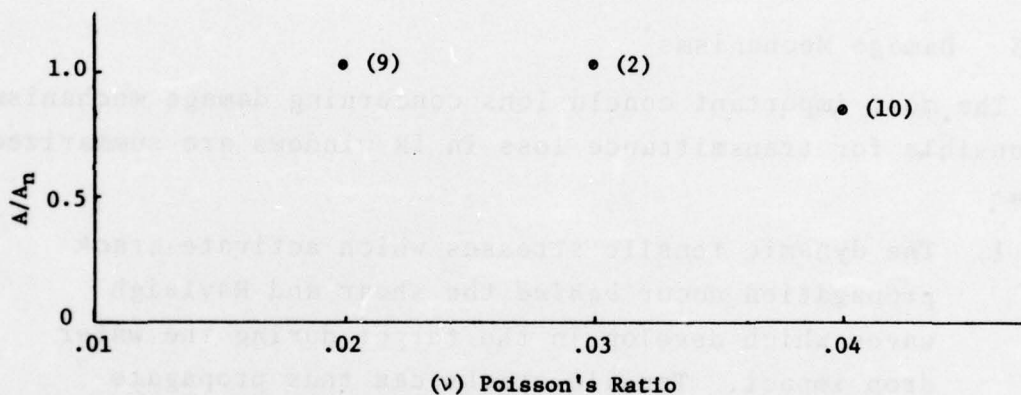
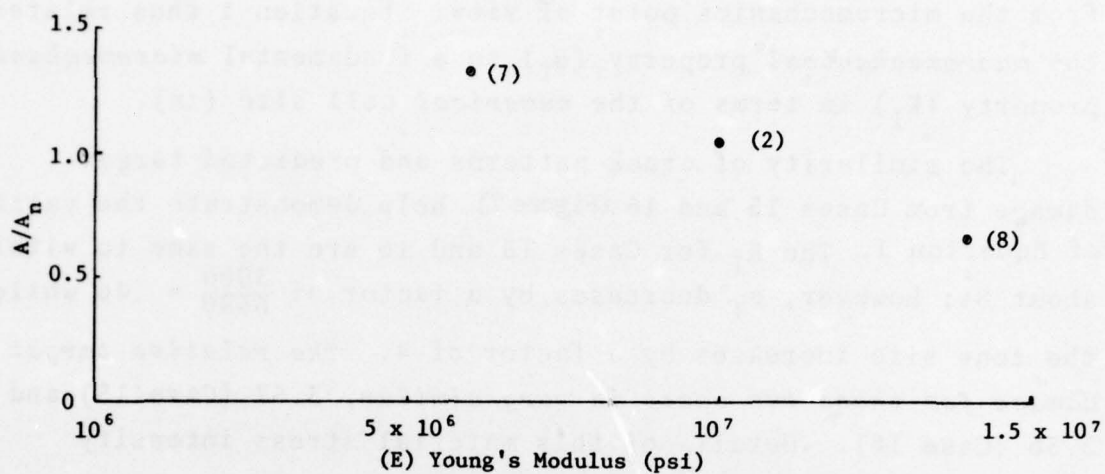


Figure 6C,D,E. Target Damage as a Function of Young's Modulus (E) , Poisson's Ratio (ν) , and Material Density (ρ_o)

from the micromechanics point of view. Equation 1 thus relates the *macromechanical* property (σ_T) to a fundamental *micromechanical* property (K_I) in terms of the *numerical* cell size (Δx).

The similarity of crack patterns and predicted target damage from Cases 15 and 16 (Figure 7) help demonstrate the validity of Equation 1. The K_I for Cases 15 and 16 are the same to within about 8%; however, σ_T decreases by a factor of $\frac{3000}{6500} = .46$ while the zone size increases by a factor of 4. *The relative target damage for these two cases is very similar, 3.57 (Case 15) and 3.36 (Case 16).* Details of this material stress intensity factor model are described in Section 5.7.

1.3.3 Damage Mechanisms

The most important conclusions concerning damage mechanisms responsible for transmittance loss in IR windows are summarized below:

1. The dynamic tensile stresses which activate crack propagation occur *behind* the shear and Rayleigh waves which develop in the target during the water drop impact. Tensile cracks can thus propagate behind the shear wave until the tensile stresses in the target fail to satisfy a crack propagation criterion. For the 1100 fps impacts treated in this study, the water drop continues to load the target surface for over 2 μ sec, but the crack propagation lasts only .5 μ sec. The loading processes therefore have time to interact with the surface cracks which result from the loading.
2. In the 1100 fps (750 mi/hr) water drop impact, the dynamic tensile stresses initiate and propagate cracks in the ZnSe targets. The presence of the

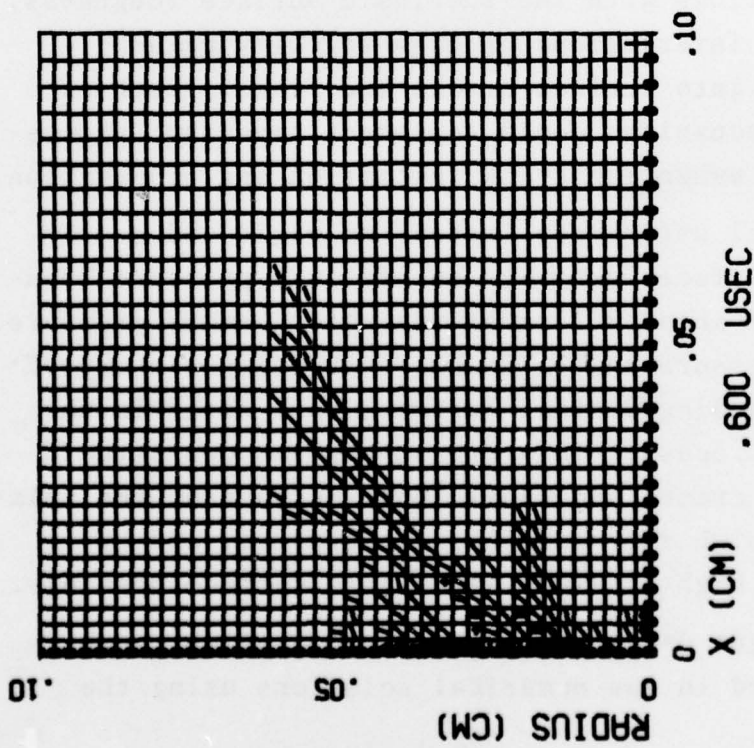
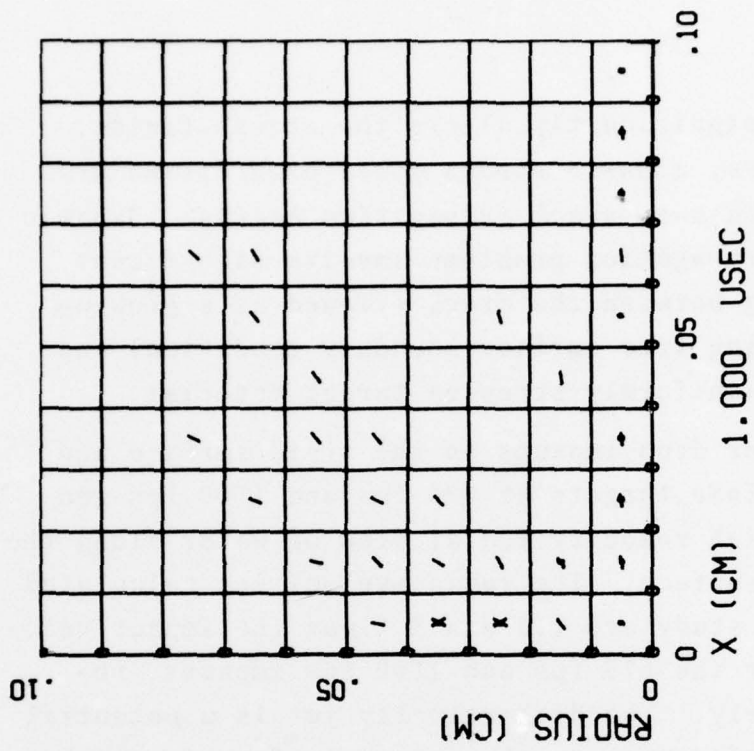


Figure 7. Crack Patterns and Predicted Target Damage in Cases 15 and 16.

cracks significantly alters the stress fields. *Therefore, elastic stress field predictions are not valid once crack propagation begins.* Dynamic crack propagation problems involve significant coupling between the crack (viewed as a growing and moving free surface boundary condition) and the non-uniformly stressed target material.

3. The water drop impacts on the rigid surface and on the ZnSe targets at 675 fps and 1100 fps generate high velocity radial flow of water along the target surface. The radial velocities calculated in this study are 2.5 and 3 times the impact velocity for the 675 fps and 1100 fps impacts, respectively. The high velocity jet is a potential source of damage to the target surface from (a) interactions with the intrinsic surface roughness, and (b) interactions of high velocity water flowing into surface cracks and flaws. Both of these mechanisms could represent important processes for enhancing crack initiation and propagation.
4. Spherical water drop impacts on rigid and nearly rigid surfaces generate an off-axis pressure transient of about 2.7 times the water hammer pressure. This pressure spike occurs near the periphery of the expanding contact surface, very early in the impact process. This pressure spike can actuate surface cracks and flaws, both because of the relatively high stresses which it induces, and by forcing high pressure water into surface openings.
5. The target damage from crack propagation can be simulated in the numerical solutions using the

fundamental material stress intensity factor (K_I) based on the following approximate relationship.

$$K_I = (\pi \Delta x)^{\frac{1}{2}} \sigma_T$$

1.4 Recommendations

The results of this study demonstrate that an efficient numerical technique for investigating the response of window materials to subsonic water drop impacts has been developed. Also, the unique capability of numerical solutions to predict the response of hypothetical materials of possible interest was successfully applied in the form of a detailed target damage sensitivity study involving elastic properties, density, tensile failure properties, impact velocity, and numerical cell size.

The most important results of this study involve the predictions of specific crack patterns and damaged areas as a function of tensile failure criteria and parameters. Also, the predicted target damage results based on the material stress intensity factor (K_I) was significant. This aspect of the study should be continued and expanded to include more detailed examination of crack propagation theory and to develop a model which connects the microscopic details of crack propagation to the macroscopic description inherent in numerical codes.

The following actions are recommended in order to take advantage of the results of this study:

1. Examine and model the relationship between *microscopic* crack initiation and propagation theory and the *macroscopic* descriptions which can be provided by numerical codes.

2. Apply the numerical codes to other materials of interest.
3. Apply the numerical codes to potential multi-material window designs of interest.
4. Use the numerical codes in a plane strain mode to investigate multiple-impact phenomenology for impacts on separated sites.

SECTION II

IMPACT LOADING ON A RIGID SURFACE

The impact of a water drop on a surface produces very high transient pressures or stresses in both the drop and the target material near the contact surface. Shock or intense stress waves propagate from the immediate impact interface, both into the target material and into the still-advancing drop-let. Geometric divergence and pressure relief from free surfaces result in rapid reduction of the peak pressure/stress.

The wave propagating into the water drop produces deceleration as well as severe distortion as the high pressures interact with the walls of the drop. The drop flattens against the target surface, and the pressure falls off as the region of impact loading grows. Simultaneously, target material beneath the impact is compressed. In very high-velocity impacts, this localized compression is sufficient to produce significant axial and radial distortion in the target, resulting in penetration and/or cratering. In the relatively low-velocity water impacts which are of interest in this program, the target surface will respond with only small distortions. This reduces the complexity of the impact dynamics, since loading occurs on an essentially flat surface.

2.1 General Procedure for Impact Analysis

In order to provide a loading function, $P(r,t)$, for the analyses of dynamic response of IR window materials, two impact solutions were calculated for a 1 mm spherical water drop on a rigid plane surface. The WAVE-L code was used for these solutions.

The initial water drop velocities in the impact problems are 675 fps (460 mi/hr) and 1100 fps (750 mi/hr). The numerical fit of Walker and Sternberg (Ref. 5) to the equation of

state of water, as given in Table 2 was used in the calculations. Since the purpose of these calculations was to obtain the pressure on the plane interface as a function of time and position, and since the largest and potentially most important pressures and pressure gradients occur early in the impacts, the following procedure was adopted for each solution:

- (a) A relatively finely zoned grid (shown in Figure 8A) was used to determine the early-time loading. The vertical axis at $r = 0$ is the axis of symmetry. Since this grid was designed with computational accuracy in mind, the interface stress function obtained during the initial high stress phase of the solution is well resolved. Integration of this grid proceeded until $.34 \mu\text{sec}$ in the 675 fps solutions, and until $.26 \mu\text{sec}$ in the 1100 fps solution. The maximum pressures at these times were approximately 1.0 Kbar (from 3.1 Kbar water hammer pressure) and 2.6 Kbar (from 5.1 Kbar water hammer pressure), respectively.
- (b) A less finely zoned grid (shown in Figure 8B) was used to determine the pressure loading at later times (i.e., after $.34 \mu\text{sec}$ and $.26 \mu\text{sec}$ in the 675 and 1100 fps impacts, respectively.) Since this grid was chosen as a compromise between ease of rezoning and computational considerations, the integration was not exceptionally difficult, as it would have been using the grid shown in Figure 8A.

The physical phenomena taking place during the impact of a water drop have been examined both theoretically and experimentally by many workers (e.g., References 6-9). Generally,

TABLE 2. WALKER-STERNBERG EQUATION OF STATE

$$P(v, e) = \frac{f_1(e)}{v} + \frac{f_2(e)}{v^3} + \frac{f_3(e)}{v^5} + \frac{f_4(e)}{v^7}$$

where $v = \frac{1}{\rho}$, e is the specific internal energy, and

$$f_{1\alpha}(e_\alpha) = a_0 + a_1 e_\alpha + a_2 e_\alpha^2 + a_3 e_\alpha^3 + a_4 e_\alpha^4 + a_5 e_\alpha^5 \\ + a_6 e_\alpha^6 + a_7 e_\alpha^7$$

$$f_{2\beta}(e_\beta) = b_0 + b_1 e_\beta + b_2 e_\beta^2 + b_3 e_\beta^3 + b_4 e_\beta^4 + b_5 e_\beta^5 \\ + b_6 e_\beta^6 + b_7 e_\beta^7 + b_8 e_\beta^8$$

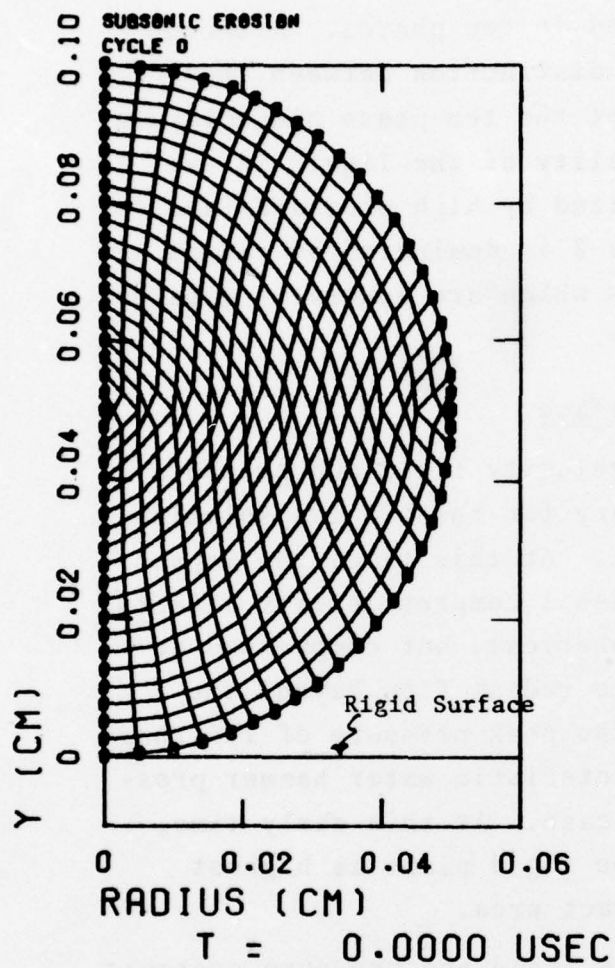
$$f_3(e) = c_0 + c_1 e$$

$$f_4(e) = d_0 + d_1 e$$

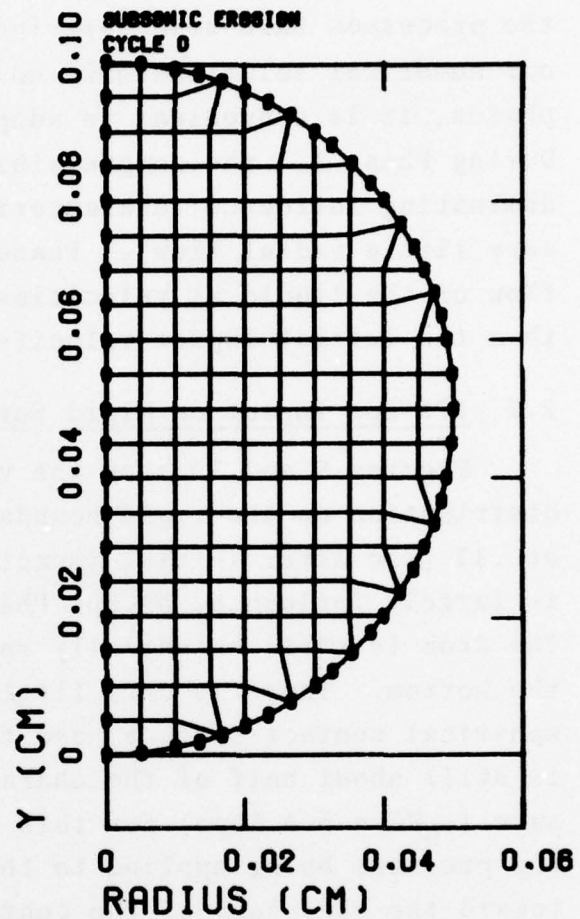
	Region α_1 $e_\alpha = e$ $0 \leq e \leq .006$	Region α_2 $e_\alpha = e - .006$ $.006 < e \leq .017$	Region α_3 $e_\alpha = e - .017$ $.017 < e$
a_0	.005722427	.001015091	.0005607572
a_1	- 1.240522	- .3270122	.11228400
a_2	50.42535	6.734616	5.275769
a_3	- 1.400579 $\times 10^3$	1.552785 $\times 10^4$	82.21745
a_4	4.13795 $\times 10^6$	- 2.92644 $\times 10^6$	-147.1514
a_5	- 2.726437 $\times 10^8$	2.139341 $\times 10^8$	- 4.044093
a_6	- 1.295684 $\times 10^{11}$	- 5.6153858 $\times 10^9$	- 3.130131 $\times 10^4$
a_7	- 1.4379880 $\times 10^{13}$	0.	0.

TABLE 2. WALKER-STERNBERG EQUATION OF STATE (Continued)

	Region β_1 $e_\beta = e$ $0 \leq e \leq .0032$	Region β_2 $e_\beta = e - .0032$ $.0032 < e \leq .0245$	Region β_3 $e_\beta = e - .0245$ $.0245 < e$
b_0	- .02748180	- .02215430	.002499950
b_1	1.691130	1.510990	.9374720
b_2	17.12981	-10.56299	- 4.624610
b_3	1.483364×10^4	$- 5.411856 \times 10^3$	- 44.52203
b_4	$- 1.549072 \times 10^7$	6.176871×10^5	375.1364
b_5	3.415591×10^9	$- 1.810118 \times 10^7$	0.
b_6	$- 2.357818 \times 10^{11}$	$- 6.2057 \times 10^8$	0.
b_7	0.	4.406075×10^{10}	0.
b_8	0.	$- 6.587460 \times 10^{11}$	0.
c_0	.0268	d_0 - .005	
c_1	- .4148	d_1 .0741	



(8A)



(8B)

Figure 8. Initial Computational Grids for Water Drop Impact Problems,
Early and Late Time Solution

the processes have been described in two phases. Although our numerical solutions make no distinction between these phases, it is convenient to adopt the two-phase nomenclature. During Phase 1, the compressibility of the liquid is the dominating influence (characterized by high pressures and very little radial flow). Phase 2 is dominated by radial flow of the liquid at velocities which are generally greater than the initial impact velocity.

2.2 675 fps Impact on Rigid Surface

Figures 9 and 10 show the velocity field and pressure distribution on the rigid boundary for the 675 fps solution at .13 μ sec after initial impact. At this time, the impact is largely influenced by the Phase 1 compressibility effects. The drop is still essentially spherical, but compressed at the bottom. There is very little radial flow beyond the spherical contact surface, and the peak pressure of 1.6 Kbar is still about half of the characteristic water hammer pressure ($\rho_0 VC = 3.1$ Kbar) for this case. At this early time, the pressure being applied to the rigid plane is highest toward the *periphery* of the contact area.

Figure 11 shows the velocity field and pressure contours in the drop at .26 μ sec. Here the velocity plot shows that radial flow is beginning, but has not yet caused large distortions. The pressure is still high, and the point of application of the greatest pressure on the rigid plane remains at the periphery of the contact area (see Figure 10). It is interesting to note in Figure 11 that the peak pressure region within the drop is not on the rigid target surface, but rather is slightly above that surface.

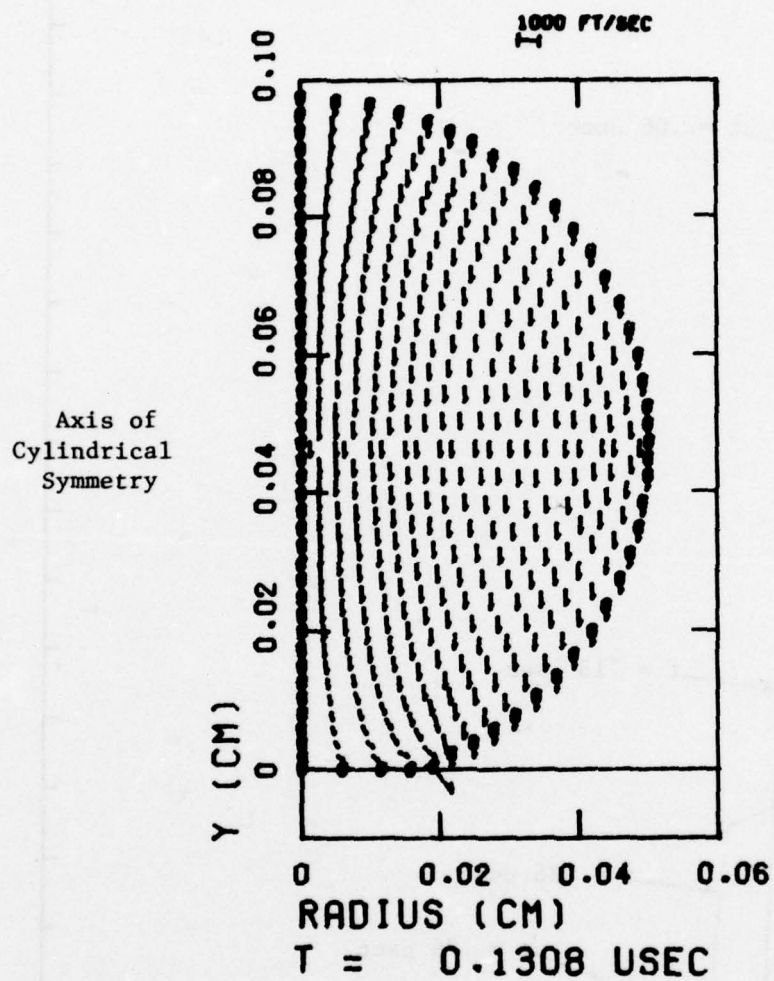


Figure 9. Velocity Field for 675 fps Impact of a Water Drop on a Rigid Surface at .13 μ sec

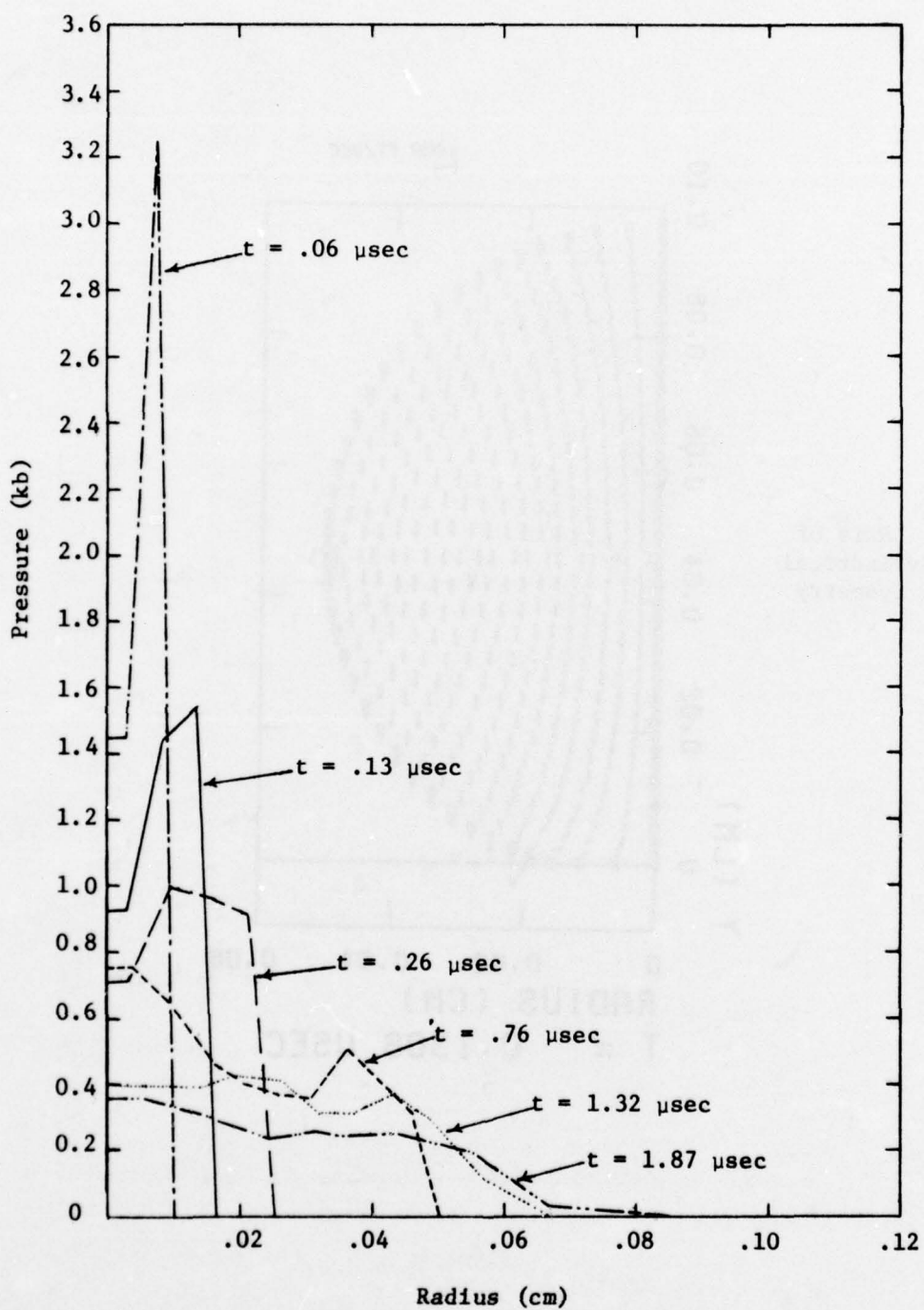


Figure 10. Radial Pressure Profiles on a Rigid Surface for 675 fps Water Drop Impact

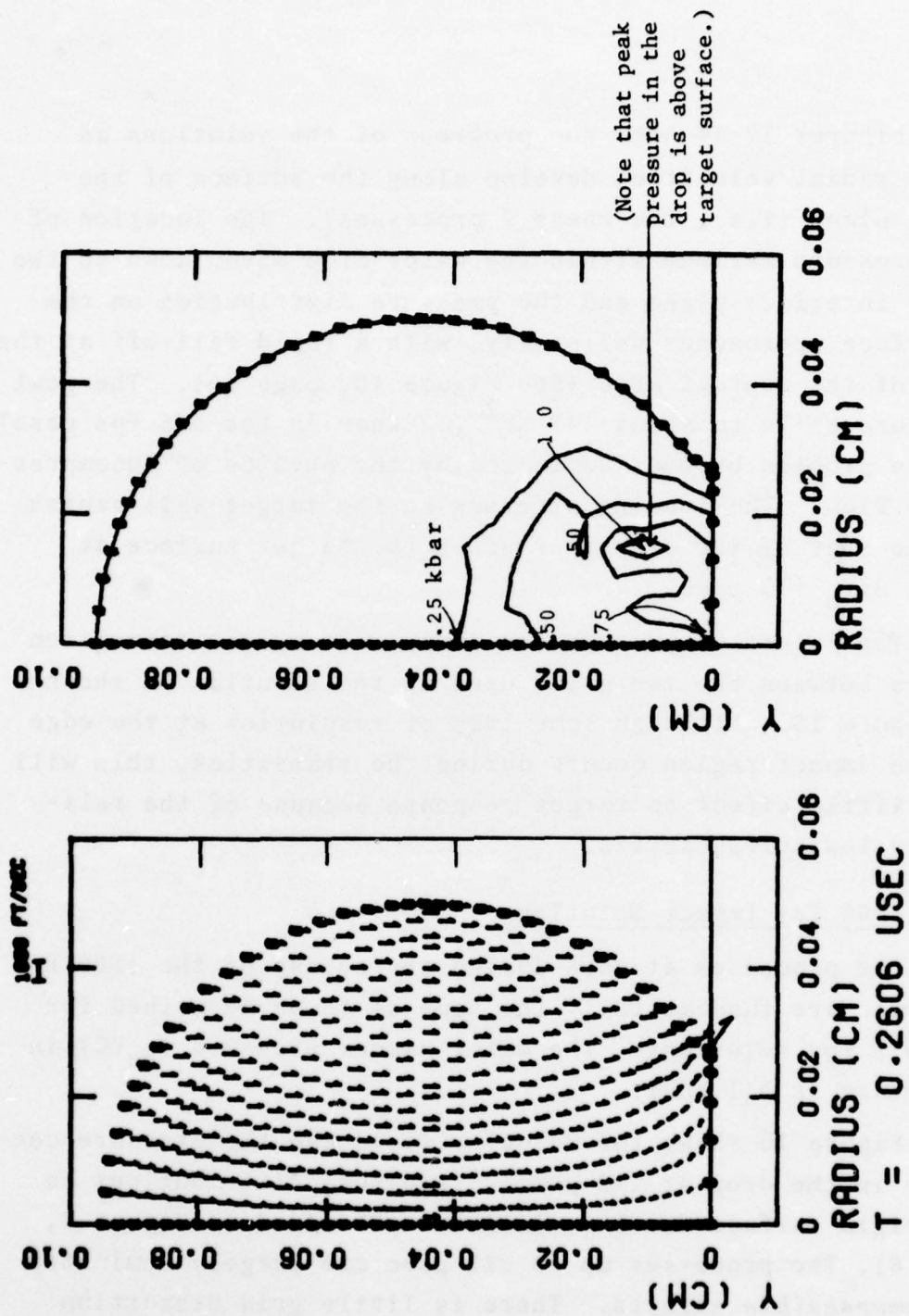


Figure 11. Velocity and Pressure Fields for 675 fps Water Drop Impact on a Rigid Surface at .26 μsec

Figures 12-14 show the progress of the solutions as large radial velocities develop along the surface of the rigid plane (i.e., the Phase 2 processes). The location of the pressure maximum within the water drop moves down to the rigid interface plane and the pressure distribution on the interface approaches uniformity, with a rapid fall-off at the edge of the contact area (see Figure 10, page 26). The peak pressure falls to about $1/2 \rho V^2$ (.2 Kbar in the 675 fps case) as the problem becomes dominated by the physics of incompressible flow. The loading stresses on the target will vanish as the rear of the drop approaches the target surface at about $D/V_0 = 5 \mu\text{sec}$.

The interface pressure vs radius during the transition cycles between the two grids used in the solution is shown in Figure 15. Although some loss of resolution at the edge of the impact region occurs during the transition, this will have little effect on target response because of the relatively low stress levels.

2.3 1100 fps Impact Solution

The processes at work during the course of the 1100 fps solution are fundamentally the same as those described for the 675 fps solutions. The water hammer pressure ($\rho_0 VC$) in this case is 5.1 Kbar.

Figure 16 shows the velocity field and the pressure contours in the drop at .12 μsec . (Pressure distributions on the rigid surface for this case are presented in Figure 4, page 8). The processes up to .12 μsec are largely dominated by *compressible* effects. There is little grid distortion (other than a flattening of the sphere at the bottom), and high pressures remain around the impact point. Some radial flow is apparent but it causes no significant distortion of the drop.

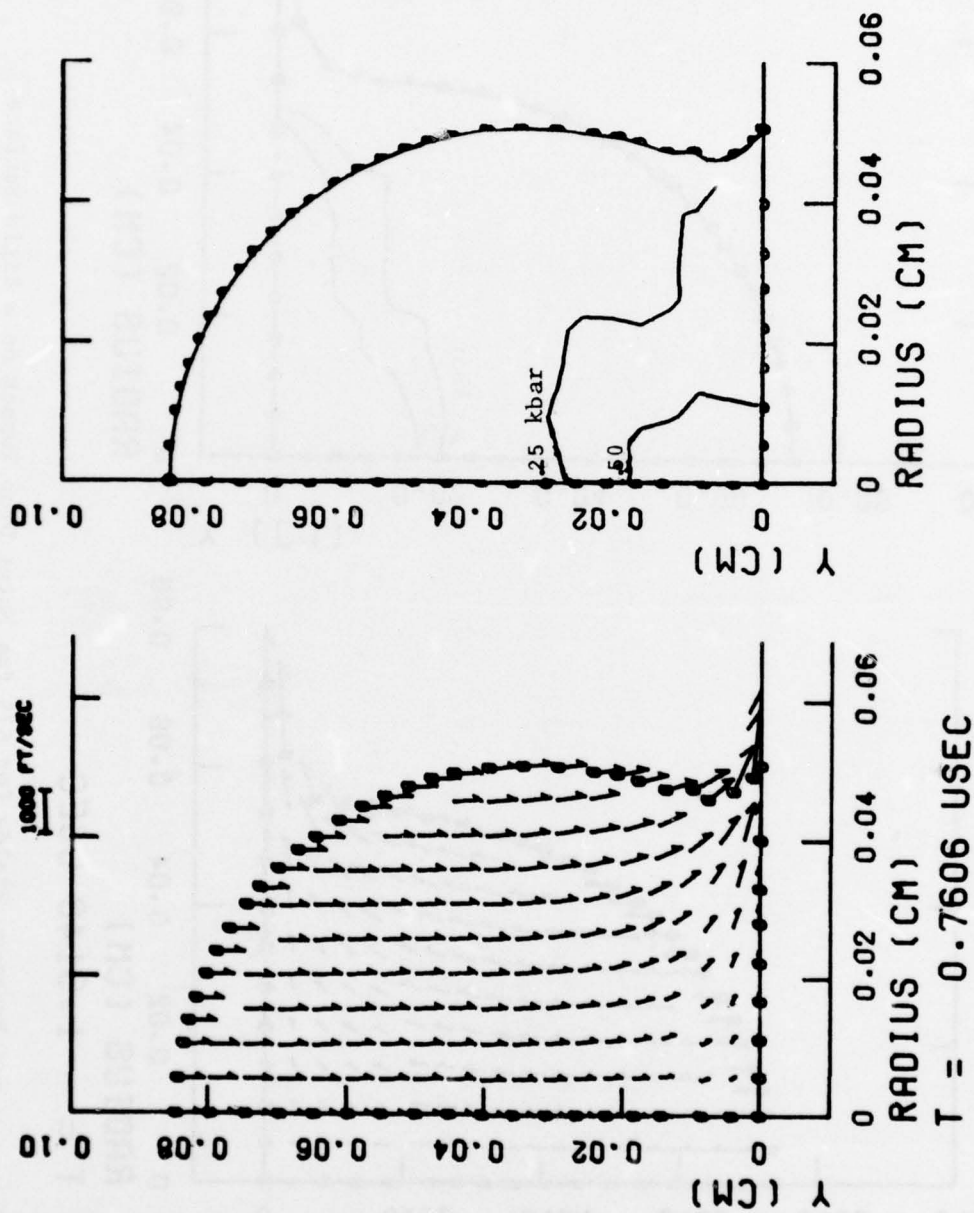


Figure 12. Velocity and Pressure Fields for 675 fps Water Drop Impact on a Rigid Surface at .76 usec

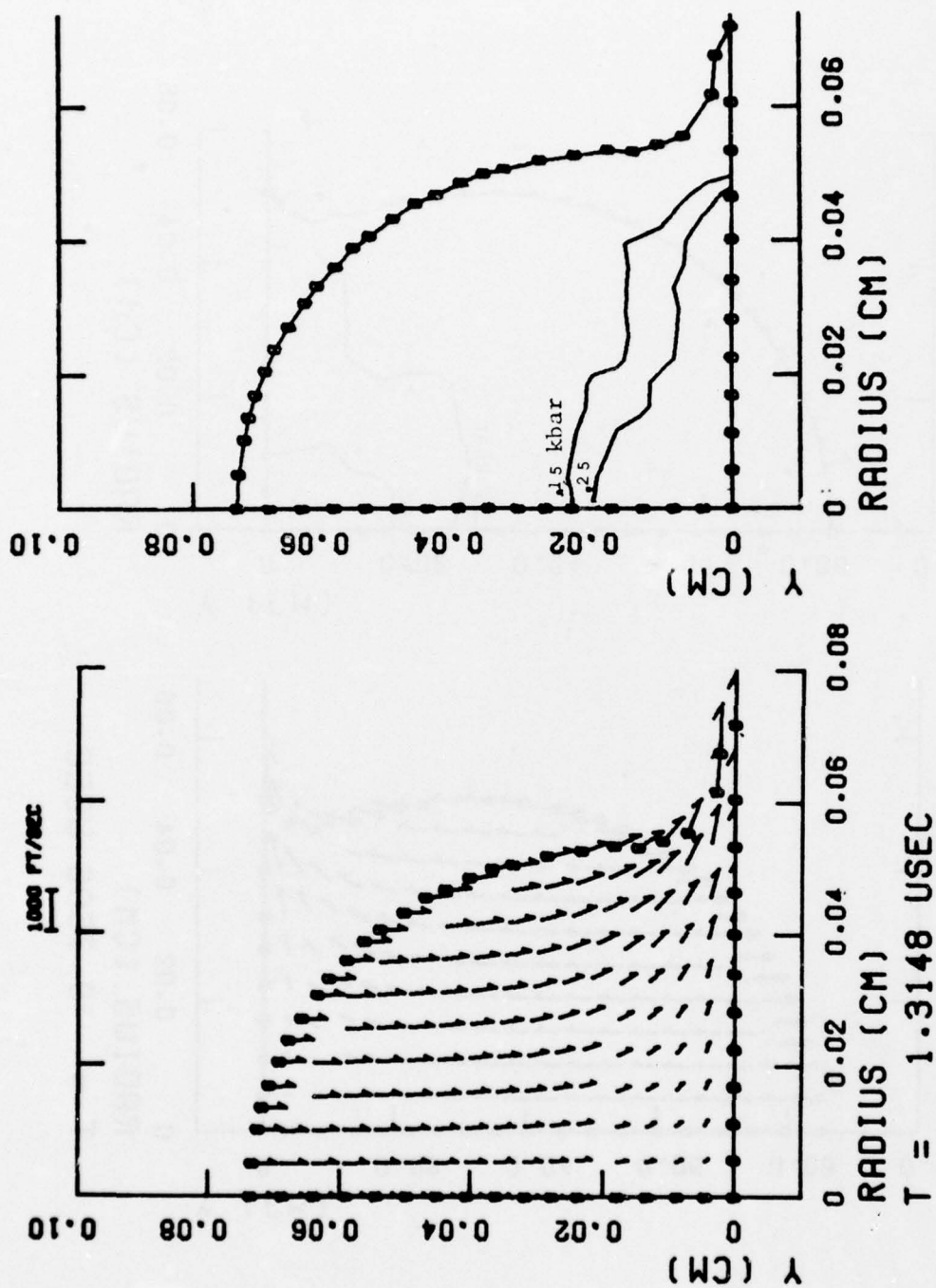


Figure 13. Velocity and Pressure Fields for 675 fps Water Drop Impact on a Rigid Surface at 1.31 μsec

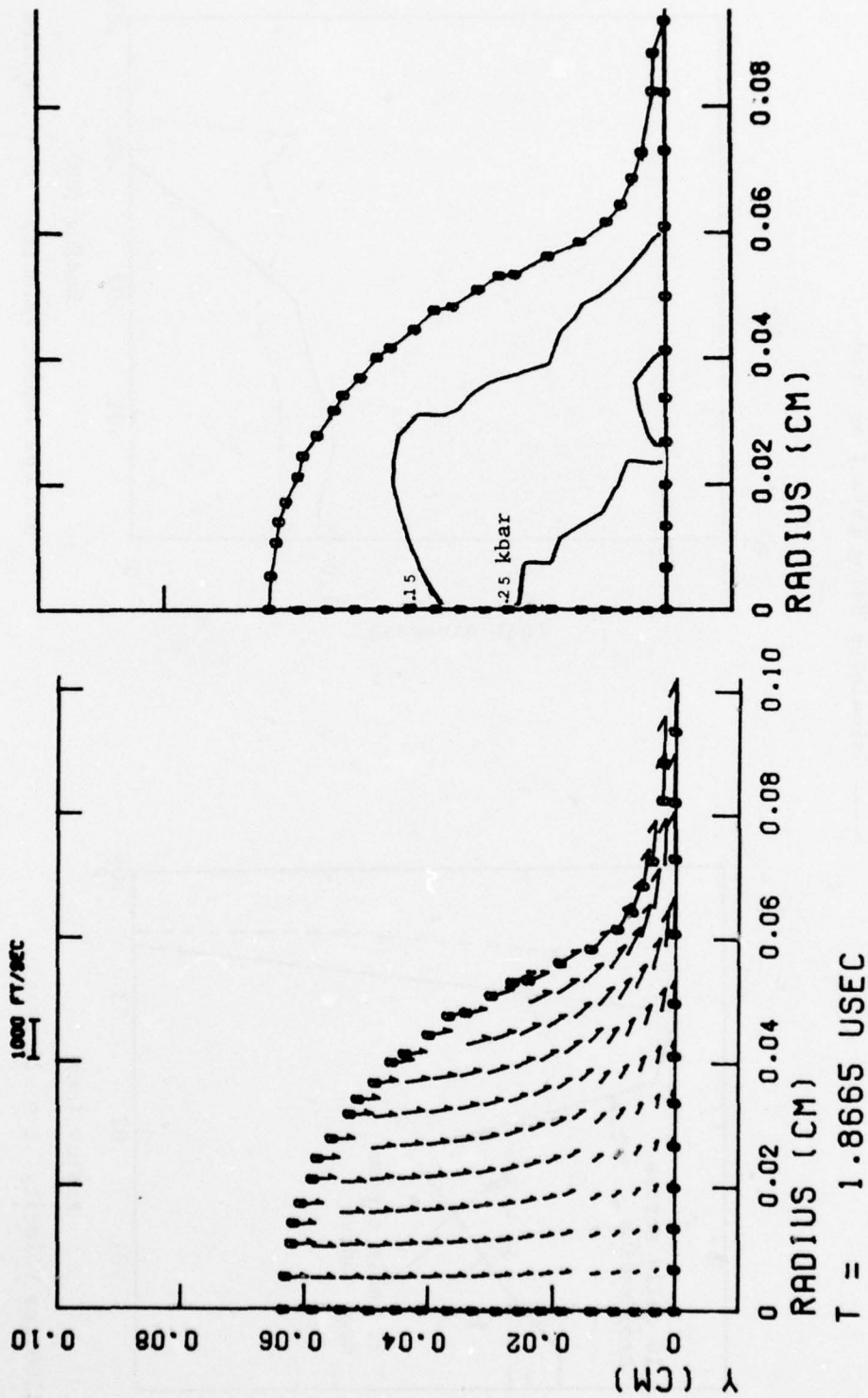


Figure 14. Velocity and Pressure Fields for 675 fps Water Drop Impact on a Rigid Surface at 1.87 μ sec

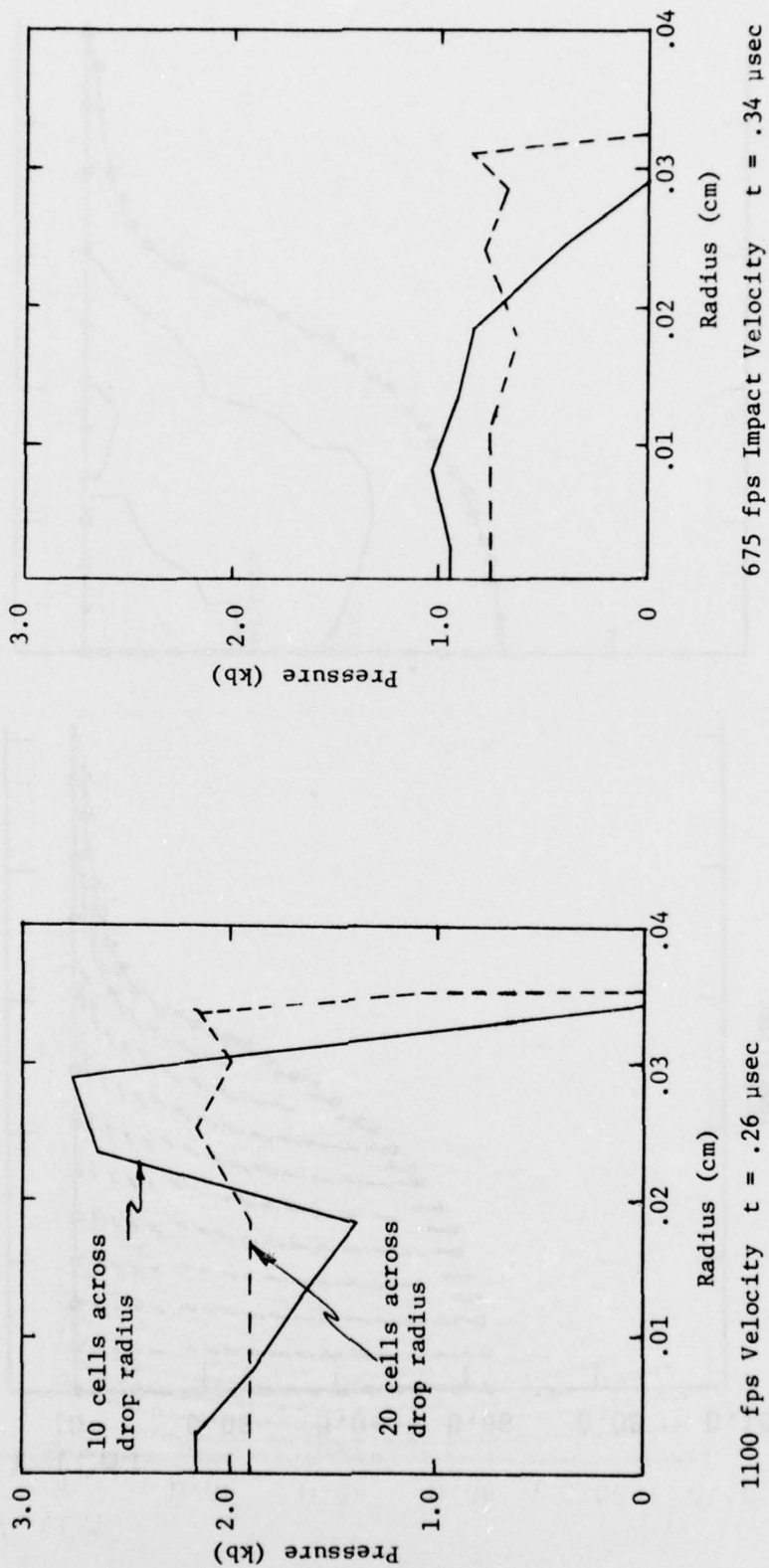


Figure 15. Pressure-Radius Profiles on Rigid Surface at Transition between Early and Late Time Computational Grids

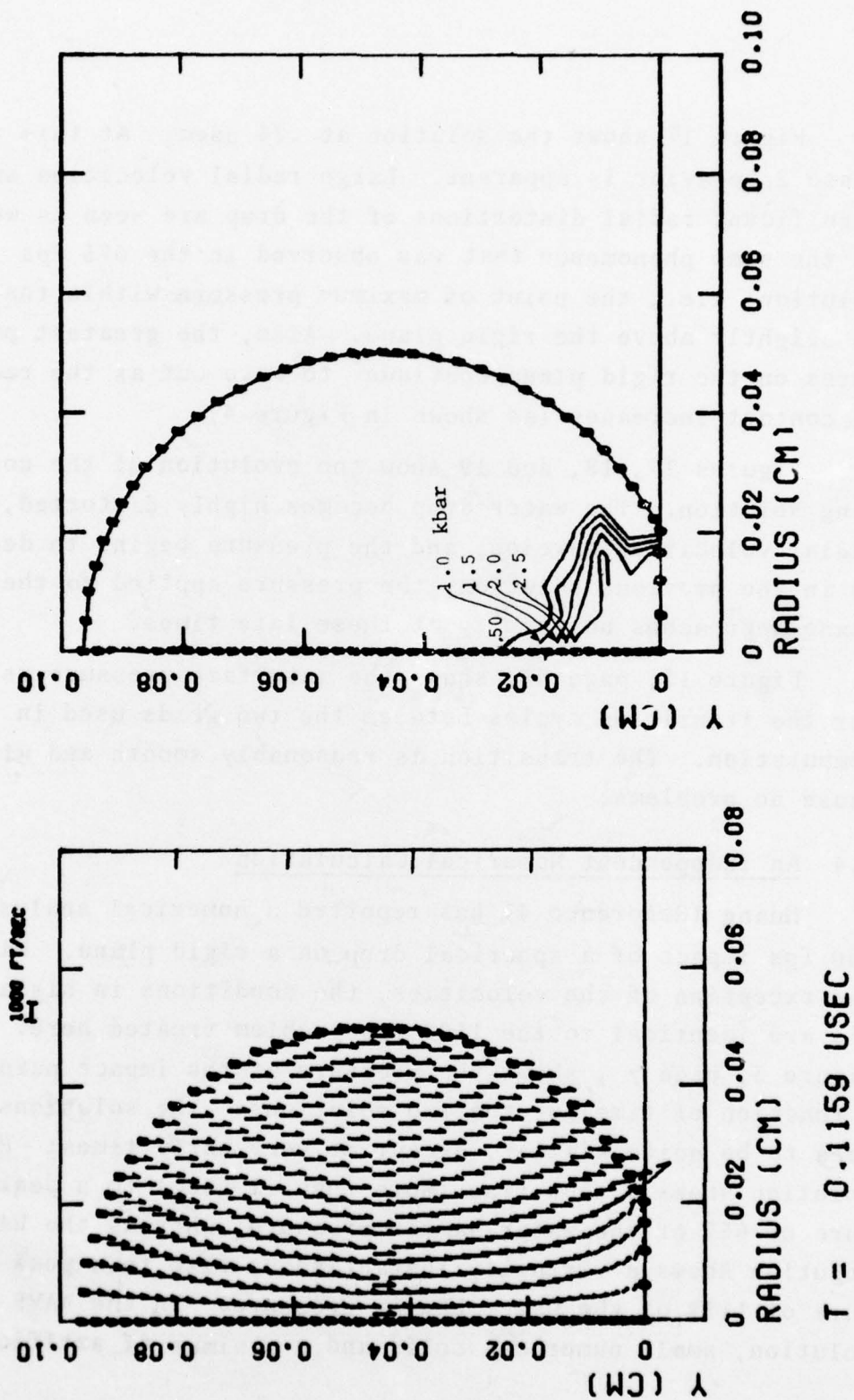


Figure 16. Velocity and Pressure Fields for 1100 fps Water Drop Impact on Rigid Surface at .12 μsec

Figure 17 shows the solution at $.24 \mu\text{sec}$. At this time Phase 2 behavior is apparent. Large radial velocities and significant radial distortions of the drop are seen as well as the same phenomenon that was observed in the 675 fps solution; i.e., the point of maximum pressure within the drop is slightly above the rigid plane. Also, the greatest pressures on the rigid plane continue to move out as the radius of contact increases (as shown in Figure 4).

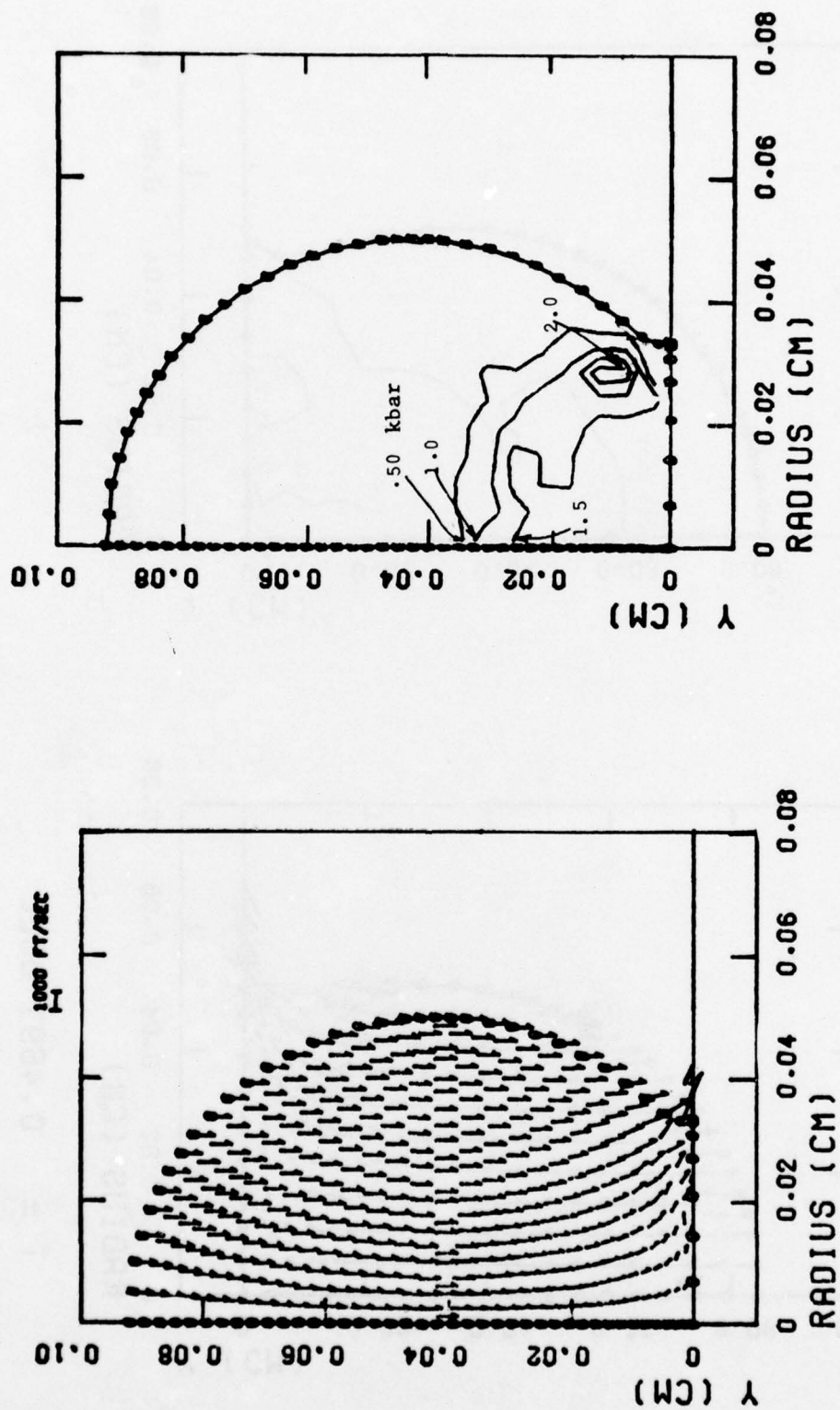
Figures 17, 18, and 19 show the evolution of the continuing solution. The water drop becomes highly distorted, large radial velocities develop, and the pressure begins to decrease. As in the previous solution, the pressure applied to the rigid plane approaches uniformity at these late times.

Figure 15, page 32, shows the interface pressure vs radius for the transition cycles between the two grids used in the computation. The transition is reasonably smooth and will cause no problems.

2.4 An Independent Numerical Calculation

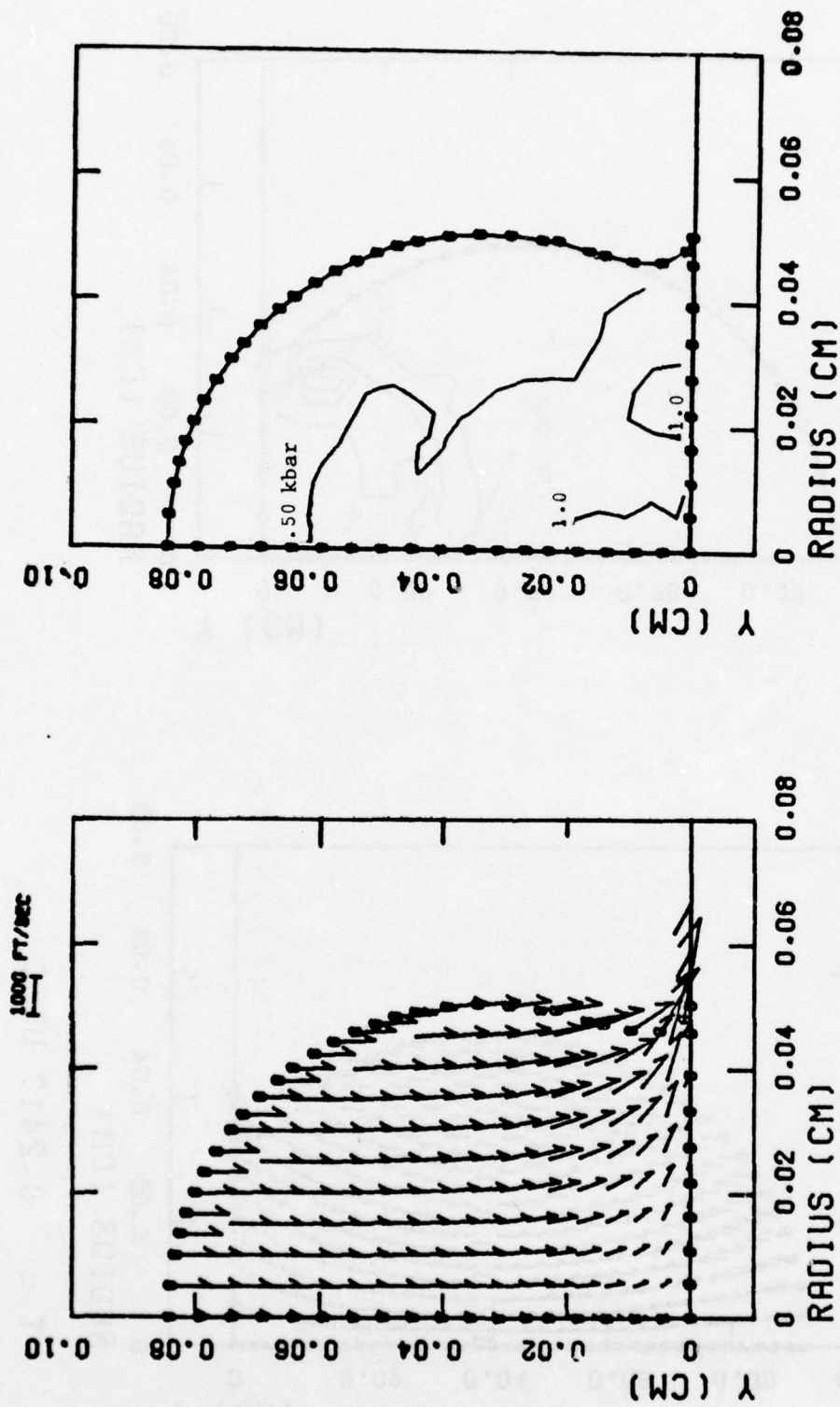
Huang (Reference 4) has reported a numerical analysis of the 980 fps impact of a spherical drop on a rigid plane. With the exception of the velocities, the conditions in his analysis are identical to the 1100 fps problem treated here.

Figure 3, page 7, shows the pressure at the impact point as a function of time for the two solutions. The solutions are seen to be quite similar, except at very early times: Huang's solution shows a slow rise (more than $.1 \mu\text{sec}$) to a peak pressure of 65% of the water hammer pressure, whereas the WAVE-L solution shows a virtually instantaneous rise to a peak pressure of 115% of the water hammer pressure. In the WAVE-L solution, small numerical cells and a minimum of artificial



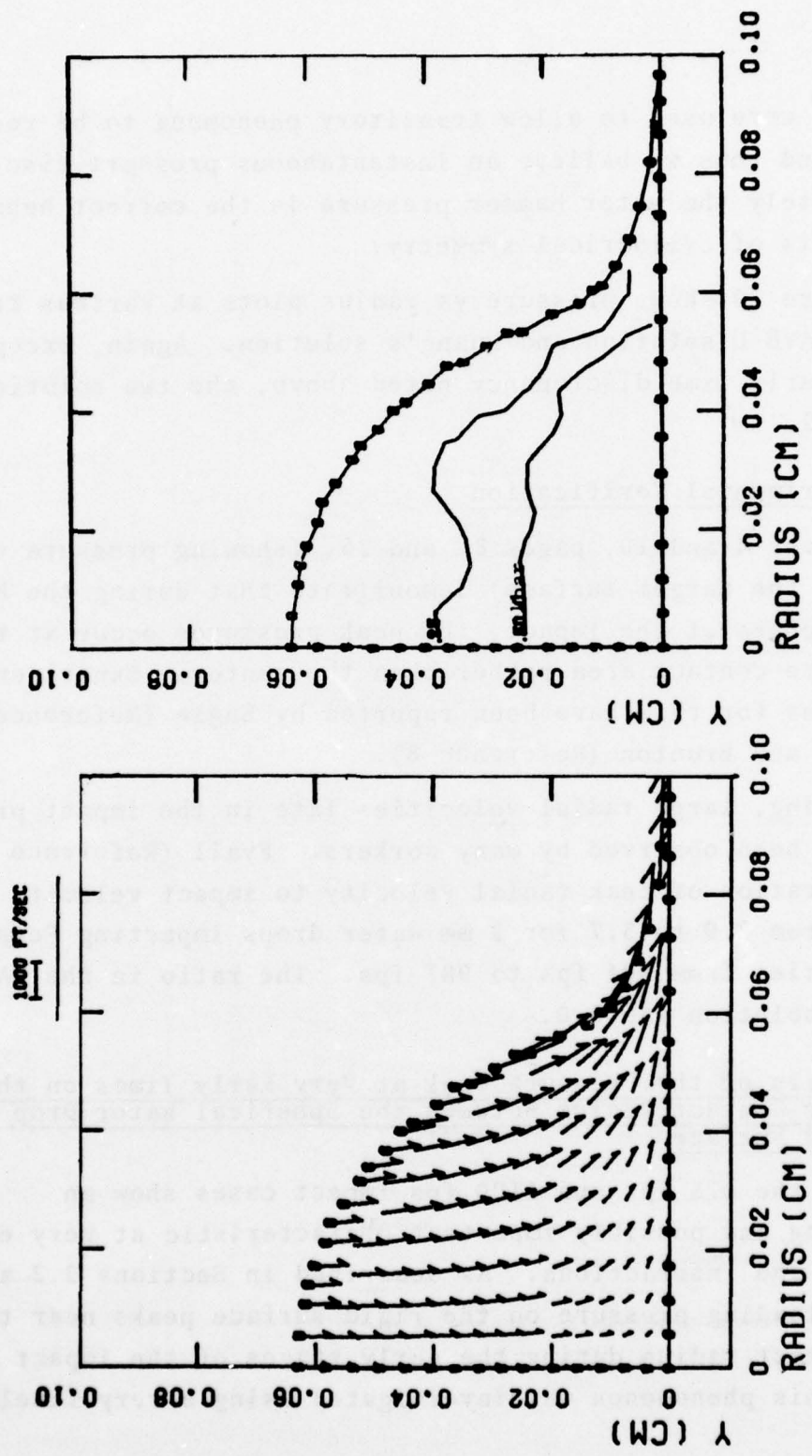
$t = 0.2417 \text{ USEC}$

Figure 17. Velocity and Pressure Fields for 1100 fps Water Drop Impact on a Rigid Surface at .24 μsec



$T = 0.4697 \text{ USEC}$

Figure 18. Velocity and Pressure Fields for 1100 fps Water Drop Impact on a Rigid Surface at .47 μsec



$T = 1.1565 \text{ USEC}$

Figure 19. Velocity and Pressure Fields for 1100 fps Water Drop Impact on a Rigid Surface at 1.16 μsec

viscosity were used to allow transitory phenomena to be resolved, and thus we believe an instantaneous pressure rise to approximately the water hammer pressure is the correct behavior on the axis of cylindrical symmetry.

Figure 20 shows pressure vs radius plots at various times for the WAVE-L solution and Huang's solution. Again, except for the early time discrepancy noted above, the two solutions agree well.

2.5 Experimental Verification

Figures 4 and 10, pages 8 and 26, (showing pressure vs radius on the target surface) demonstrate that during the high pressure phase of the impact, the peak pressures occur at the edge of the contact area rather than the center. Experimental indications for this have been reported by Engle (Reference 6) and Rochester and Brunton (Reference 8).

Jetting, large radial velocities late in the impact process, has been observed by many workers. Fyall (Reference 9) has reported ratios of peak radial velocity to impact velocity ranging from 2.9 to 3.7 for 2 mm water drops impacting Perspex at velocities from 904 fps to 987 fps. The ratio in the WAVE-L 1100 fps solution was 3.0.

2.6 Details of the Pressure Peak at Very Early Times on the Outer Contact Radius Between the Spherical Water Drop and Rigid Surface

Both the 675 fps and 1100 fps impact cases show an interesting and possibly important characteristic at very early stages of the interactions. As described in Sections 2.2 and 2.3, the loading pressure on the rigid surface peaks near the outer contact radius during the early stages of the impact event. This phenomenon was investigated using a very finely

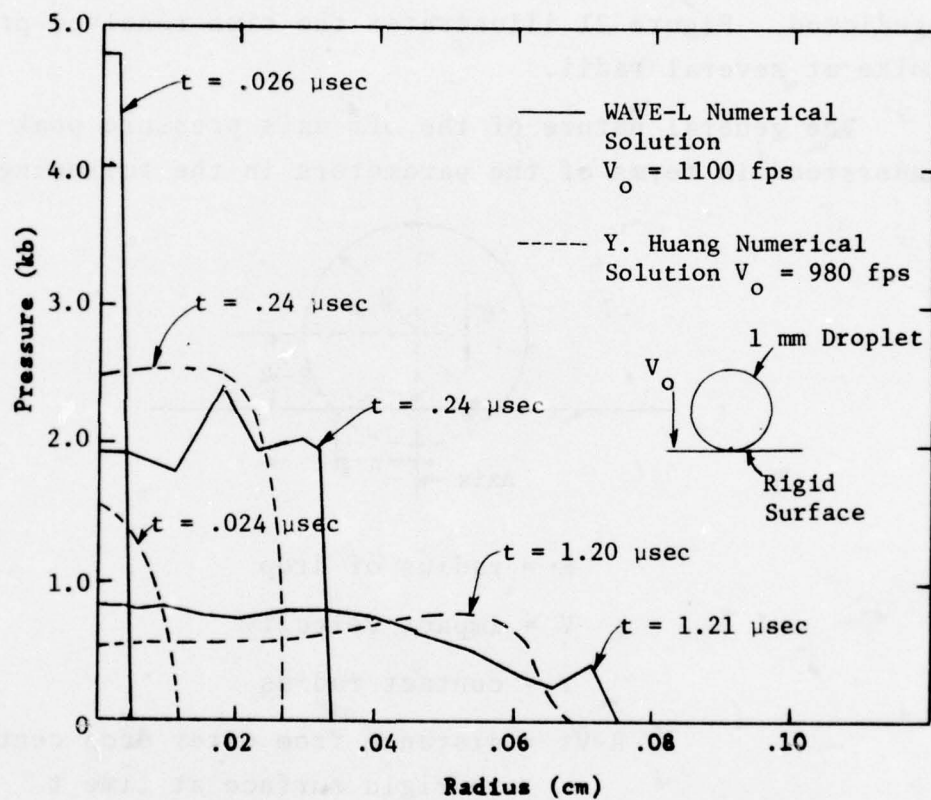
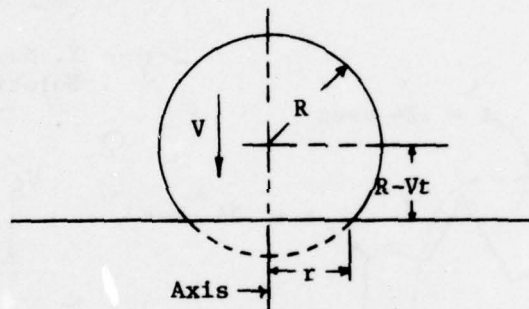


Figure 20. Pressure-Radius Profiles on a Rigid Surface for Water Drop Impact

zoned grid under a separate contract with Prototype Development Associates and the Office of Naval Research (Reference 10). A calculation was performed to obtain more detailed information on the target pressure load at very early times for a very finely resolved water drop impact at 1100 fps. In this study, a peak pressure of 2.65 times the water hammer pressure is predicted. Figure 21 illustrates the time resolved pressure spike at several radii.

The general nature of the off-axis pressure peak can be understood in terms of the parameters in the following sketch:



R = radius of drop

V = impact velocity

r = contact radius

$R-Vt$ = distance from water drop center
to rigid surface at time t

The following relationship is apparent:

$$r^2 + (R-Vt)^2 = R^2 \quad (2)$$

or in non-dimensional form

$$\left(\frac{r}{R}\right)^2 + \left(1 - \frac{Vt}{R}\right)^2 = 1 \quad (3)$$

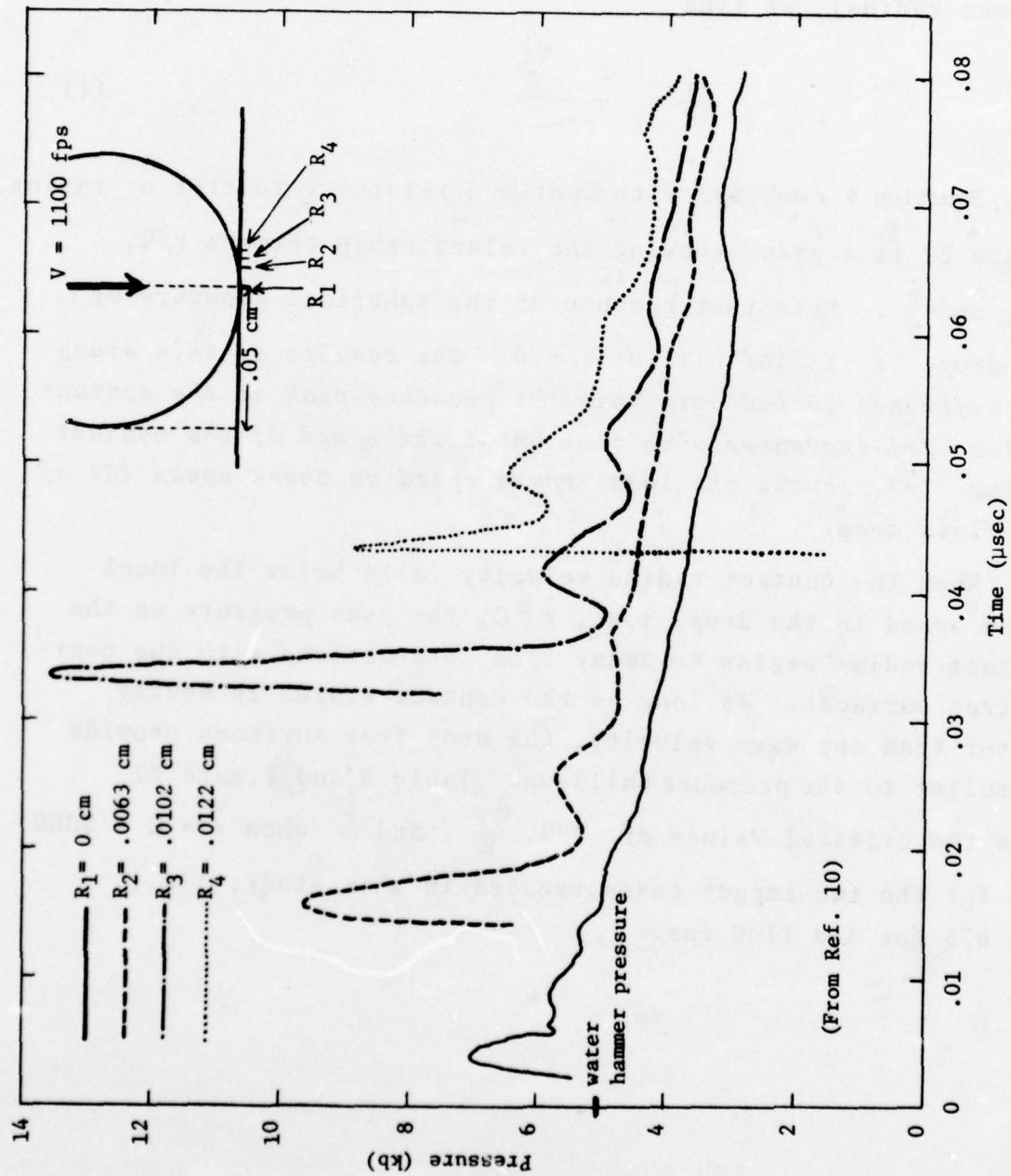


Figure 21. Pressure Peak Characteristics for 675 and 1100 fps Impact Cases at Very Early Times

Equation 3 represents the relationship between the contact radius (r) and time after impact (t). Taking the time derivative of Equation 3 and solving for $\frac{\dot{r}}{V}$ (where \dot{r} is the speed of the contact radius), we find

$$\frac{\dot{r}}{V} = \frac{1 - \frac{Vt}{R}}{r/R} \quad (4)$$

Thus, Equation 4 combined with Equation 3 relates $\frac{\dot{r}}{V}$ to time or radius. Figure 22 is a graph showing the relationship between r/R , $\frac{Vt}{R}$, and $\frac{\dot{r}}{V}$. Note that because of the spherical geometry of the drop, r is infinite at $t = 0$. *The results of this study and Reference 10 indicate that the pressure peak at the contact radius (r) increases with time until the speed of the contact radius (\dot{r}) equals the local sound speed or shock speed (C) of the fluid drop.*

When the contact radius velocity falls below the local sound speed in the drop, i.e., $\dot{r} < C$, the peak pressure on the contact radius begins to decay from interactions with the nearby free surfaces. As long as the contact radius is moving faster than any wave velocity, the drop free surfaces provide no relief to the pressure build-up. Table 3 and Figure 22 show the critical values of r/R , $\frac{Vt}{R}$, and $\frac{\dot{r}}{V}$ when $\dot{r} = C = 5000$ fps for the two impact cases treated in this study, i.e., $V = 675$ fps and 1100 fps.

TABLE 3. CRITICAL WATER DROP PARAMETERS WHEN $\dot{r} = C = 5000$ FPS FOR $V = 675$ AND 1100 FPS

	$V = C = 675$ fps (0.020514 cm/ μ sec)	$V = 1100$ fps (0.033528 cm/ μ sec)
\dot{r}/V	7.41	4.55
r/R	0.13	0.22
Vt/R	0.009 ($t=0.022$ μ sec for $R=0.05$ cm)	0.023 ($t=0.034$ μ sec for $R=0.05$ cm)

Thus, the peak pressure spike occurs early in the drop-target interaction process and at radii which are only 13% and 22% of the drop radius for 675 and 1100 fps water drop impacts, respectively. The predicted time and location of the pressure spike agrees very well with the results shown in Figure 21.

2.7 Comparison of Impacts of a Water Drop on a Rigid Target and on a Znse Window

When the pressure applied to the window by the impacting water drop begins to decay, relief waves propagate into the window material and the window "rebounds". As a validation of the assumption that water impact loading on a rigid surface is essentially the same as water impact loading on an IR window (in the velocity range of interest) a solution of a water drop impacting directly on a window surface was obtained.

Figure 23 shows the initial conditions for this solution. The grid design in the water drop is identical to that used at early times in the rigid surface solution (i.e., Figure 8A).

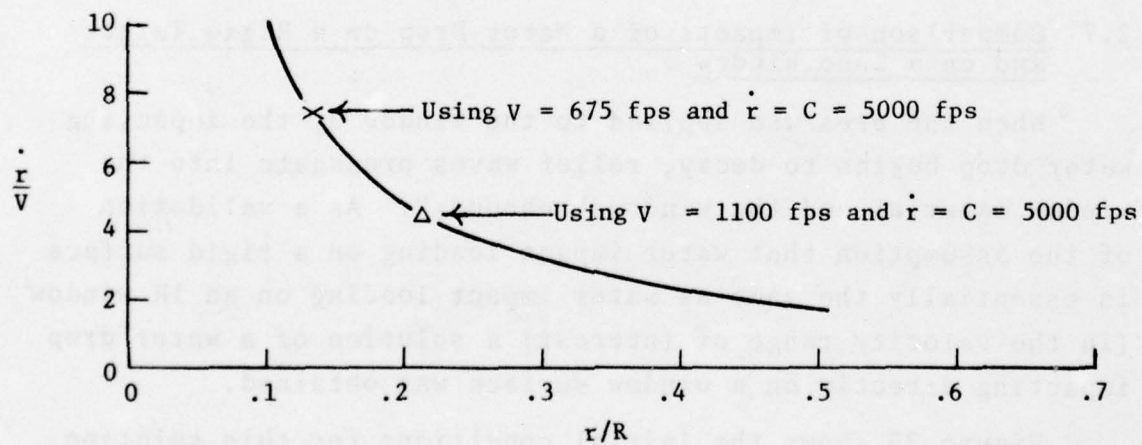
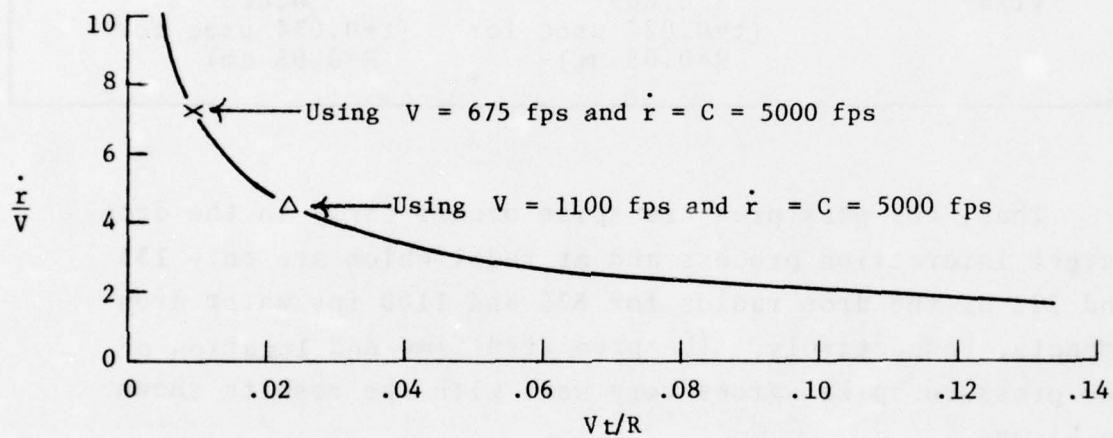
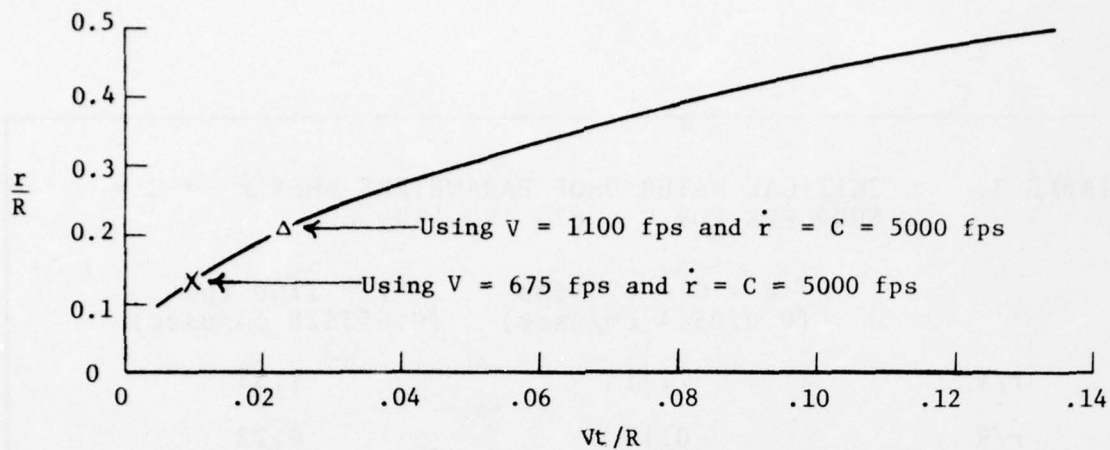


Figure 22. Relationship between Non-Dimensional Contact Radius, (r/R) , Time, (Vt/R) , and Velocity of Contact Radius (\dot{r}/V)

The initial velocity of the drop is 1100 fps. The window is .32 cm thick ZnSe, with 64 cells across the thickness. The two grid lines which comprise the interface between the water drop and the window are frictionless slide lines, which means they can freely slip along one another. In the radial direction the grid extends to .6 cm (the entire grid is not shown in Figure 23).

Figure 24 compares the velocity field from this solution at .26 μ sec with that of the 1100 fps rigid surface impact described previously. They are almost identical. Figure 25 compares the interface pressure functions for the two solutions at .26 μ sec, and except for numerical oscillations, there is no substantial difference.

By .26 μ sec the peak pressures in the 1100 fps impact case have decayed from almost 6 Kbar to less than 2.5 Kbar, and the window material at the impact point has begun to *rebound* after negligible displacement. If the deformation of the window were going to affect the interface loading, this would have become evident by this time. Consequently, we conclude that the rigid surface concept is valid in the 1100 fps velocity regime, and that the impact pressure function determined using a rigid surface can be used to load elastic windows without alteration.

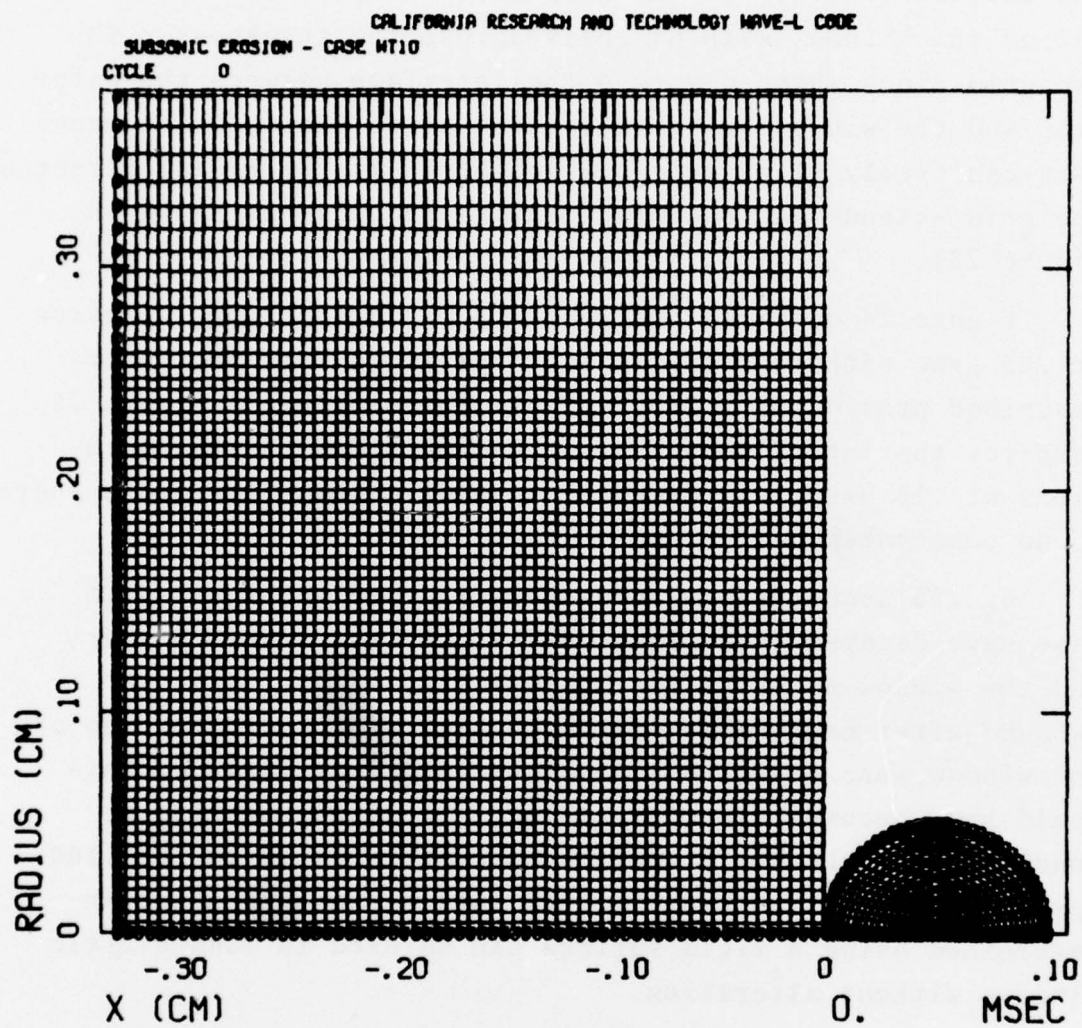


Figure 23. Initial Grid Configuration for 1100 fps Impact of Water Drop

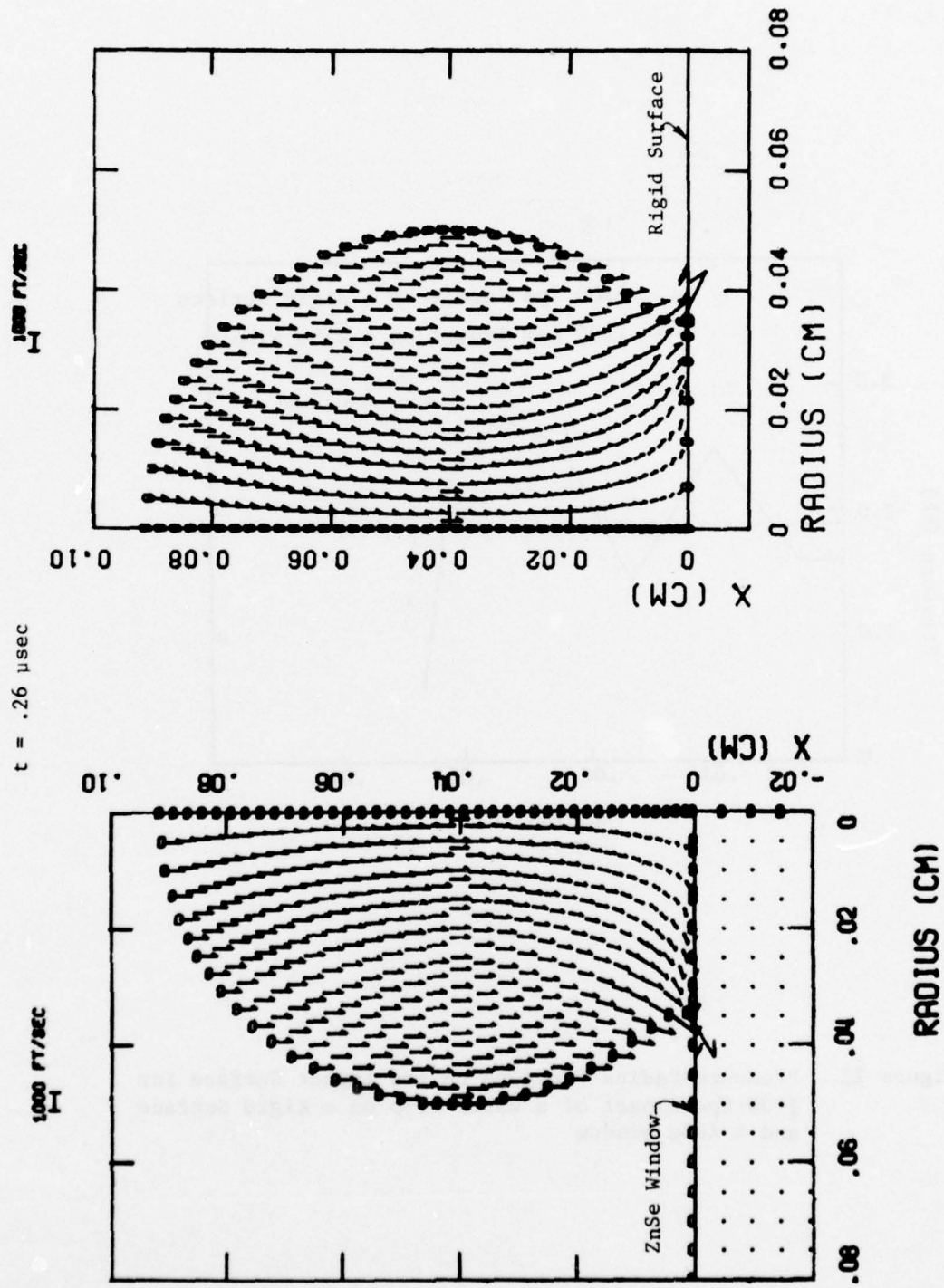


Figure 24. Velocity Field Comparison at .26 μsec for 1100 fps Water Drop Impact on ZnSe Window and on a Rigid Surface

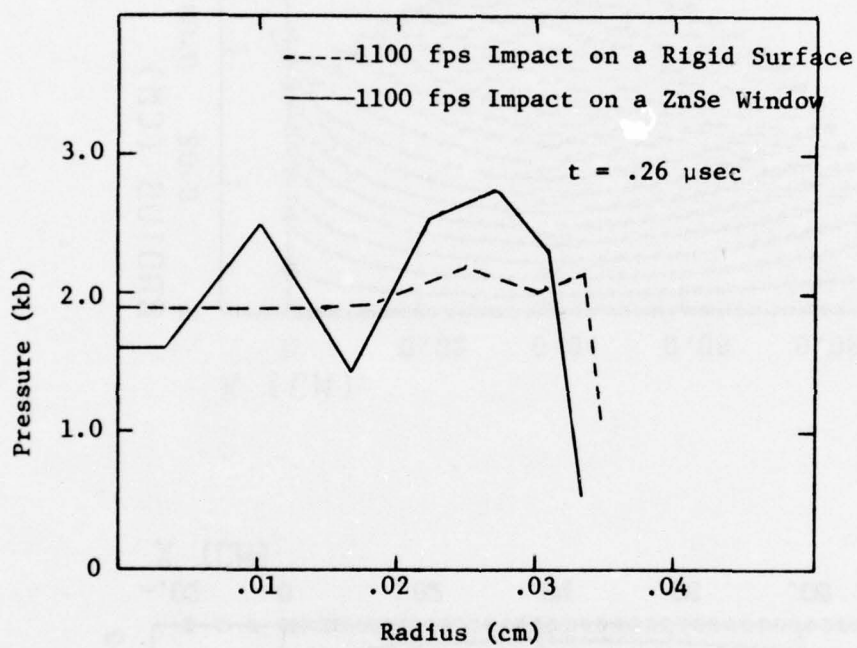


Figure 25. Pressure-Radius Profiles on the Impact Surface for 1100 fps Impact of a Water Drop on a Rigid Surface and a ZnSe Window

SECTION III

MATERIAL PROPERTIES

The baseline material for this study is ZnSe in a form suitable for the construction of optical components from the Eastman Kodak Company, under the name IRTRAN 4, and from the Raytheon Corporation. IRTRAN 4 is made by subjecting a ZnSe powder to heat and pressure while bulk diffusion and plastic flow take place and a glass-like form of the material is produced. The Raytheon product is produced by a chemical vapor deposition process. References 11-18 were reviewed to determine the properties of the various types of available ZnSe. In addition, pertinent information was obtained by private communications with J. Pappis of the Raytheon Corporation; Roy Rice of the Naval Research Lab; John Wurst of the University of Dayton; and A. G. Evans of the Rockwell Science Center. The results of these inquiries are summarized in Table 4.

ZnSe is modeled in the computer solutions as a linear elastic material with Young's Modulus and Poisson's Ratio as given in Table 4. (These imply a bulk modulus $K = 574$ Kbar.) Plastic behavior has not been observed in ZnSe, though experimental data are available only for failure in tension. We have assumed that at the stress levels of interest in the present effort compressive yielding does not occur. Fracture is allowed to occur, with the width and trajectory of any crack that forms being determined by the local stress field. The stress field itself will be appropriately affected by the existence of the fracture.

As a part of this effort, the properties of calcium aluminosilicate glass were compared with ZnSe to determine if it would respond similarly to water drop impact. A positive finding would allow the use of calcium aluminosilicate glass

TABLE 4

PROPERTIES OF ZnSe and CALCIUM ALUMINO-SILICATE GLASS

Material	Kodak IRTRAN 4 ZnSe	Raytheon CVD ZnSe	Cortran 9753
Density	5.27 gm/cm ³	5.27 g/cm ³	2.798 g/cm ³
Refractive Index	2.40 ($\lambda=8-13\mu$)	2.40 ($\lambda=8-13\mu$)	1.61251 ($\lambda=.4861\mu$)
10.6 μ Optical Absorption	.13 cm ⁻¹	1-3x10 ⁻³ cm ⁻¹	
Hardness (Knoop)	150	95-140	657.5 (100g) 601 (500g)
Flexural Strength	7500 (250°C) 6000 (RT)	4.0 - 8.6 ksi	
Fracture Energy		3-6J/m ²	
Young's Modulus	10.3 x 10 ⁶ psi	10.0 x 10 ⁶ psi	14.3 x 10 ⁶ psi
Poisson's Ratio		.30	.28
Specific Heat		.084 cal/g°C	
Mean Grain Size		50 μ m	
Modulus of Rupture	6000-7500 psi	5600-7500 psi	8000-9000 psi
Dilatational Sound Speed		.42 cm/ μ sec	.67 cm/ μ sec
Stress Intensity Factor, K _I		600-1300 psi $\sqrt{\text{in}}$	

in experimental comparisons, since glass is more economical and has superior optical characteristics. The particular glass chosen for the comparison was Corning's CORTAN 9753, whose properties are listed in Table 4.

Comparing the values in Table 4, we note the following:

- o The density of ZnSe is almost twice that of CORTAN 9753 glass. This is a serious dissimilarity, since it means that any inertial effects will be substantially different.
- o Both the Knoop hardness and the modulus of rupture of the 9753 glass are greater than those of ZnSe, indicating a higher fracture resistance in the glass.
- o The sound speed in 9753 glass is about 60% greater than that of ZnSe. This would lead to differences in the timing of the various stress wave interactions (though these might be remedied by scaling the window thickness and/or the drop size accordingly).

In addition, Schmitt (Reference 1) has obtained experimental results in which both ZnSe and CORTAN 9753 glass were subjected to erosion by water drop impact. Photographs of the eroded surfaces indicate that significantly different processes are governing the erosion of the two materials.

The property differences between ZnSe and CORTAN 9753, together with Adler's data, suggest that ZnSe should be used instead of 9753 glass in any experimental comparisons despite the associated costs.

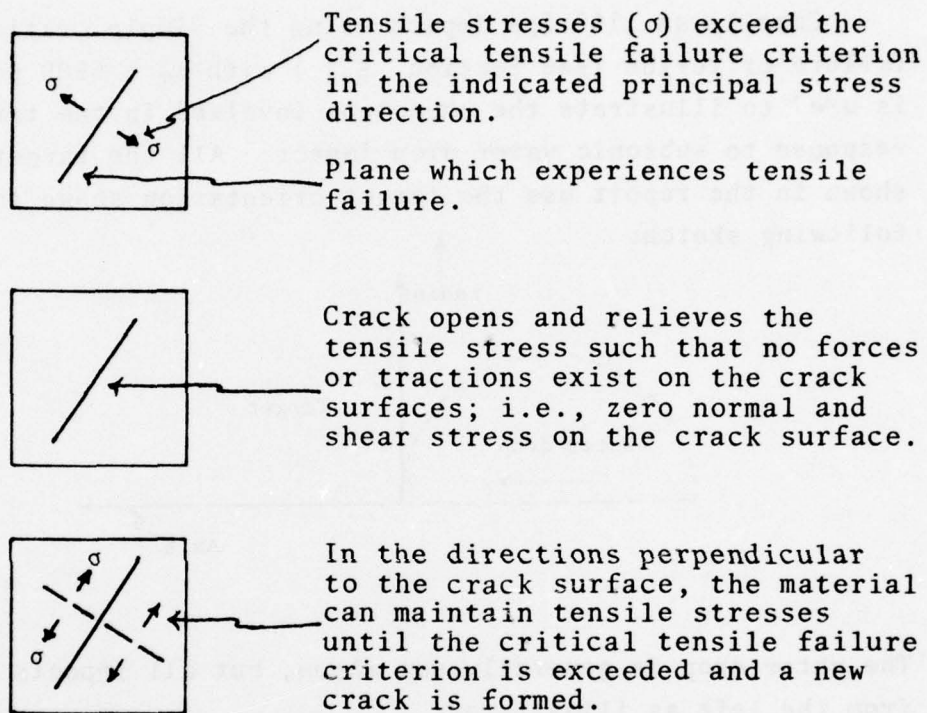
SECTION IV

PHENOMENOLOGY OF TARGET RESPONSE TO WATER DROP IMPACTS

All of the target response problems were run using the WAVE-L computer code, and all used the impact loading functions described in Sections 2.2 and 2.3. The water drop is represented as a *pressure-boundary condition on the ZnSe plate* and does not explicitly appear in the computational grid. The numerical solutions therefore become easier and less expensive.

ZnSe in the solutions was modeled as an elastic material (implying Young's Modulus $E = 10 \times 10^6$ psi and Poisson's Ratio $\nu = .3$, with bulk modulus $K = 574$ Kbar, shear modulus $G = 265$ Kbar) *but the ZnSe was allowed to fail by undergoing tensile fracture when the maximum principal stress or stress history in any cell exceeded some failure criterion.*

The WAVE-L code has the capacity to allow the formation of tensile cracks, to calculate the width of the cracks, to make appropriate changes in residual properties of adjacent material, and to appropriately adjust stresses adjacent to the cracks. After a cell has cracked, no tensile stress across the crack is permitted, and no shear stresses are permitted on the crack if the crack is open (the width of the crack is continuously monitored). These stress adjustments are important because a crack frequently alters the local stress field in such a way as to enhance its own growth; thus, any realistic method of predicting crack growth must consider the altered stress field. Each computational cell is allowed to develop up to two cracks. If a third crack forms, the cell is considered to be completely shattered, and no tension at all is thereafter allowed. The general treatment of tensile failure and the plotting conventions used to indicate the cracked cells in the computational grid plots are illustrated in Figure 26.



Plotting Convention:






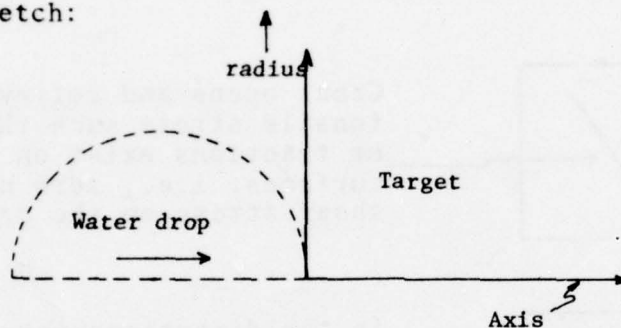
-  Single crack in r-z plane. The line is plotted in the direction of the crack (normal to the principal stress causing the crack).
-  Hoop crack; i.e., $\sigma_{\theta\theta} > \sigma_c$ caused the crack.
-  Hoop and r-z plane crack.
-  Two r-z plane cracks; only hoop tension is permitted.
-  Completely fractured - no tension permitted.

Figure 26. Treatment of Tensile Cracks in WAVE-L Code

Case 1, an 1100 fps impact using the simple critical stress failure criterion (see Section 5.1) with $\sigma_T = 6500$ psi, is used to illustrate the phenomena involved in the target response to subsonic water drop impact. All the target plots shown in the report use the target orientation shown in the following sketch:



The water drop is generally *not shown*, but all impacts are from the left as illustrated.

Figure 27 shows the evolution of the cracks in Case 1 as the solution progresses. The radial cracks are initiated on the surface at a radius of about .025 cm (one-half the radius of the impacting drop) and extend outward at an angle of about 45° to the surface of the window. This is consistent with Adler's (Reference 19), experimental observations for water drop impacts on ZnSe, which show a distribution of concentric ring fractures.

The location of the shear wave fronts ($C_s = .224$ cm/ μ sec) in Figure 27 suggests that the tensile cracks form and propagate behind the shear wave front. Figure 5, page 10, identifies two discrete cracks in the final crack pattern for Case 1 and shows crack length vs time for these cracks. These results demonstrate that the cracks propagate at a major fraction of

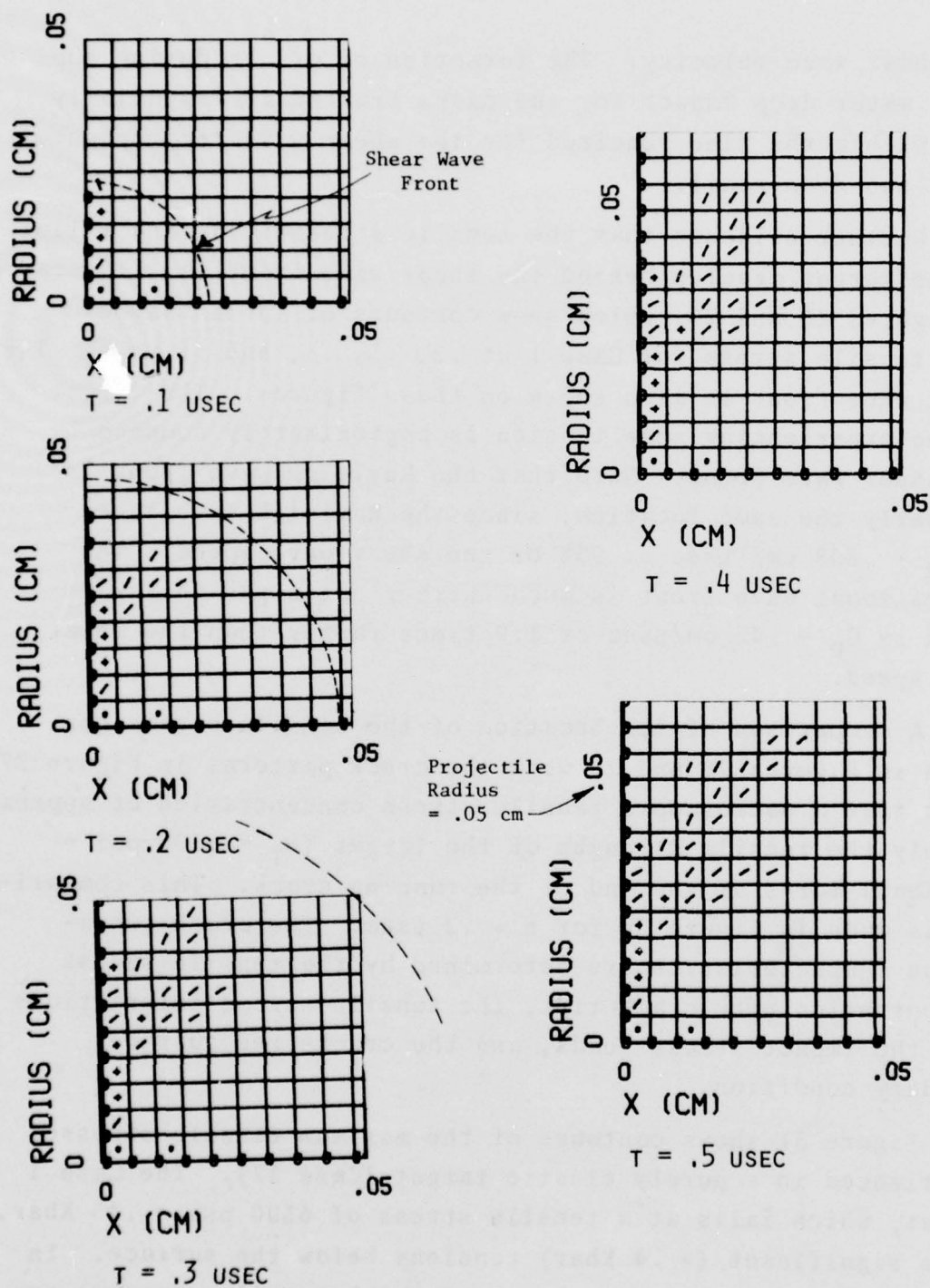


Figure 27. Crack configuration at Various times from Numerical Solution of 1100 fps Water Impact on ZnSe Window

the shear wave velocity. The formation of cracks during subsonic water drop impact for the cases treated is essentially over within the time required for the shear wave to propagate about two drop radii.

Further evidence that the tensile stresses causing failure in the target develop behind the shear wave front is illustrated in Figures 28 and 29, which show contours of instantaneous peak tensile stress for Case 1 at .2, .3, .4, and .5 μsec . The shear wave front is also shown on these figures. The target volume experiencing some tension is approximately bounded by the shear wave front. Note that the Rayleigh wave front is at nearly the same location, since the Rayleigh wave speed is $C_R = .208 \text{ cm}/\mu\text{sec}$ or 93% of the shear wave speed. The dilatational wave front is much farther out since this wave speed is $C_D = .42 \text{ cm}/\mu\text{sec}$ or 1.9 times faster than the shear wave speed.

A comparison of the location of the tensile stress contours in Figures 28 and 29 with the crack patterns in Figure 27 shows that a macroscopic tensile stress concentration of approximately the tensile strength of the target ($\sigma_T = 6500 \text{ psi} = .45 \text{ Kbar}$) forms at the end of the running crack. This comparison is made in Figure 30 for $t = .2 \mu\text{sec}$. The crack propagation characteristics are determined by the tensile stress concentration near crack tips, the tensile stress interactions with the impact stress loads, and the crack-free surface boundary condition.

Figure 31 shows contours of the maximum tensile stresses experienced in a purely elastic target (Case 17). The Case 1 target, which fails at a tensile stress of $6500 \text{ psi} = .45 \text{ Kbar}$, shows significant ($> .4 \text{ Kbar}$) tensions below the surface. In the elastic case, on the other hand, high tensile stresses are present only near the target surface.

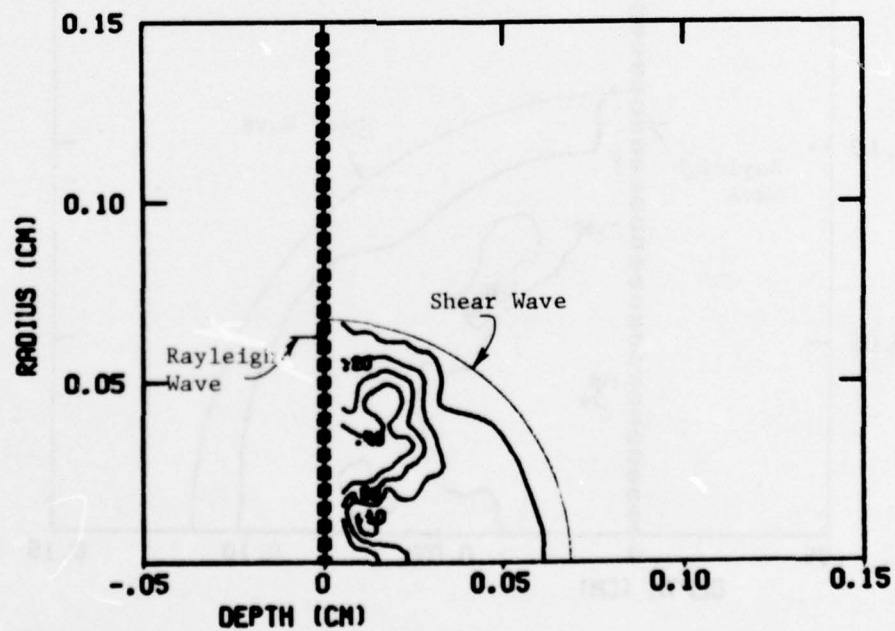
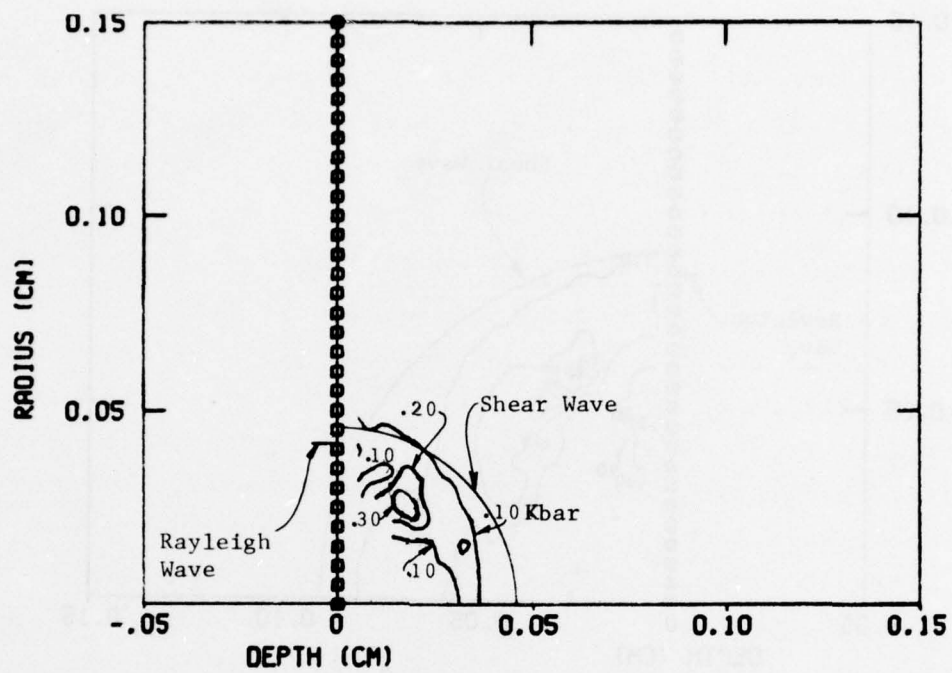


Figure 28. Contours of Peak Tensile Principal Stress for 1100 fps Water Drop Impact on ZnSe Window at .20 and .30 μ sec

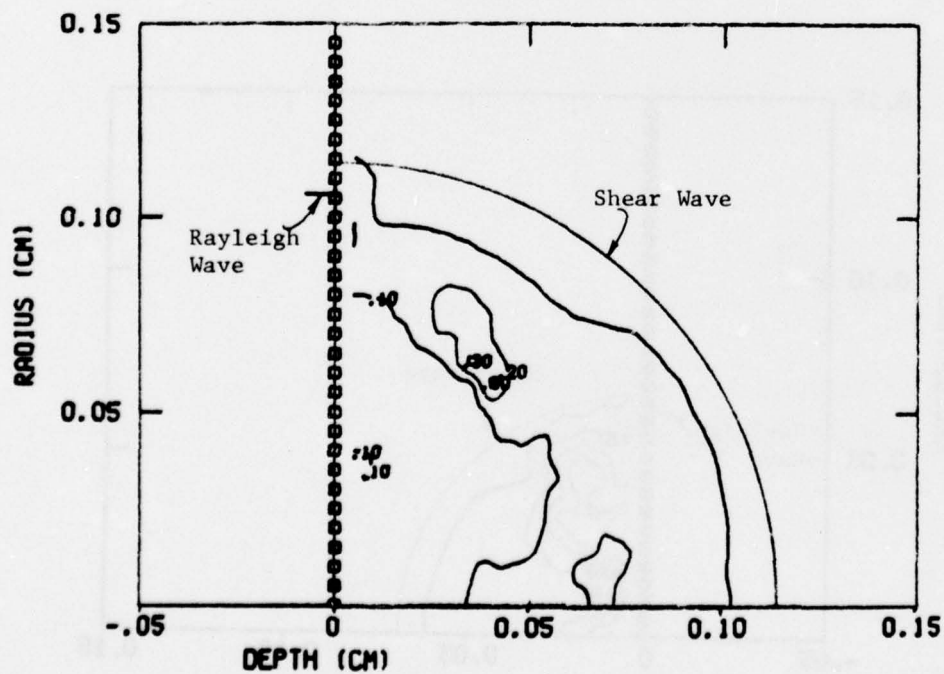
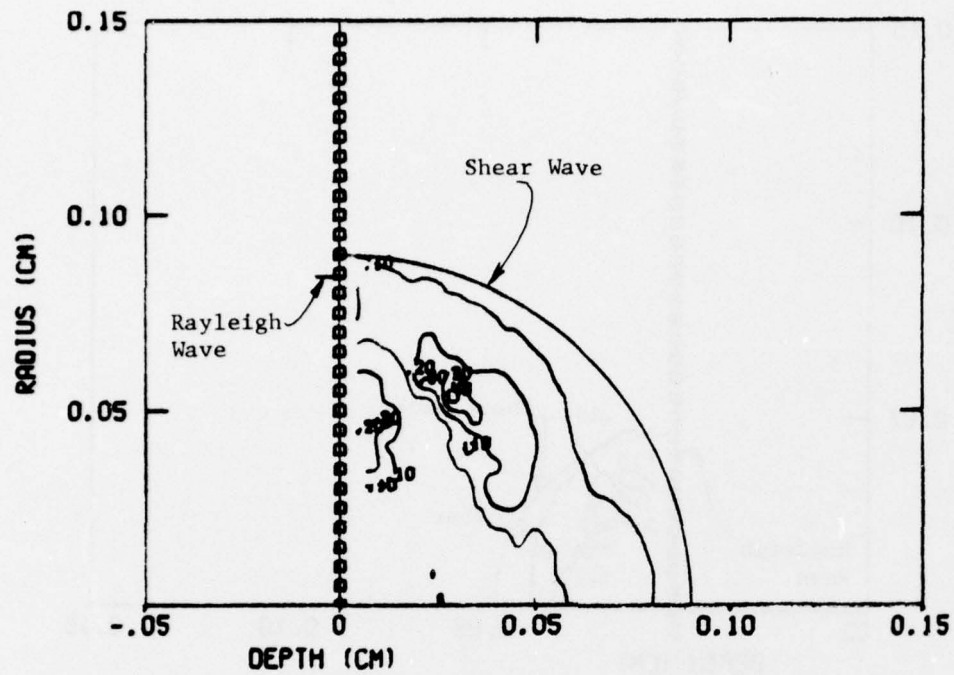


Figure 29. Contours of Peak Tensile Principal Stress for 1100 fps Water Drop Impact on ZnSe Window at .40 and .50 μ sec

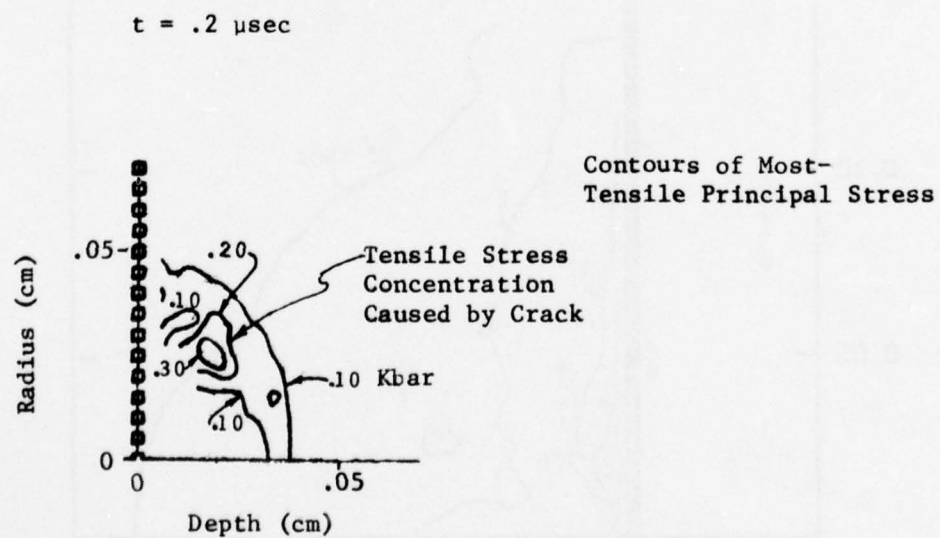
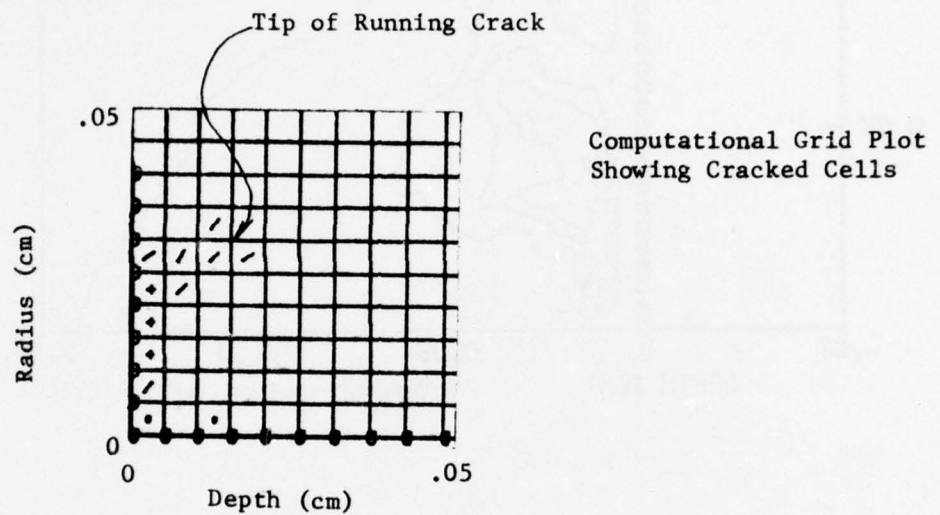


Figure 30. Computational Grid and Peak Tensile Principal Stress Contours for 1100 fps Water Drop Impact on ZnSe Window at $.2 \mu\text{sec}$

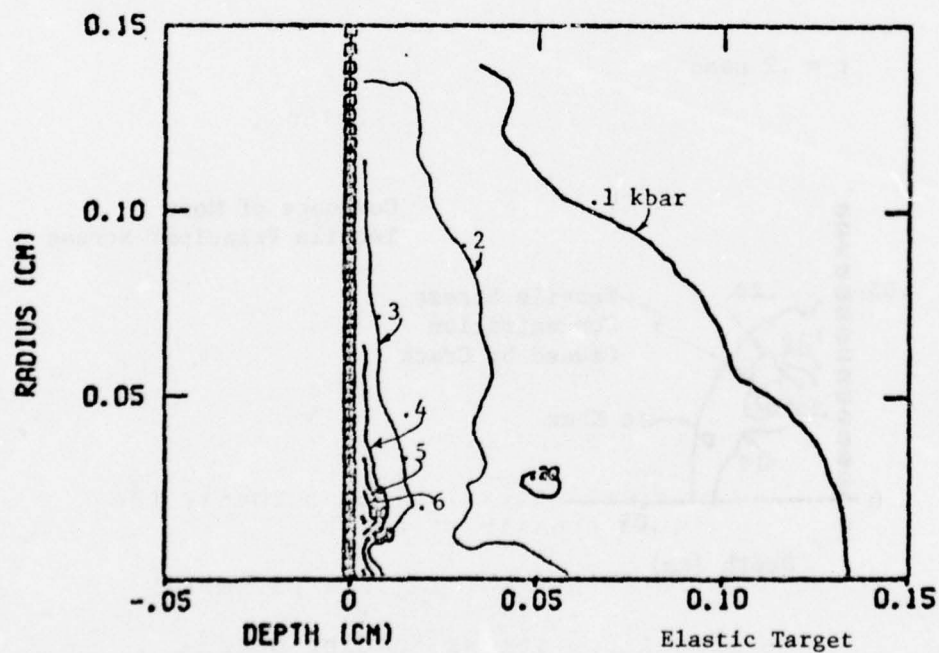
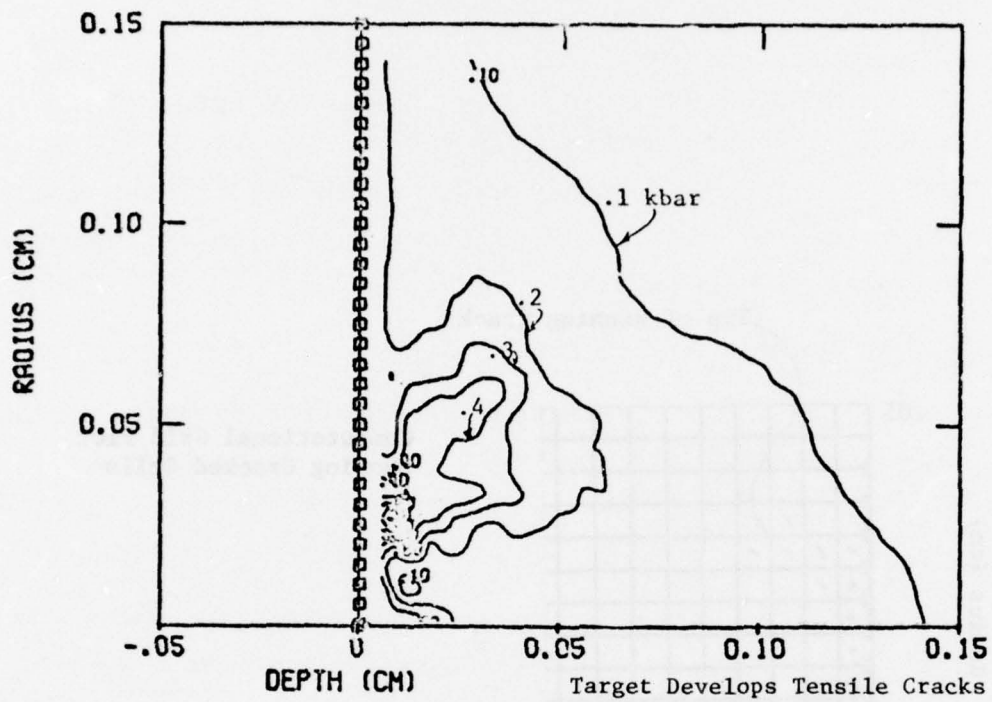


Figure 31. Cumulative Maximum Tensile Stress Contours for 1 mm Water Drop Impact on ZnSe Window at 1100 fps

SECTION V

SENSITIVITY STUDIES ON VARIOUS PARAMETERS INVOLVED IN WATER DROP IMPACTS ON WINDOWS

The 1100 fps water drop impact was used in all the sensitivity studies except for the cases where variation in impact velocity was being examined (Section 5.5).

5.1 Tensile Failure Criteria and Parameters

Two tensile failure criteria were used in the targets with the crack initiation and propagation model described in Section 4. The two models are described below:

o Critical Tensile Stress Criterion

A tensile crack is formed whenever the tensile stress in the material exceeds a pre-specified critical stress value, σ_T . Thus failure occurs in a computational cell if $\sigma > \sigma_T$.

o Stress Integral Failure Criterion

A tensile crack is formed whenever the following integral criterion is satisfied:

$$\int_0^t (\overline{\sigma - \sigma_T}) dt > \kappa_T$$

where

$$(\overline{\sigma - \sigma_T}) = (\sigma - \sigma_T) \text{ if } \sigma \geq \sigma_T \text{ and}$$

$$(\overline{\sigma - \sigma_T}) = 0 \text{ if } \sigma < \sigma_T$$

σ = most tensile principal stress

σ_T = critical stress value; normally the static tensile strength

κ_T = stress integral failure parameter

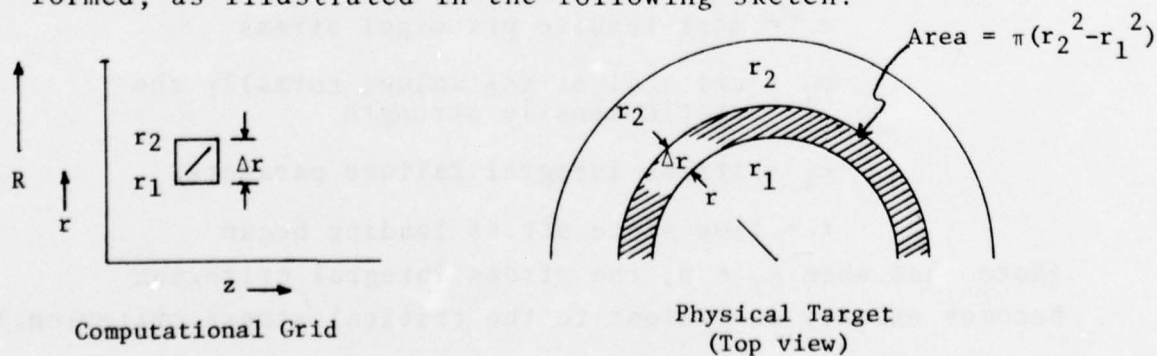
t = time since stress loading began

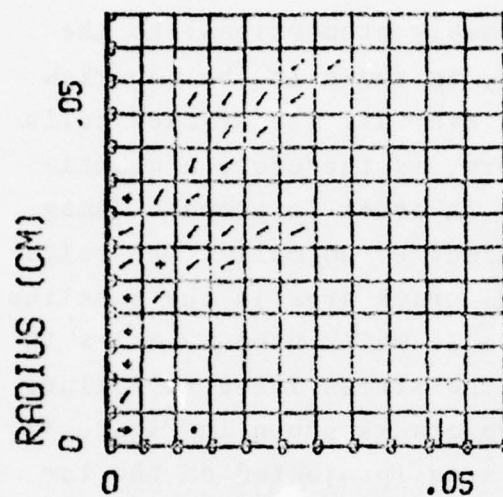
(Note that when $\kappa_T = 0$, the stress integral criterion becomes exactly equivalent to the critical stress criterion.)

Figure 5, page 10, and Figure 27, page 55, show the dynamic target response in terms of crack patterns using the simple critical stress criterion ($\kappa_T = 0$) with $\sigma_T = 6500$ psi for the 1100 fps impact. Directly under and near the impact point, cracks form within the first few cycles of the numerical calculation. These quickly close as the surface impact pressure develops. This is inconsistent with experimental observations and with physical intuition. Tensile stresses may initially occur near the impact point, but their duration is so short that there probably is not sufficient *time* for a crack to form. In order to investigate the importance of tensile stress duration on crack initiation and propagation, the stress integral failure parameter, κ_T , was varied. This model has been examined for metals in Reference 20.

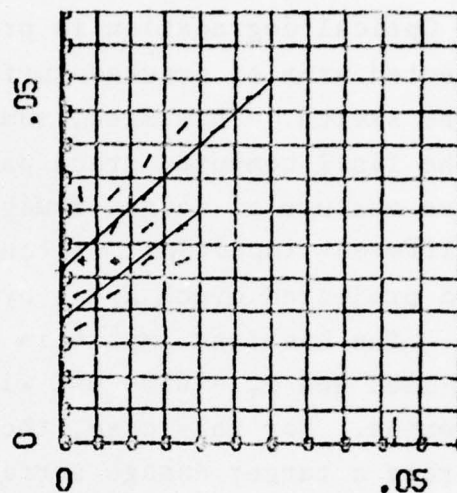
Figure 32 shows the final crack patterns using various values of κ_T for $\sigma_T = 6500$ psi and for the 1100 fps impact. A value of $\kappa_T = 5 \times 10^{-7}$ Mbar- μ sec is sufficient to remove the very short duration cracks near the impact point. A κ_T of 5×10^{-6} Mbar- μ sec significantly reduces the extent of crack propagation. Figure 32 illustrates the *qualitative* effect of κ_T variations on target damage.

The quantitative measure of target damage adopted in this study is based on *cracked surface area* available for optical degradation. When a computational cell fails due to tension in the target, a cylindrically symmetric surface is formed, as illustrated in the following sketch:

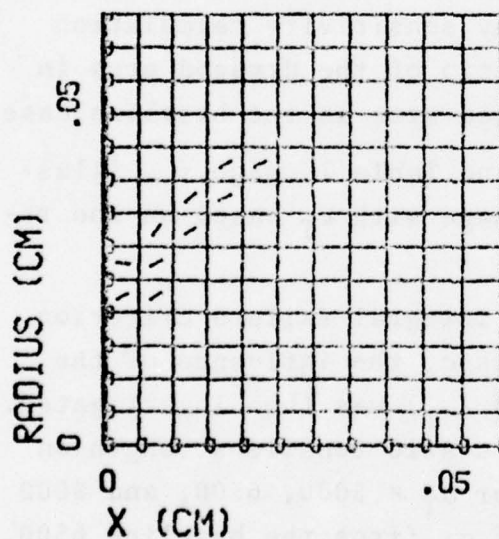




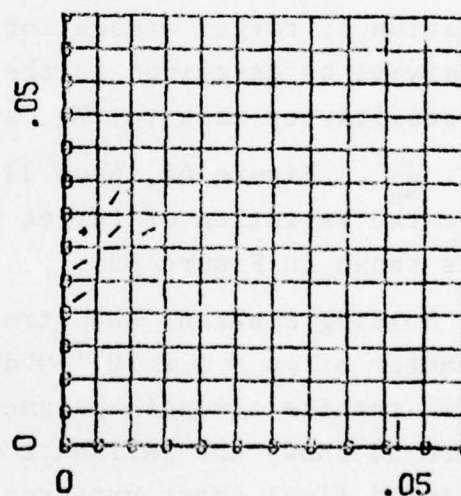
Case 1
 $\kappa_T = 0$



Case 2 (baseline)
 $\kappa_T = 5.0 \times 10^{-6} \text{ Mbar-}\mu\text{sec}$



Case 3
 $\kappa_T = 2.0 \times 10^{-6} \text{ Mbar-}\mu\text{sec}$



Case 4
 $\kappa_T = 5.0 \times 10^{-6} \text{ Mbar-}\mu\text{sec}$

Figure 32. Crack Patterns as a Function of Stress Integral Parameters for 1100 fps Impact of .1 cm Water Drop on ZnSe Window

Optical degradation is presumably proportional to the projected area of cracked surface, as shown in the top view in the sketch. This area, summed over all the cracked cells in the final computed crack pattern, is therefore a quantitative measure of target damage. In order to compare damage in different impacts, it is convenient to normalize the calculated projected crack areas by the crack area in the baseline case. The baseline impact is Case 2, which used $\kappa_T = 5 \times 10^{-7}$ Mbar- μ sec and $\sigma_T = 6500$ psi with the stress integral failure criterion. For this case, the two cracks shown in Figure 32 generate a target damage surface area (projected on the target surface) of $A_n = 8.07 \times 10^{-3} \text{ cm}^2$, which is 3% greater than the projected area of the water drop.

Once this quantitative measure is established, the variation of target damage for any sensitivity calculation can always be described as the ratio of the damaged area in the sensitivity case to the damaged area in the baseline case, i.e., $\frac{A}{A_n}$. Figure 6A, page 11, and Table I, page 6, illustrate the variation of target damage with κ_T based on the results shown in Figure 32.

Holding constant the stress integral failure criterion parameter of $\kappa_T = 5 \times 10^{-7}$ Mbar- μ sec, the influence of the static tensile strength parameter (σ_T) was then investigated. Figure 33 shows the influence of static tensile strength on predicted final crack patterns for $\sigma_T = 5000, 6500$, and 8000 psi. This ± 1500 psi variation of σ_T (from the baseline 6500 psi tensile strength) caused significant changes in the extent of crack propagation. For $\sigma_T = 5000$ psi, the degree of target cracking increased significantly, $A/A_n = 2.26$. The $\sigma_T = 8000$ psi target, on the other hand, showed only a limited

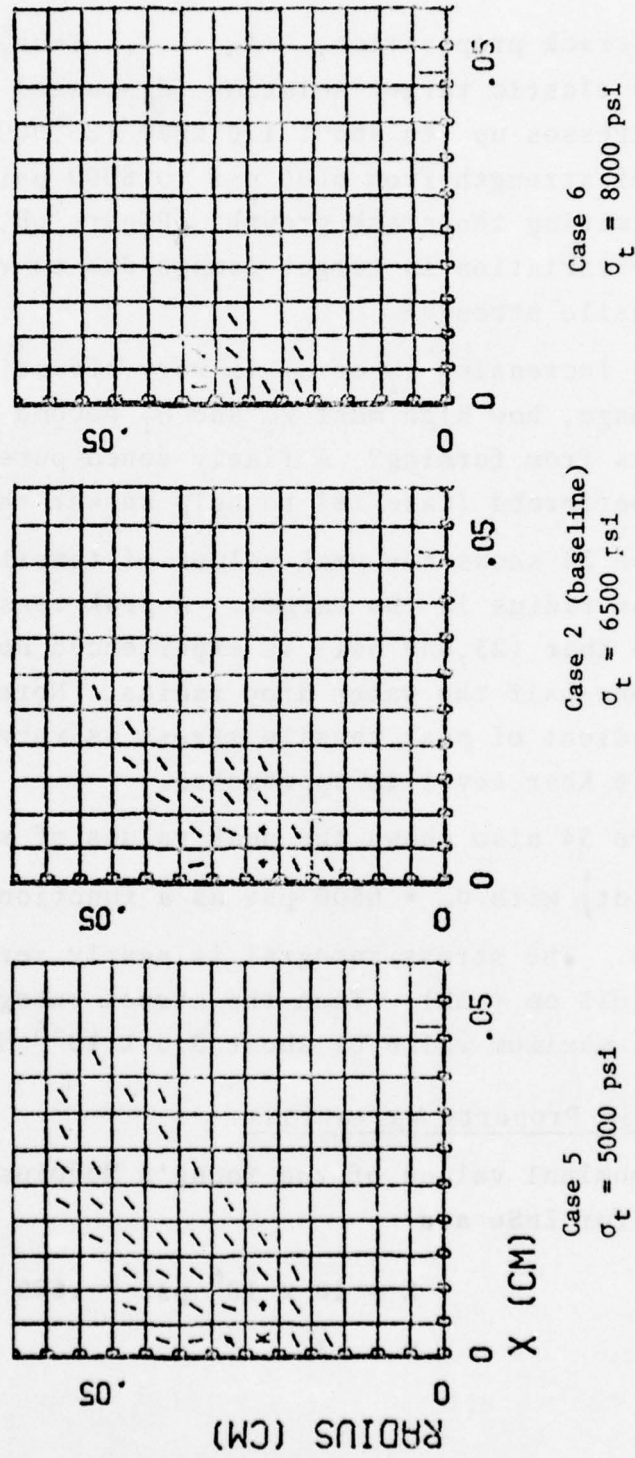


Figure 33. Crack Patterns as a Function of Tensile Strength, σ_T , for 1100 fps Impact of .1 cm Water Drop on ZnSe Window

amount of crack propagation, $A/A_n = .4$. Thus, even though the purely elastic target solution (discussed below) showed tensile stresses up to about 1.6 Kbar (23,000 psi), a modest increase of strength from 6500 psi to 8000 psi is very effective in limiting the crack growth. Figure 6B, page 11, illustrates the variation in target damage due to variations in static tensile strength.

Since increasing κ_T or σ_T is very effective in *reducing* target damage, how high must κ_T and σ_T become to *prevent* tensile cracks from forming? A finely zoned purely elastic solution was performed (Case 18) to help answer this question.

Figure 34 shows the peak values of tensile stress as a function of radius in the target. A peak tensile stress of almost 1.6 Kbar (23,000 psi) is experienced near the surface at about one-half the water drop radius. Note that the radial gradient of peak tensile stress is very sharp as the maximum 1.6 Kbar level is approached.

Figure 34 also shows the peak values of stress integral $\left(\int_0^t (\sigma - \sigma_T) dt \right)$ with $\sigma_T = 6500$ psi as a function of radius in the target. The stress integral is nearly zero for radii up to about .015 cm (.3R). Then the stress integral rapidly peaks to a maximum value of about 3.5×10^{-5} Mbar- μ sec.

5.2 Elastic Property Variations

The nominal values of the Young's Modulus (E) and Poisson's Ratio (ν) for ZnSe are

$$E = 10 \times 10^6 \text{ psi} = .689 \text{ Mbar}$$

$$\nu = .3$$

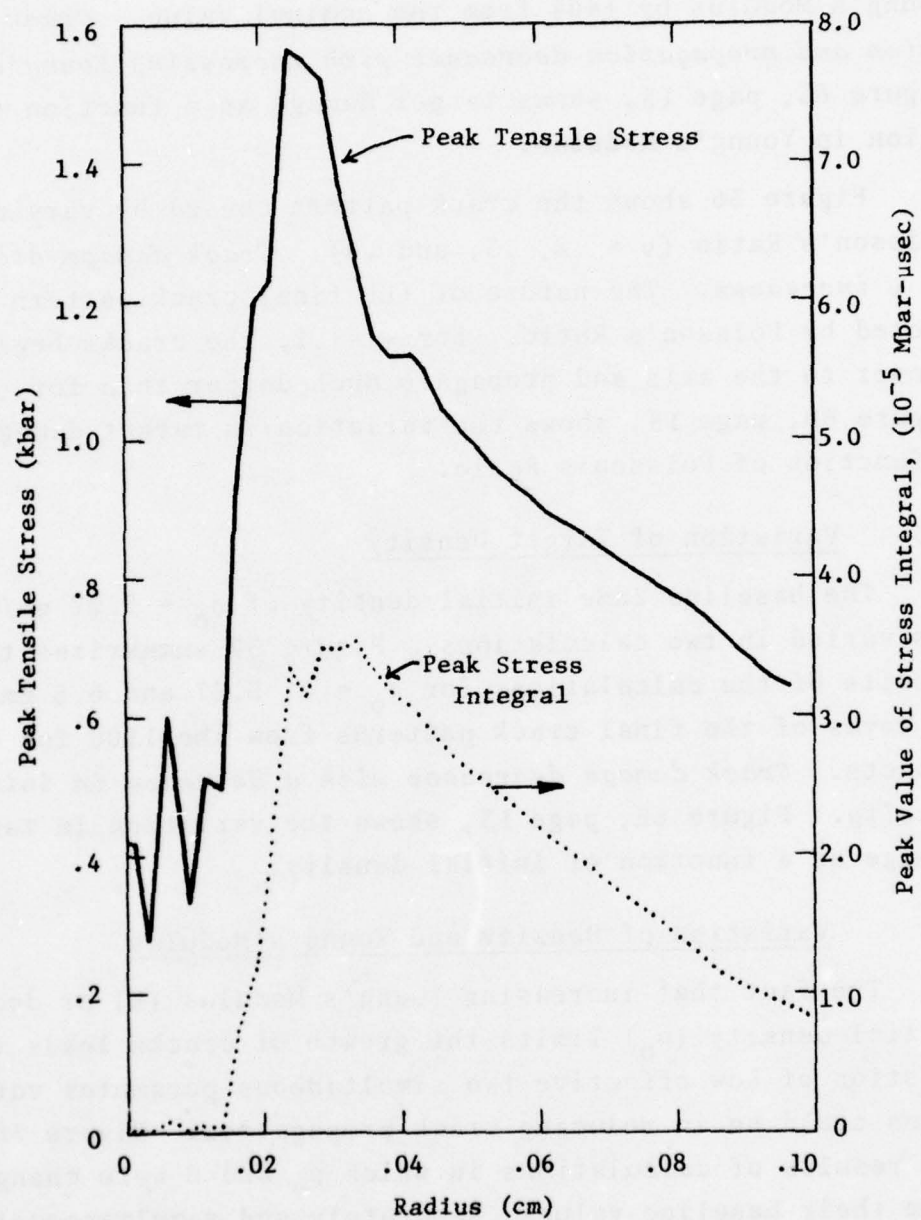


Figure 34. Peak Values of Tensile Stress and Stress Integral of Purely Elastic ZnSe during 1100 fps Impact of .1 cm Water Drop (Case 18)

Figure 35 shows the crack patterns caused by varying Young's Modulus by $\pm 40\%$ from the nominal value. *Crack formation and propagation decreases with increasing Young's Modulus.* Figure 6C, page 13, shows target damage as a function of variation in Young's Modulus.

Figure 36 shows the crack pattern caused by varying Poisson's Ratio ($\nu = .2, .3, \text{ and } .4$). *Crack damage decreases as ν increases.* The nature of the final crack pattern is affected by Poisson's Ratio. For $\nu = .2$, the cracks begin closer to the axis and propagate much deeper than for $\nu = .4$. Figure 6D, page 13, shows the variation in target damage as a function of Poisson's Ratio.

5.3 Variation of Target Density

The baseline ZnSe initial density of $\rho_0 = 5.27 \text{ gm/cm}^3$ was varied in two calculations. Figure 37 summarizes the results of the calculations for $\rho_0 = 4, 5.27 \text{ and } 6.5 \text{ gm/cm}^3$ in terms of the final crack patterns from the 1100 fps water impacts. *Crack damage decreases with a decrease in initial density.* Figure 6E, page 13, shows the variation in target damage as a function of initial density.

5.4 Variation of Density and Young's Modulus

The fact that increasing Young's Modulus (E) or decreasing initial density (ρ_0) limits the growth of cracks leads to the question of how effective two simultaneous parameter variations could be in reducing crack propagation. Figure 38 shows the results of calculations in which ρ_0 and E were changed from their baseline values, separately and simultaneously. *The reduction in target crack damage when both E and ρ_0 are changed ($A/A_n = .33$) is much greater than when either E ($A/A_n = .64$) or ρ_0 ($A/A_n = .77$) is independently changed.*

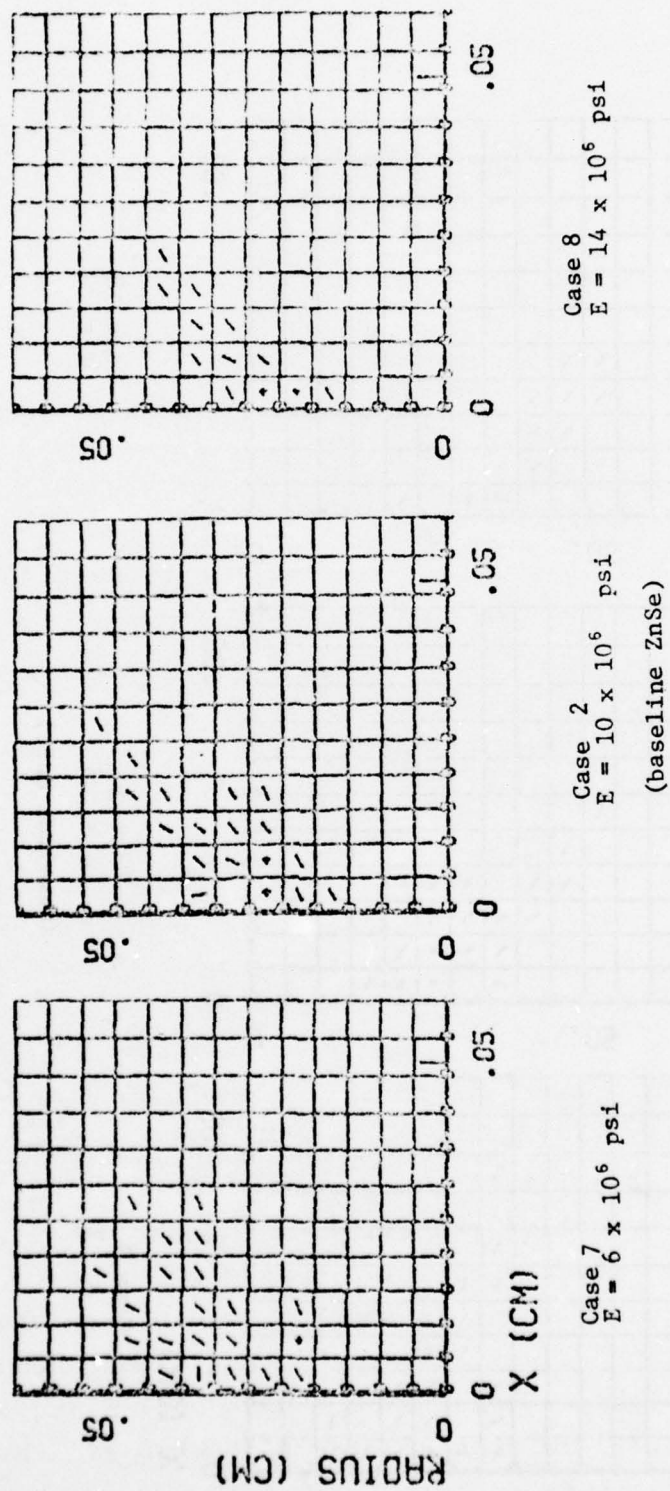


Figure 35. Crack Patterns as a Function of Young's Modulus, E , for 1100 fps Impact of .1 cm Water Drop on ZnSe Window

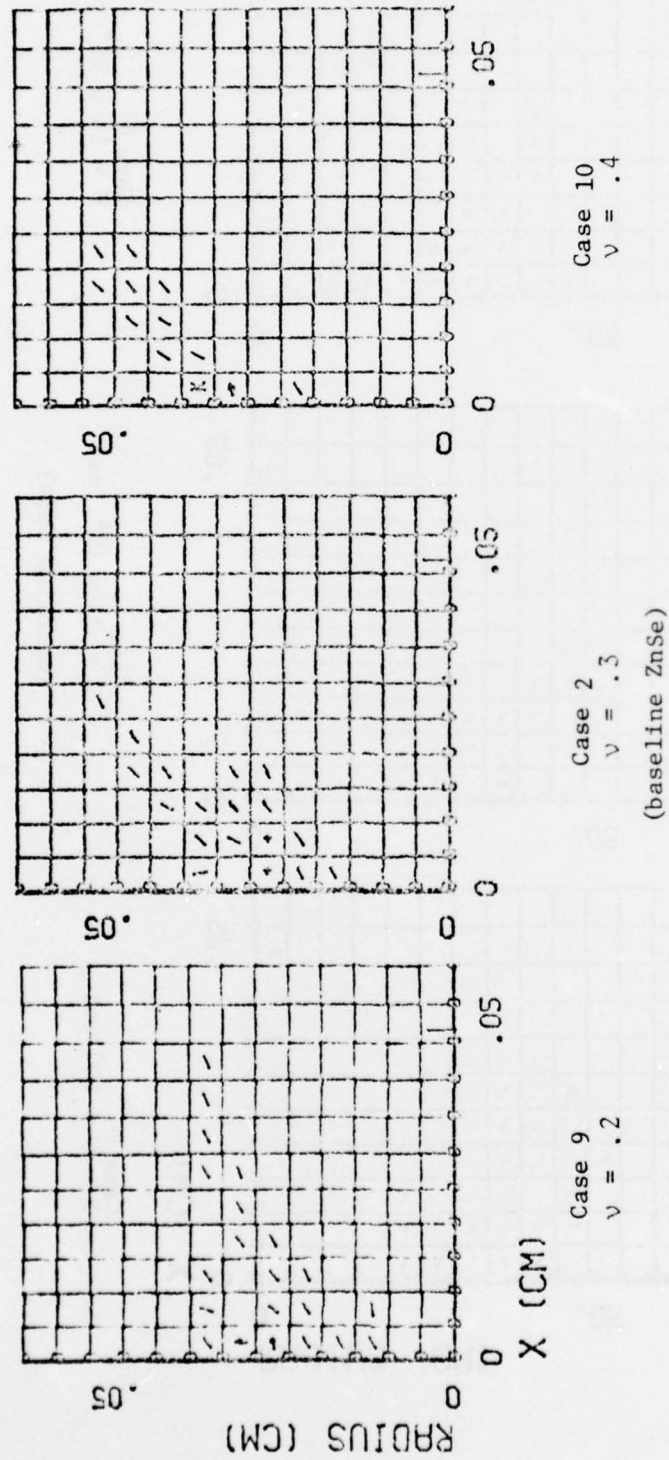


Figure 36. Crack Patterns as a Function of Poisson's Ratio, ν , for 1100 fps Impact of .1 cm Water Drop on ZnSe Window

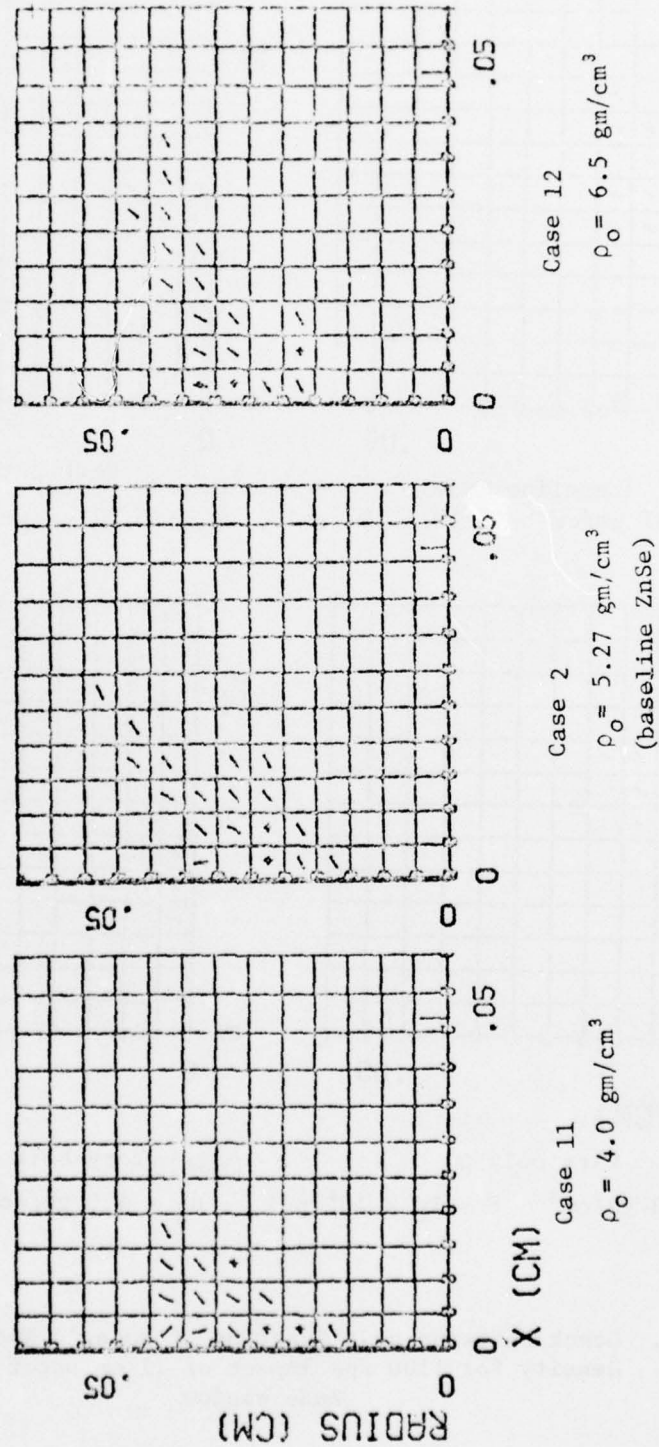
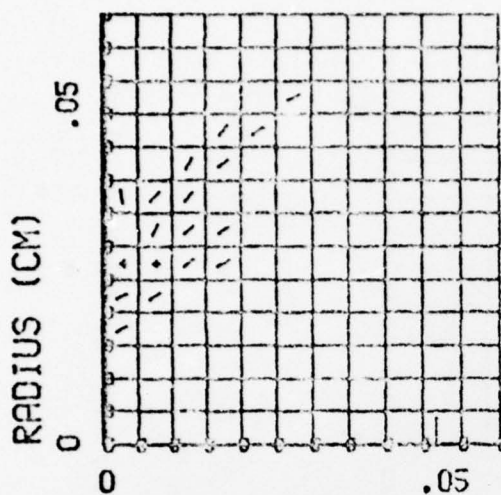
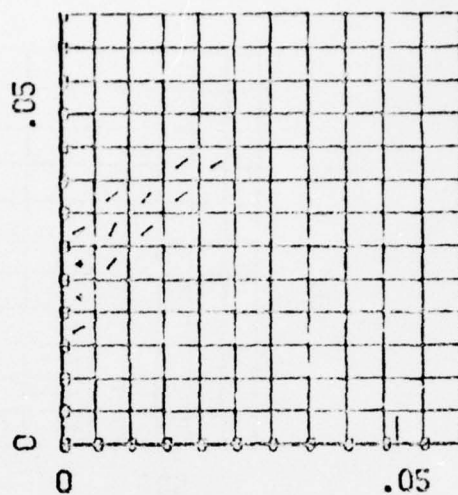


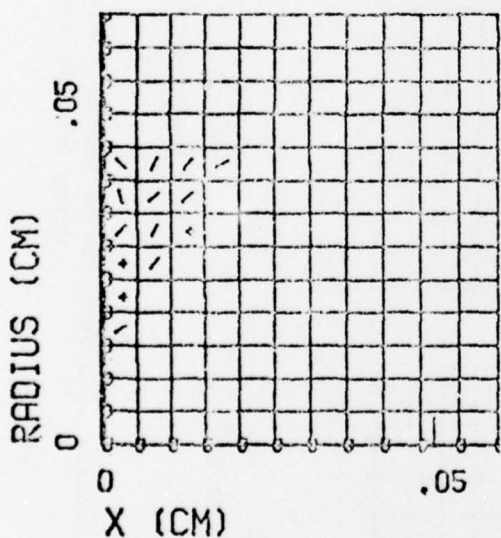
Figure 37. Crack Patterns as a Function of Nominal Density, ρ_0 , for 1100 fps Impact of .1 cm Water Drop on ZnSe Window



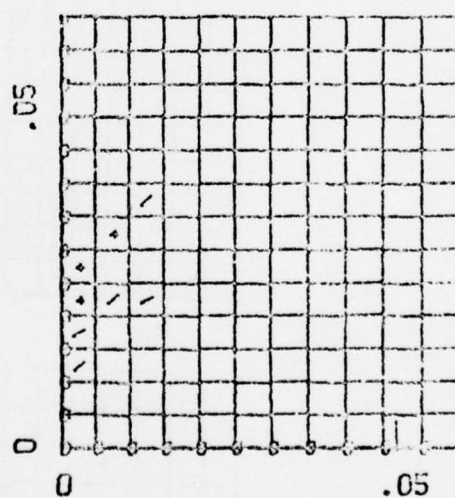
Case 2 (baseline ZnSe)
 $\rho_o = 5.27 \text{ gm/cm}^3$ $E = 10 \times 10^6 \text{ psi}$



Case 8 Vary only E
 $\rho_o = 5.27 \text{ gm/cm}^3$ $E = 14 \times 10^6 \text{ psi}$



Case 11 Vary only ρ_o
 $\rho_o = 4.0 \text{ gm/cm}^3$ $E = 10 \times 10^6 \text{ psi}$



Case 13 Vary both ρ_o and E
 $\rho_o = 4.0 \text{ gm/cm}^3$ $E = 14 \times 10^6 \text{ psi}$

Figure 38. Crack Patterns as a Function of Young's Modulus and Density for 1100 fps Impact of .1 cm Water Drop on ZnSe Window

5.5 675 fps Impact Velocity Case and Repeated Impact on the Same Site

The baseline velocity in the sensitivity study was 1100 fps. The 675 fps impact loading pressure function was used to examine the influence of impact velocity on target damage. Using the baseline target parameters, i.e., $\kappa_T = 5 \times 10^{-7}$ Mbar- μ sec, $\sigma_T = 6500$ psi, and $\Delta x = .005$ cm, the ZnSe target did *not* crack in a 675 fps impact (Case 19). Figure 39 shows the peak tensile stress in the target as a function of radius for this case. The maximum tensile stress in the solution is 3% above the static tensile strength (σ_T) of the material, but the duration of this overstress is far too short to cause failure when $\kappa_T = 5 \times 10^{-7}$ Mbar- μ sec.

The numerical solution was repeated using the simple critical tensile stress fracture criteria ($\kappa_T = 0$) with $\sigma_T = 6500$ psi, (Case 20). In this case, only one cell cracked. Thus, the numerical solution simulated a crack initiation with no crack propagation. This situation is somewhat analogous to a single water drop impact which causes only marginal damage. Target damage will develop after multiple impacts.

Generally, multiple impacts will not occur on exactly the same site. However, in an axisymmetric code, multiple impact loadings can only be simulated for impacts on the same site. The multiple impact case on the same site is nevertheless of interest because of the interactions between stress waves and pre-existing cracks. To investigate the nature of crack growth from stress interactions during multiple impacts on the same site, a second water drop impact and then a third were simulated on the target. The second and third drop were simulated using the 675 fps loading function applied to the final damaged target configuration from the previous impact.

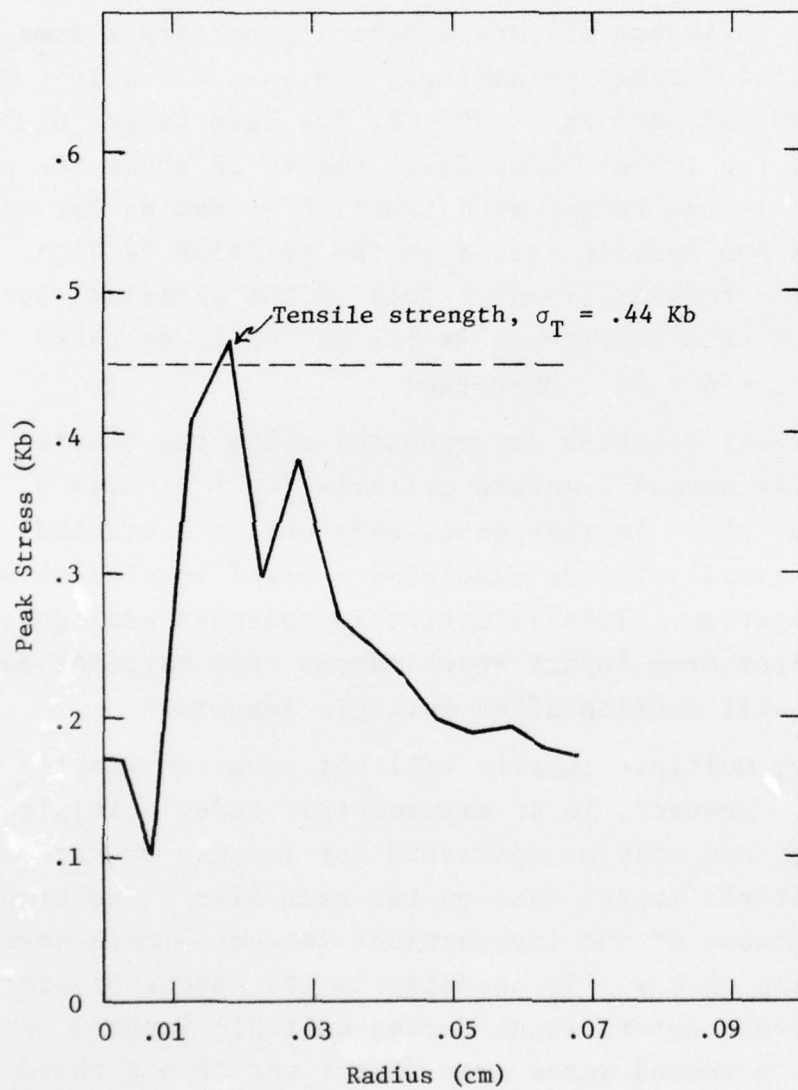


Figure 39. Peak Tensile Stress as a Function of Radius for 675 fps Impact Case

Figure 40 shows the crack pattern after each water drop impact. The effect of the multiple impacts is to spread tensile failure. Also, the crack pattern from the 675 fps multiple impact loading appears shallower than in the 1100 fps single impact cases.

5.6 Target Thickness

The baseline target thickness in this study was $1/8" = .3175$ cm. At this thickness, the dilatational wave takes about $1.5 \mu\text{sec}$ to reflect off the target rear surface and interact with the tensile cracks which develop near the impact site. Since the 1100 fps baseline calculation was numerically integrated to over $4 \mu\text{sec}$, while the crack pattern did not change after $.5 \mu\text{sec}$, the $1/8"$ target acted as if it were semi-infinite.

A much thinner target was simulated (Case 21) to investigate the potential interaction between target free surfaces and crack propagation. In Case 21, a 1 mm thick target with baseline ZnSe characteristics was impacted at 1100 fps with the 1 mm water drop. Figure 41 shows the final crack pattern for this thin target case. Crack segments which formed in the .1 cm target but not in the .3175 cm target are shown circled.

The thin target permitted sufficient interactions with the rear surface to somewhat enhance crack propagation. Also, the rear of the target experienced failure from hoop and radial tensile stresses. Normally, we would expect a spall-type failure in thin plates, i.e., from axial tensions. In this case, the fact that the loading function has a peak compressive load which occurs off axis causes relatively large radial motions and stresses which are larger than the axial motions and stresses at the target rear surface.

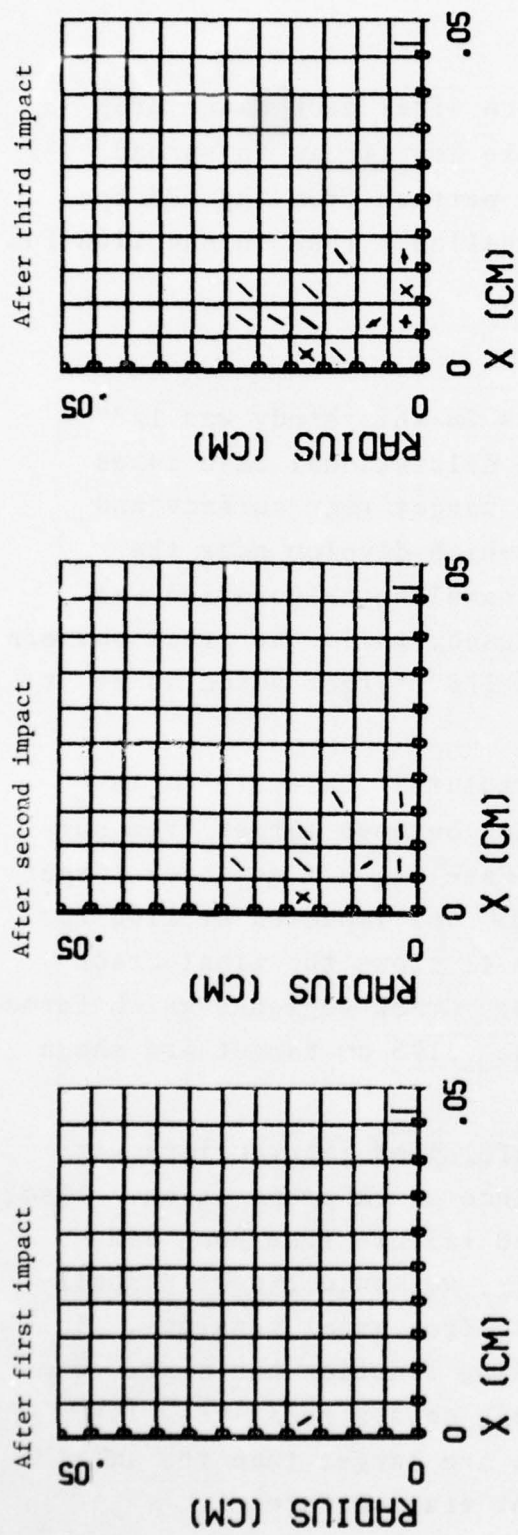


Figure 40. Crack Pattern after Impact of Three Water Drops at 675 fps on ZnSe

07 FEB 76

CALIFORNIA RESEARCH AND TECHNOLOGY WAVE-L CODE

SUBSONIC EROSION CASE TH1

CYCLE 181

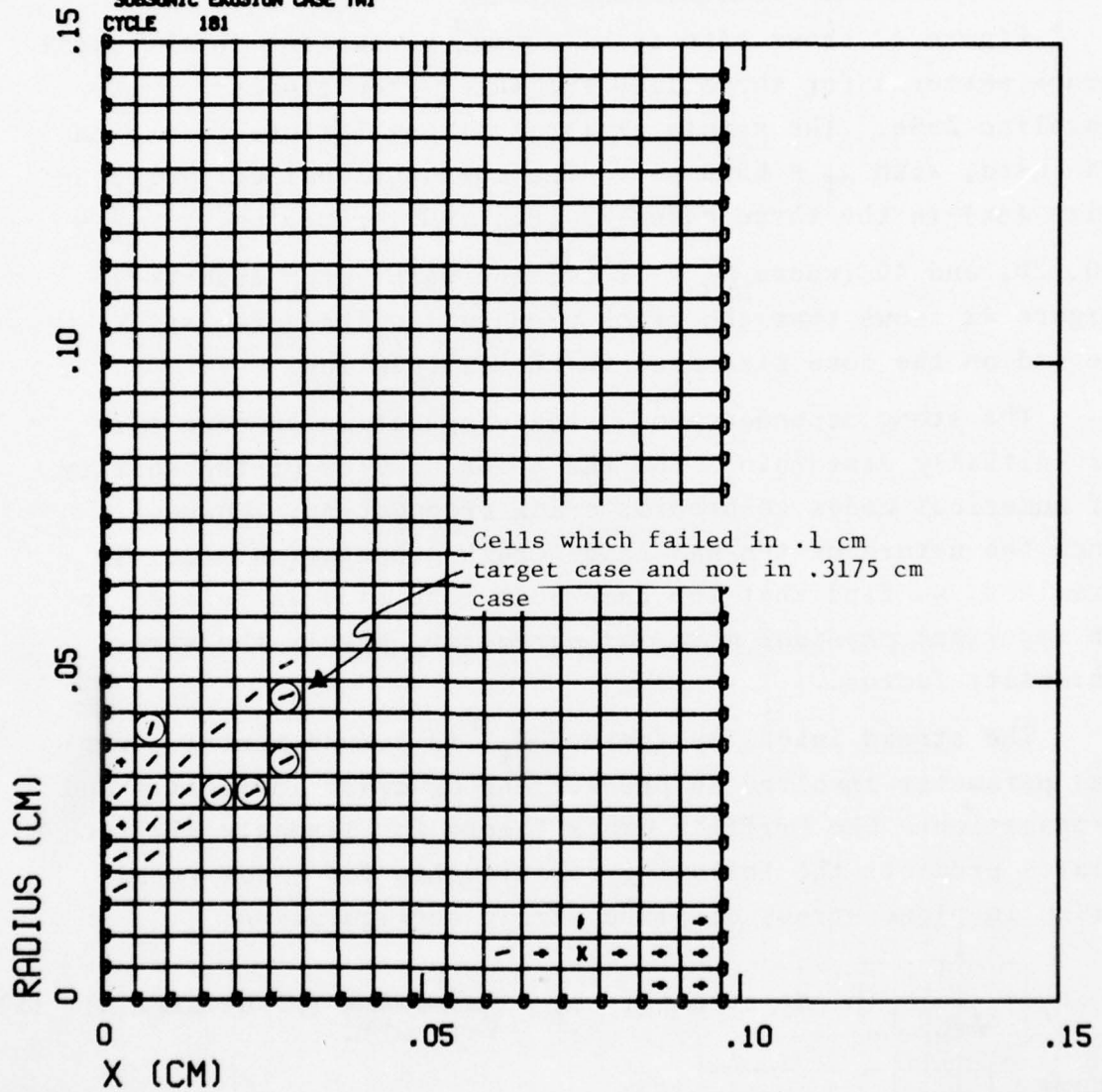


Figure 41. Crack Pattern for Thin Target (.1 cm) Impacted with Water Drop at 1100 fps

5.7 Variations in Computational Zone Size and Effective Variation in Target Toughness

Figure 42 shows effects of zoning variations in the final crack patterns for three 1100 fps water drop impacts on the baseline ZnSe. The simple critical stress failure criterion was used, with $\sigma_T = 6500$ psi. The computational cell or zone size (Δx) in the three cases is .01, .005, .0025 cm or $\frac{D_0}{\Delta x} = 10, 20, \text{ and } 40$ (where $D_0 = .1$ cm, the water drop diameter). Figure 42 shows that the crack propagation characteristics depend on the zone size used in the calculation.

The strong dependence of crack propagation on zone size is initially disturbing from the point of view of the ability of numerical codes to predict crack propagation. However, once the nature of the *numerical* crack propagation model is examined, we find that the numerical zone size is related to an important *physical material parameter*, namely the stress intensity factor.

The stress intensity factor, K_I , is a fundamental material parameter involved in predictions of crack initiation and propagation. The Griffith Crack Theory for linearly elastic plates predicts the following relationship for *crack initiation* in plane stress or plane strain configuration:

$$\sigma_T = \frac{K_I}{\sqrt{\pi C}} \text{ (plane stress), } \sigma_T = \frac{K_I}{\sqrt{\pi(1-\nu^2)C}} \text{ (plane strain) } \quad (5)$$

where

K_I = stress intensity factor or crack toughness

$2C$ = length of pre-existing crack nucleus

σ_T = critical far-field tensile stress which
will lead to unstable crack growth

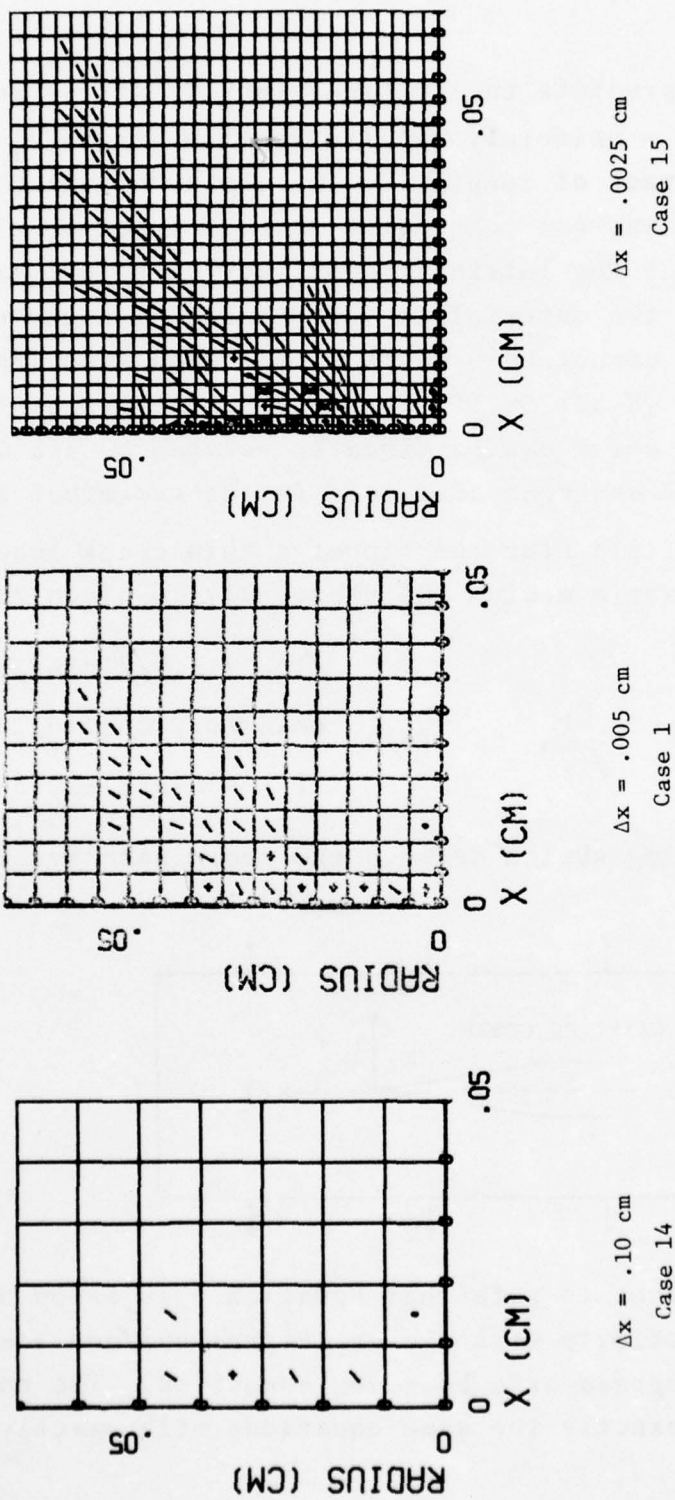


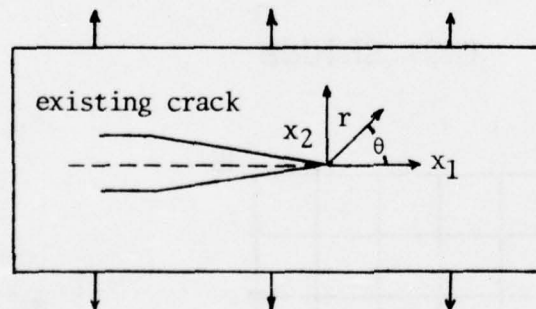
Figure 42. Crack Pattern for 1100 fps Water Drop Impact on ZnSe Window, Zone Size, $D/\Delta x = 10, 20, 40$

Equation 5 predicts the critical tensile stress for unstable crack growth for a uniformly applied tensile stress σ_T with a pre-existing crack of length $2C$. In the numerical solution, *crack initiation* was not considered to be a function of $2C$. Furthermore, since the intrinsic distribution of pre-existing crack lengths in the material is independent of numerical zone size, Equation 5 cannot be used to relate zone size (Δx) and stress intensity factor (K_I). *On the other hand, the stress field near an existing crack can be directly related to the crack propagation model and zone size used in the numerical solutions.*

The stress field near the tip of a thin crack loaded in tension in an elastic medium (Reference 21) is given by

$$\begin{Bmatrix} \sigma_{11} \\ \sigma_{12} \\ \sigma_{22} \end{Bmatrix} = \frac{K_I}{\sqrt{2\pi r}} \cos(\theta/2) \begin{Bmatrix} 1 - \sin(\theta/2)\sin(3\theta/2) \\ \sin(\theta/2)\cos(3\theta/2) \\ 1 + \sin(\theta/2)\sin(3\theta/2) \end{Bmatrix} \quad (6)$$

where the following sketch defines the coordinate system



It is important to note that Equation 6 is based on the equations of elasticity *with the crack-free surface condition* (no tractions) *imposed as a boundary condition*. The numerical solutions solve exactly the same equations with exactly the

same free surface boundary conditions on the crack surfaces. Thus, the numerical solutions will approximate Equation 6. The elastic tensile stress causing crack propagation along the direction of the existing crack ($\theta = 0$) is therefore governed (near the crack tip) by

$$\sigma_{22} = \frac{K_I}{(2\pi r)^{1/2}} \quad (7)$$

In the numerical solutions, crack propagation is governed by the magnitude and duration of tensile stresses in the computational cells in front of existing cracks. (In Section 4, the increase in tensile stresses in front of existing cracks in the numerical solutions was demonstrated). If, as a first approximation, we assume that the typical distance between the existing crack and the nearest cell center is $r = \Delta x/2$, and if we assume $\sigma_{22} = \sigma_T$ for crack propagation in the numerical solutions, then Equation 7 immediately relates the fundamental stress intensity factor to the parameters σ_T and Δx , i.e.,

$$\sigma_T = \frac{K_I}{(\pi \Delta x)^{1/2}}$$

$$\text{or} \quad K_I = (\pi \Delta x)^{1/2} \sigma_T \quad (8)$$

Note that Equation 8 completely specified the effective stress intensity parameter once σ_T and Δx are specified. Thus, each zoning and σ_T variational calculation (with $\kappa_T = 0$) can be viewed as a variation in the single material parameter K_I . Table 5 indicates the effective stress intensity factors for the three cases shown in Figure 42.

TABLE 5
EFFECTIVE STRESS INTENSITY FACTORS ACCORDING TO
EQUATION 8

Case*	$\frac{D}{\Delta x}$	Δx (cm)	K_I^{**} psi (cm) ^{1/2}
14	10	.01	1099
1	20	.005	777
15	40	.0025	550

* All cases use $\kappa_T=0$, $\sigma_T = 6500$ psi, $\nu = .3$

** K_I for ZnSe from Table IV is 600-1300 psi-inch^{1/2}
which is 960-2070 psi-cm^{1/2}

Note that the effective K_I used in the numerical calculations is reasonably close to the experimental values for ZnSe.

An important verification of the numerical simulation of K_I based on Eq. 8 was performed. If the numerical solutions do approximately simulate a K_I based on the choice of σ_T and Δx , then similar crack patterns should develop for similar values of K_I . Figure 7, page 15, compares Cases 15 and 16 which have the widest variation in σ_T and Δx of all the cases performed in this study. Table 6, below, summarizes the relevant parameters.

TABLE 6
EFFECTIVE STRESS INTENSITY FACTORS ACCORDING TO
EQUATION 8

Case	σ_T (psi)	$\frac{D}{\Delta x}$	Δx (cm)	K_I (psi-(cm) ^{1/2})
15	6500	40	.0025	550
16	3000	10	.01	507

Note that σ_T changes by a little over a factor of 2 and Δx varies by a factor of 4 between the two cases; therefore, K_I is relatively constant ($\sim 8\%$ change).

As Figure 7, page 15, demonstrates, the crack patterns for the two cases are very similar. Both targets have long cracks extending beyond .05 cm in radius (one drop) and below a depth of .05 cm. The target damage in the two cases is also very close ($A/A_n = 3.57$ in Case 15, compared to 3.36 in Case 16). The only important difference in the two patterns is that Case 16 ($D/\Delta x = 10$) has developed a crack near the axis of symmetry. The numerics near the axis of symmetry in a relatively coarsely zoned problem could easily cause very short tensile oscillations in excess of the low σ_T value of 3000 psi in Case 16. In Case 15, on the other hand, the tensile oscillations would have to exceed 6500 psi in a very finely resolved numerical solution. For this reason, we would discount the cracks near the axis in Case 15.

There is still much to be understood about the relationship between the material physical parameters and numerical solution parameters such as σ_T , κ_T , and zone size. *However, the results to date indicate that the numerical crack propagation model used in this study can be systematically related to the fundamental stress intensity factor K_I .* Additional efforts should be directed toward improving the crack initiation models in a form which is independent of computational cell size.

REFERENCE

1. G. F. Schmitt, Jr., "Rain Droplet Erosion Mechanisms in Transparent Plastic Materials", Proc. 45th International Conf. on Rain Erosion and Associated Phenomena, Meersburg, Germany, May 1974.
2. M. L. Wilkins, "Calculation of Elastic-Plastic Flow", UCRL-7322, Rev. 1, January 1969.
3. A. A. Fyall, "Single Impact Studies with Liquids and Solids", Proceedings of the Second Meersburg Conference on Rain Erosion and Allied Phenomena, August 1967.
4. Y. C. Huang, "Numerical Studies of Unsteady Two-Dimensional, Liquid Impact Phenomena", PH.d. Dissertation, University of Michigan (1971).
5. W. A. Walker and H. M. Sternberg, "The Chapman-Jouguet Isentrope and the Underwater Shockwave Performance of Pentolite", The Fourth Symposium on Detonation, Naval Ordnance Laboratory, White Oak, Md., 12-15 October 1965, pp. 27-38.
6. O. B. Engel, "Damage Produced by High-Speed Liquid-Drop Impact", J. Appl. Phys. Vol. 44, pp. 692-704, February, 1973.
7. Y. C. Huang, "Three-Stage Impact Process in Liquid Impingement", Combustion Engineering, Inc., 1974.
8. M. C. Rochester and J. G. Brunton, "Surface Pressure Distribution During Drop Impingement", paper presented at the Fourth International Conference on Rain, Erosion and Associated Phenomena, Meersburg, West Germany, May 1974.
9. F. P. Bowden and T. F. Field, "The Brittle Fracture of Solids by Liquid Impact, by Solid Impact, and by Shock", Proc. Royal Soc. (London) A282, 331 (1964).
10. G. E. Eggum and M. Rosenblatt, "1100 fps Impact of a 1 mm Water Drop on a Rigid Surface at Early Times", September 1975, CRT 5010-1, Prepared for Prototype Development Associates and ONR.

REFERENCES (Cont'd)

11. V. I. Kuskov, A. P. Rusakoo, and A. N. Mentser, "Elastic Constants of ZnSe", Soviet Physics-Solid State, pp. 1869-1870, January 1973.
12. B. H. Lee, "Elastic Constants of ZnSe and ZnSe between 77°-300°K", J. Appl. Phys. Vol. 41, pp. 2984-2987, June 1970.
13. B. H. Lee, "Pressure Dependence of Second Order Elastic Constants of ZnTe and ZnSe", J. Appl. Phys. Vol. 41, pp. 2988-2990, June 1970.
14. D. Berlincourt, H. Jaffee, and L. R. Shiozawa, "Electro-elastic Properties of the Sulfides, Selinides and Tellurides of Zinc and Cadmium", Phys. Rev., Vol 129, pp. 1009-1017, February 1972.
15. A. G. Evans and H. Johnson, "A Fracture Mechanics Study of Zinc Selenide for Laser Window Applications", Institute for Materials Research, National Bureau of Standards, Washington, D. C.
16. Private communication with Dr. John C. Wurst.
17. R. W. Rice, "High Energy Laser Windows", Naval Research Laboratory, June 1974.
18. Kodak Publication U-72.
19. W. F. Adler, "Characterization of Transparent Materials for Erosion Resistance", Textron's Bell Aerospace Co., February, 1975.
20. F. R. Taler and B. M. Butcher, "A Criterion for Time Dependence of Dynamic Fracture", Sandia Laboratories, 1968.
21. J. R. Rice "Mathematical Analysis in the Mechanics of Fracture", Chapter 3, Vol. II of Fracture Edited by H. Liebowitz, Academic Press, 1968.